UNIVERSITY OF CALIFORNIA, MERCED

Development of a Bioprinter Towards Controlling the Vascular Microenvironment

A dissertation submitted in partial satisfaction of the requirements
for the degree Doctor of Philosophy

in

Bioengineering and Small-Scale Technologies

by

Edwin M. Shen

Degree year: 6

Committee in charge:

Professor Kara McCloskey, Primary Advisor

Professor Anand Subramaniam

Professor Song Li

Professor Changqing Li, Chair

The Dissertation of Edwin M. Shen is approved, and it is acceptable in quality and form for publication on microfilm and electronically

_____

Professor Changqing Li, Committee Chair

_____

Professor Anand Subramaniam

_____

Professor Song Li

_____

Professor Kara McCloskey, Primary Advisor

University of California, Merced
2018

Acknowledgements

The research in this document was funded by the California Institute for Regenerative Medicine (CIRM) Basic Biology Award (no. RB5-07414), NSF Integrative Graduate Education and Research Traineeship (IGERT) Award no. 0965918, and NSF-Science and Technology Center (STC) for the Emergent Behavior of Integrated Biological Systems (EBICS) Award no. 0939511, and NSF Innovation Corps (I-Corps) Award no. 1816189.

Chapter 3 was completed with the assistance from my undergraduate assistants Lisa V. Salmeron, and Gabriella Sanchez who helped with cell culture and flow cytometry.

Chapter 5 was completed in collaboration with graduate student Maria Mendoza who performed all the cell culture, imaging and data analysis of live cells, as well as the the printing and material preparation alongside me.

Customer discovery for ModiPrint was performed in collaboration with Rachel Hatano and Dr. Elliot Botvinick with the guidance of NSF's I-Corps. Commercialization was performed with the help of UC Merced's Venture Lab and UC Berkeley's New Business Community Law Clinic.

Finally, I would like to thank my advisor, Dr. Kara McCloskey, for guiding me through all aspects of these studies.

Curriculum Vitae

Research scientist trained in tissue engineering with a diverse set of biology, engineering, and programming expertise. Enjoys designing and integrating devices into the biology workflow. Skilled scientific writer with experience in documenting protocols. Independent and creative thinker.

Education

Ph.D., Biological Engineering and Small-Scale Technology — 2014 – Present
University of California, Merced — (Anticipated Summer 2020)
Advisor: Kara E. McCloskey

B.S., Bioengineering — 2011 – 2014
University of California, Merced
Graduated in 3 years with honors

Experience

Graduate Student Researcher: University of California, Merced — 2014 – 2020
Vascular tissue engineering and bioprinting.

- Differentiated human pluripotent stem cells into vascular cell lineages.
- Validated the specificity of antibodies with multicolor flow cytometry.
- Designed and trained non-engineers on a bioprinter.
- Guided microvasculature formation of bioprinted cells.
- Managed and trained multiple undergraduate students in cell culture and flow cytometry.

Creator of ModiPrint (www.modiprint.com) — 2020 – Present
Sole designer of a custom, multi-material bioprinter and lab automation device.

- Created an affordable device for high resolution, multi-material bioprinting.
- Programmed the control software (C#) and embedded firmware (C).
- Wrote the documentation for others to recreate and operate this device.
- Created an automatable fluid manipulation technique that embeds small molecule concentration gradients into printed hydrogels.
- Implemented novel stepper control software that improves resolution of extrusion bioprinting.

NSF Innovation Corps: Customer Discovery Grant — 2018 – 2018
Modularized Bioprinter for High Throughput Pharmaceutical Development
Award # 1816189 PI: Kara E. McCloskey

- Acquired $50,000 in funding to research market potential.
- Conducted over 100 customer discovery interviews.
- Lead technology transfer for a UC Irvine senior engineering team to recreate and customize our product.

Skills

Cell Biology & Analysis

Human Cell Culture	Stem Cell Differentiation
Multi-Color Flow Cytometry	Cell Sorting
Murine Dissection and Cell Isolation	Fluorescent Microscopy

Engineering

Photolithography	Microfluidic Devices

Extrusion Bioprinting
G-code for CNC Devices
CAD (Sketchup, Autocad)
Drop-on-demand Bioprinting
Prototyping

Programming
C# (.NET, WPF)
VBA (Excel)
C (Embedded Applications)

First Author Publications

Edwin Shen, Kara E. McCloskey, *Affordable, High-Resolution Bioprinting with Embedded Concentration Gradients.* Bioprinting.
In Review

Edwin Shen, Kara E. McCloskey, *Inadequate Antibodies for Vascular Smooth Muscle Cell Characterization.* PLOS One.
In Review

Edwin Shen, Kara E. McCloskey, *Development of Mural Cells: From In Vivo Understanding to In Vitro Recapitulation.* Stem Cells and Development. July 2017, 26(14): 1020-1041.
Journal Cover

Edwin Shen, *Durotaxis Directed Cell Migration for Enhanced Vascular Stent Endothelialization*. **UC Merced Undergraduate Research Journal**, 2014. 7(1)

Presentations

Podium – 2018 EBICS Tech Conceptualization (1st Place)
ModiPrint: Multimaterial Bioprinter
Podium – 2017 BMES Annual Conference
Podium: *Open Source, Multi‐Printhead, Modular Bioprinting System*
Podium – 2017 UC Symposium
Print It Your Way: Open Source, Multi‐Printhead, Modular Bioprinting System
Poster – 2017 EBICS Retreat
Open Source, Multi-Printhead Modular Bioprinting System
Poster – 2015 BioNanotechnology Summer Institute
Generation of vascular smooth muscle cells from embryonic stem cells
Poster – 2015 Annual EBICS Retreat
Generation of vascular smooth muscle cells from embryonic stem cells under chemically-defined conditions
Poster – 2014 Capstone Design, University of California
Design of Optimal Porous Material for Tissue Engineering

Mentorship

Lisa Vanessa Salmeron 2015 - 2017
Undergraduate Research Assistant
Currently PhD Student at University of California, Riverside

- Training in pluripotent stem cell culture, vascular smooth muscle induction, cell staining
- Guidance for independent project to prepare 3D printable crosslinking alginate in degradable scaffolds
- Assistance in preparing presentations, scientific writing, and academic applications

Gabriella Sanchez 2017 - 2019
CCBM Undergraduate Scholar & Undergraduate Research Assistant

- Training in pluripotent stem cell culture, vascular smooth muscle induction, cell staining, and flow cytometry
- Guidance for preparation of 3D printable crosslinking alginate in degradable scaffolds
- Assistance in preparing presentations

Cheukho Lui 2018 - 2019

Undergraduate Research Assistant

- Training in bioprinter hardware and software development
- Assistance in preparing academic applications

Printer Pals 2017

University of California, Irvine Senior Design Team (5 Members)

- Interviewed and selected team leader to match project
- Assistance in preparing proposals to secure funding
- Provide technical advice throughout project

Teaching Experience

Teaching Assistant - University of California, Merced

- Introduction to Biology Discussion — Spring 2018, Spring 2019 – 2020
- Introduction to Materials — Fall 2017
- Introduction to Biology Lab — Fall 2017, Spring 2018
- Biotransport — Spring 2017
- Introduction to Materials — Fall 2016
- Capstone Design — Spring 2015
- Biotransport — Fall 2014
- Analogs and Digital Devices — Fall 2014

Guest Lectures

- *Applications, Properties, and Fabrication of Biomaterials* — March 2015
  Tissue Engineering - University of California, Merced

Abstract

Development of a Bioprinter Towards Controlling the Vascular Microenvironment

For the degree Doctor of Philosophy in Bioengineering and Small-Scale Technologies

By Edwin M. Shen

University of California, Merced

Committee in charge:
Professor Changqing Li, Chair
Professor Anand Subramaniam
Professor Song Li
Professor Kara McCloskey, Primary Advisor

While bioprinting is well positioned for creating thick tissues and whole organs due to its scalability and geometric flexibility, it is limited in terms of microscale complexity. Reasons for this inadequacy includes limited resolutions, a lack of printable but biologically active materials, and a lack of use of stem cells. This issue permeates to vascularization, a universal requirement for artificial tissues, in which bioprinting has difficulty inducing microvasculature formation. In my dissertation, I address the lack of complexity in bioprinting by developing a multi-material bioprinter with novel features that improve resolution and embed hydrogels with concentration gradients of small molecules. I then print fragile induced pluripotent stem cells (iPSC), which are well-known for their propensity to self-assemble, and demonstrate their high viability in long term culture. I attempt to guide these iPSC towards vascular smooth muscle fate, but inadequate commercial antibodies forced me to pivot towards a study on characterization. Finally, I induce vascular network formation in printed endothelial cells and show the effects of printed VEGF concentration gradients on printed networks.

Table of Contents

List of Figures

Chapter 1: Introduction

Regenerative medicine is an emerging technology that aims to restore the natural functions of tissues typically by integrating stem cells or biomaterials to native tissues. Therefore, it is major impetus in the regenerative medicine field to produce implantable, organ-like structures that recapitulate the functions of native tissues [1]. This new technology may resolve some of the biggest issues in healthcare and drug development.

Firstly, artificial tissue can potentially relieve the unmet demands for replacement organs [2]. Currently, there are over 100,000 people on the United States national transplant waiting list where 20 waitees die each day [3]. Compounding this issue, there are numerous complications that can lead to the rejection of transplanted organs [4]. Regenerative medicine promises a solution by producing artificial tissue with stem cells. Pluripotent stem cells (PSC) can differentiate into any cell type found in the body and are thus able to form any tissue type. Unlike human organs, stem cells are infinitely renewable, curtailing the supply issues with natural organs. Furthermore, with the introduction of induced PSC (iPSC) [5], PSC can be sourced from the patient, thereby bypassing rejection issues [6].

Secondly, basic knowledge and tools acquired from regenerative medicine can be used to improve the research and development (R&D) process of traditional drug therapies [7]. Pharmaceutical R&D has been in a decades-long slump in productivity attributed to increasing difficulty and cost in development [8]. A significant factor to this issue is high attrition rates during the lengthy and expensive clinical trial process [9]. Many scientists believe these high failures rates can be mitigated with improvements to the drug-screening status quo of animal models and 2D cell culture. Functional, 3D tissue, such as those that regenerative medicine aims to create, can better bridge the disconnect between pre-clinical screens and clinical trials [10].

Herein lies the paradigm of regenerative medicine. PSC are first differentiated into multipotent stem cells or more specialized cell types [11–13]. Then these derived cells are embedded in hydrogels and patterned into the general geometry of product [14–17]. Over time in culture, these cells react to their new microenvironment by proliferating, self-organizing, and gaining functionality [18–20]. Finally, the result is implanted into an organism or used to screen synthetic compounds [21,22].

PSC are typically guided towards a specific fate via 2D cell culture and growth factors in the culture media. Although other methods, such as 3D cell culture and mechanical stimulation, are studied in the context of differentiation, 2D culture is the predominant method for generating PSC-derived cells because of its ease, lower cost, and scalability. Cell fates are typically guided via growth factors introduced in the culture media. However, a fraction of the population will always differentiate into unwanted cell types [23]. Furthermore, stem cell-derived cells tend to exhibit an immature phenotype [24] or incomplete functionality [25]. And progenitor cell lines are often difficult to identify and characterize [26,27]. Therefore, the challenge of cell differentiation is high efficiency differentiation that produces cells with similar characteristics to primary cells [25].

There are three primary methods of shaping a mass of cells into an organ-like structure: organoids, microfluidics, and bioprinting. Organoids formed when stem cells are placed in a 3D environment,

such as hydrogels, cell pellets, or embryoid bodies, and coaxed to differentiate and self-assemble into organ-like structures [28]. Organoids are the least “engineered” of these approaches as it lets natural, cellular processes create most of the pattern. As such, organoids are comparatively simple yet still recapitulates in vivo phenomena [29]. Microfluidic devices are small, micron-scale channels typically formed from molded polydimethylsiloxane (PDMS). Each channel can contain media, extracellular matrix (ECM), and cells [30]. This technique is exceptionally potent at manipulating the microenvironment as it can physically separate biological components while controlling interactions such as cell to cell communication [31] and signal gradients [32]. Bioprinting is the technique by which 3D printing is adapted to patterning biological matter, including live cells [33]. While it is the most flexible technique in terms of patterning geometry, it is limited in resolution by the requirement of using materials that are simultaneously printable but structurally sound [34].

Herein lies the issue with bioprinting: its techniques find difficulty integrating multiple cell types together to recapitulate the complexities of native tissue. Printed constructs typically lack the organic, self-assembled features of an organoid as stem cells are notoriously fragile to physical stresses [35,36] and the printability requirement limits cell densities and hydrogel materials [37]. Printed constructs also lack the resolution of microfluidic devices and cannot mimic the benefits of compartmentalization to manipulate the microenvironment [21]. Hence, in the context of biological complexity, bioprinting studies typically produce little more than cells encapsulated in 3D environments. Thus, bioprinting is currently ill-suited to manipulate the microenvironment of cells. Moving forward will require the issues of resolution and complexity to be addressed without compromising the advantages of flexibility and scalability that make bioprinting so conducive to organ engineering.

Although each technique is very different, the entire field of regenerative medicine shares the same problem of vascularization [38]. Thick tissues, no matter the method of generation, are subject to the 100-200 μm of oxygen diffusion and require perfusable vasculature to supply nutrients [39,40]. Therefore, thick tissue must necessarily be complex, multicellular constructs that integrate vascular cells with other cell types. The current paradigm is to interlace large vasculature (>100 μm diameter) with tissue via artificial patterning methods [16,41,42]. Meanwhile, capillaries that are smaller than the resolution of engineering techniques should self-assemble or sprout from the large diameter vessels [43–45]. Incorporation of these requirements in a scalable manner is the holy grail of vascularization in regenerative medicine.

The McCloskey lab has expertise in forming microvasculature within the compartmentalized environment of microfluidic devices [46]. These devices typically drive vasculogenesis of human umbilical vein ECs (HUVECs) via direct contact with fibrin gel and paracrine signaling from fibroblast cocultures [47]. The McCloskey lab is in the process of improving microfluidic vascularization by optimizing the different accessory cell types that are cocultured. Furthermore, the lab aims to bring this technology to bioprinting and incorporate microvasculature into bioprinter constructs. To do so, I will need to resolve the bioprinting issues related to biological complexity.

Furthermore, the McCloskey lab and most of the regenerative medicine field are inducing vasculogenesis with primary cell types. To move towards the long-term, clinical goals of the regenerative medicine field, PSC-derived cell types should be guided to vessel formation. The McCloskey lab has previously established a protocol for the chemically-defined generation of ECs

from human [23] and mouse [48–50] PSC sources. The protocol is multistage and first creates a kinase domain receptor (KDR) positive, multipotent progenitor before inducing EC fate. This KDR+ progenitor (also known as a vascular progenitor cell, VPC) is analogous to a cell in embryonic development's LPM and is known to be multipotent for both ECs and VSMCs [51]. Therefore, I can adapt this protocol for the generation of VSMC to provide PSC-derived accessory cell types for vascularization.

In my dissertation, I aimed to create a custom bioprinter that enables novel techniques for improving resolutions and manipulating the environment (Chapter 2). I demonstrate the printing of viable PSC in high resolution tissue constructs and guide microvasculature formation with a novel technique for bioprinting concentration gradients (Chapter 5). I also aimed to produce an efficient, reproducible protocol for the generation of vascular smooth muscle cells from PSC (Chapter 3) and address problems with the current methods of phenotype characterization (Chapter 4).

Chapter 2: ModiPrint: An Accessible, Feature-Rich, Multi-Material Bioprinter

Abstract

Three-dimensional (3D) bioprinting has brought major innovations to the field in its ability to fabricate cell-laden constructs that closely resemble physiological tissue. Unfortunately, many bioprinters print single or few cell-material combinations or at limited resolutions. Improving on the resolutions, functionality, and affordability necessitates attention to both printing techniques and printers. Here, I address this schism with my own, custom designed bioprinting system, ModiPrint. ModiPrint is a multi-material bioprinter that is feature rich through its highly custom control software and hardware design. ModiPrint enhances the biological cmplexity of its constructs by improving resolutions with novel stepper control software and embeding concentratrion gradients of small molecules in hydrogels. It still remains affordable, accessible, and modular through its 100% commercially availible component makeup that anyone can recreate using my documentation.

2.1 Introduction

2.1.1 Accessibility in Bioprinting

Bioprinting for tissue engineering applications has gained enormous traction in the scientific community. The technique's ability to generate cell-laden, organ-like constructs holds great promise for research and clinical use [33]. Specifically, bioprinting can precisely control the deposition of material and cells in three-dimensional space. This enables the automated design of anatomic structures and the manipulation of cellular microenvironments towards more complex, functional tissue constructs [52].

Advancing bioprinting requires either better materials that improve cell functions or structural properties, or better techniques that improve the resolutions and patterning of said bioinks [53]. As such, the bioprinting field has innovated a variety of materials with different mechanical properties, crosslinking ability, and cellular interactivity [54]. Similarly, there are different extrusion, inkjet, laser-based, and stereolithography techniques with different advantages of resolution, bioink compatibility, and flexibility [55]. For additional functionality, bioprinters have also mimicked physiological features such as concentration gradients [19,56] and vascularization [16,57].

To accommodate this variety of bioinks and print techniques, research groups often create purpose-built bioprinters that suit their specific research needs. Examples include multi-printhead machines for multi-material prints [58], a solenoid valve inkjet for micropatterning and gentle dispensing of stem cells [20], and temperature controlled printheads that manipulate the mechanical properties of thermoplastic materials [59]. This variety of machine designs and features is necessitated by a variety in bioprinting challenges.

However, the barrier of entry into bioprinting is high [60][61]. Custom, feature-rich bioprinters typically require specialized knowledge of software and hardware to construct. Meanwhile, commercially available alternatives for these machines remain expensive. And while many accessible bioprinters exist, they are often limited in functionality. For example, many studies use thermoplastic printers modified into motorized syringe extruders. These printers, while inexpensive and accessible, are limited to extrusion and single material prints.

2.1.2 Resolution in Bioprinting

Native tissues possess functionalities and characteristics that artificial tissues have not yet achieved [54]. For example, a major limitation in bioprinting is the lack of vascularization of thick tissues. As such, artificial tissues need to be unideally fabricated with negative spaces for nutrient diffusion, or risk cell death beyond the limits of diffusion [16]. Channels aside, native tissue is typically layered with different types of ECM and cell types. For example, the skin consists of multiple, interwoven layers of collagens, elastin, fibrin, embedded small molecules, fibroblasts and more [62]. And large diameter blood vessels possess distinct compartments of ECs, ECM-rich basement membrane, muscular tissue and connective tissue [63]. Recapitulating such complexity is key to representing proper functions for in vitro models and maximizing the healing potential of artificial grafts.

Higher resolutions enable more types of materials and patterns to be compacted into the same space, thereby increasing complexity and functionality. As such, the tissue engineering field is constantly trying to push the boundaries of resolution in 3D bioprinting. Typically, extrusion bioprinting yields

filament diameters of hundreds of microns [64][65][66]. In the context of tissue complexity, this is not even enough to meet the diffusion limits of nutrients (100 – 200 μm) [16] let alone mimic the complexity of multi-cellular tissue.

Increasing resolutions in bioprinting typically involves tuning the properties of the material and parameters of the print [34]. For extrusion bioprinting, the most popular technique, materials for the highest resolution prints are at a low enough viscosity that it is malleable to pressure but a high enough viscosity that dispense rates are controllable. The highest resolution materials typically crosslink quickly after print or is printed within a support bath [17]. To control resolution via extrusion printing parameters, the applied pressure, nozzle diameter, and XYZ stage traverse speed need to be optimized [67]. The lower the material flow rate, the lower the filament diameter. However, material needs to be flowing at a high enough rate such that it dispenses continuously and consistently.

2.1.3 Junction Resolution in Pressure-Driven Extruders

A seldom explored issue with pressure-driven extruders is that straight line resolutions are not necessarily representative of resolution in constructs of complex geometries. The curves of organ-like shapes necessitate many line segments which forces XYZ stages to slow down below their intended print speed. All the while, pneumatically driven printheads maintain the same dispense rates via a constant pressure acting on the reservoir. These transitions between line segments, hereby referred to as junctions, necessitate stepper motor operations to slow to a stop then reaccelerate while maintaining linear acceleration. As opposed to non-constant stepper motor speeds, pressure-driven extruders maintain a constant dispense rate. To my knowledge, only one publication has acknowledged this excess material deposition phenomenon with no proposed method to mitigate it [61]. However, other publications display this phenomenon with figures of their prints which showcase uneven material deposition at junctions [64,65].

My proposed methods on improving junction resolutions requires a combination of hardware and software optimizations. Hardware optimizations included a stiff frame, which increases junction speeds, and high torque motors, which decrease acceleration time. This chapter will discuss software optimizations which involve implementation of a junction algorithm enabling the maintenance of higher, more consistent speeds around junctions. The physical result causes stepper motor operations to slow to non-zero junction speeds, thereby reducing the effects of excess material deposition (**Figure 2.1**).

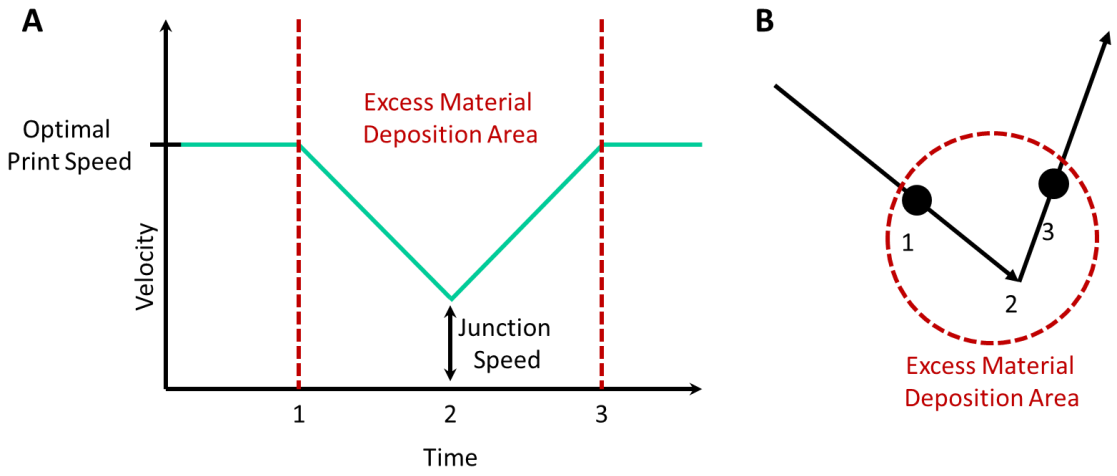

Figure 2.1 *Excess material deposition caused by the non-constant movement speed of the XYZ stage.* ***A)*** *Velocity profile of stepper motor operations during the transition between line segments. As the stepper motor approaches the intersect between line segments, it decelerates to the junction speed. After the intersect, it must accelerate to the print speed. The deceleration and acceleration below the optimal print speed causes excess material deposition.* ***B)*** *Plot of the printhead trajectory and the area affected by excess material deposition. Points 1-3 correspond to the points in Figure 2.1A.*

2.1.4 Software Requirements for High Speed Junctions

This essential fast junction capability must be custom built for a custom machine. However, even the more powerful of plug-and-play microcontrollers are resource limited and cannot perform the complex calculations for fast junctions in a timely manner. Herein lies another issue: maintaining accessibility while maximizing junction resolution requires innovations to stepper motor control software. This custom stepper control software is designed to maintain consistently high speeds around long sequences of linear movements. This necessitates that software calculate the highest possible junction speeds and incorporate them into movements without interruptions. In the resource limited setting of a microcontroller, there are several challenges that must be addressed:

1. Efficient Δt Calculations: Executing linear acceleration for a smooth movement requires calculating Δt, the time in between steps. There is not enough memory in the microcontroller to buffer all Δt values, therefore, Δt must be calculated in real time. Equation S1 calculates the Δt values for perfect linear acceleration.

$$\Delta t = \sqrt{\frac{2n}{a}} - \sqrt{\frac{2(n-1)}{a}} \quad (Equation\ 2.1)$$

Where a is acceleration and n is total step count.

However, the slow processor of a microcontroller necessitates efficient estimations of Δt values else the calculation time exceeds Δt itself and limits the stepper motor maximum

speed. Efficient calculations will minimize square roots, floating-point values, and division operations; therefore Equation 2.1 cannot be used.

2. Smooth Movement: Smooth movement via linear acceleration is necessary to maintain the precision of stepper motors. This is especially true when the XYZ stage is subject to the stresses of above zero junction speeds.
3. Buffering Movement Parameters: Tool paths of organic shapes typically involve sequences of short linear movements. These short movements can be physically executed more quickly than that time it takes to process and calculate movement parameters and stall the program. When XYZ operations are stalled, consistently high speeds are no maintained and excess material deposition occurs. Therefore, the ability to buffer movement parameters will better allocate the longer time allowed in longer movements to be used to calculate future short movements. Longer buffers require less memory usage for movement parameters, which necessitate more information that can be calculated and consumed in real time as opposed to stored.
4. Fast Junctions: A method must be implemented such that slow movement in between linear movement transitions are minimized. This must be implemented in such a way that maximizes transition speeds with minimal compromise to precision.

While these issues could be resolved with more powerful microcontrollers, a commercially available option is not yet available. The plug-and-play of the Arduino was necessary to maintain the affordability and accessibility of the bioprinter design. Furthermore, its ubiquity and corresponding abundance of documentation was instrumental in easing me into an otherwise arcane skillset. Moreover, more powerful microcontrollers typically operate at lower voltages. Lower voltages are more susceptible to noise, which was already a significant issue that necessitated filters given the numerous electronics and compactness of the bioprinter design. Regardless of these issues, the more powerful plug-and-play microcontroller is likely not be powerful enough to overcome these challenges.

Current custom bioprinters with even a modicum of atypical features are accompanied by custom control software [68] or modified versions of open source software [61]. Typically, the requirements for controlling an arbitrary number of pneumatics and actuators, integration with a custom language, and other common features prevent generic scientific equipment from being sufficient.

Furthermore, commercially available XYZ stages and controllers are not typically built with this fast junction functionality. These functions provide small increases to the operation time while increasing the risk of stepper motor slips [69]. Therefore, stages typically designed for precision, scientific equipment, and automation do not feature this functionality. Operations that require long sequences and movements, such as computer numeric control devices, may very rarely feature this function as the cumulative time savings are insignificant. However, even if a software does possess such features, none are designed as portable libraries and are, therefore, difficult to integrate with custom machines.

2.1.5 A Lack of Concentration Gradients in Bioprinting

Concentration gradients play an important role in the cell's microenvironment by directing various cell fates and functions. In vivo, concentration gradients play a critical role in the organization of tissue during embryonic development, wound recovery, and vascularization [70–72]. In line with

goals of regenerative medicine, recapitulating concentration gradients can provide new techniques for guiding the self-assembly and functionalizing of artificial tissue.

These gradients have been mimicked in a variety of microfluidic devices. However, artificially generating these gradients requires systems that expose cells to multiple channels of media, serial dilution devices [32], or the patterning of multiple materials of different concentrations [19]. Hence, concentration gradients have been demonstrated with very few bioprinting studies. Furthermore, these techniques are complex with a limited choice of geometries of the gradients and the containing structures which is counter to the appeal of bioprinting.

Applying concentration gradients while retaining the flexibility of bioprinting would allow the field of regenerative medicine to better recapitulate the microenvironment of native tissues and integrate those environments into scalable, artificial tissue. This necessitates a new bioprinting technique and machinery to support it.

2.1.6 A Need for a Better Bioprinter, ModiPrint

These issues of accessibility, resolution, and concentration gradients can collectively be resolved with improvements to bioprinting hardware and software.

Here, I present ModiPrint, an open-source bioprinting system that is both accessible and feature-rich. It features a modular, open-ended design with multiple printhead types and printheads mounted on independent Z actuators. The build is compact enough to fit within the sterile confines of a biosafety cabinet and viably dispense hiPSC. The design consists entirely of inexpensive, commercially available parts, with our own 4 printhead system costing under $4,000 (not including the cost of our own commercialized firmware). All operation is guided by an easy to use, custom GUI-based desktop software that is integrated with open source slicing software.

I demonstrate that ModiPrint can produce high resolution, 100 μm alginate filaments. I improve the resolution around corners with software and hardware features that allow for high accelerations and fast cornering. A novel stepper control program allowed me to leverage these features even on a resource limited microcontroller.

Finally, I created a new technique that is enabled by ModiPrint's combination of extrusion and drop-on-demand printing styles. It is capable of embedding 3D small molecule concentration gradients of any geometry into a hydrogel patterned in any geometry.

2.2 Materials & Methods

2.2.1 Design Criteria

This bioprinter was initially intended as a custom device for our lab. I sought to create a multi-material bioprinter that's gentle enough to print pluripotent stem cells. Operation with live cells necessitated a compact build that could fit within the confines fo a biosafety cabinet. It needed to print complex geometries which required integration with computer aided design. It needed to be able to manipulate the microenvironment of printed cells which manifested as novel features that improved resolution and generated ceoncentration gradients. Altogether, these custom features necessitated a highly custom desktop control program and embedded software.

The suite of custom features required the hardware to deviate from typically-used scientific equipment. Instead, the hardware was built with generic components from vendors such as Openbuilds and McMaster Carr. I realized that this machine could be built purely from commercially availbile parts, making it well suited to be an affordable, open source device that other groups can replicate. This necessitated thorough documentation for the open source model and for other members of my lab to operate the device after my leave.

2.2.2 Hardware Design

Before assembly, the bioprinter's design was built in the CAD program, Sketchup using 3D models of commercially available parts that were provided by the vendor or drawn by me. Almost always, the design process was an iterative loop of CAD design followed by physical assembly, then redesign and reassembly.

ModiPrint's structural frame and many actuators are a custom arrangement using modular, V-slot based hardware primarily sourced from Openbuilds. The pneumatic circuitry and control are sourced from many different manufacturers and drives precision dispensing components from Pneumadyne, Nordson EFD, and The Lee Co. Other miscellaneous generic components were sourced from McMaster Carr and other vendors. The electronics suite is built around an Arduino MEGA with various easy to wire drivers and power sources. All parts are commercially available components.

The assembly process consisted of simple tools such as Allen wrenches, taps attached to power tools, wrenches, basic soldering equipment, etc.

2.2.3 Software Design

ModiPrint's software suite consists of a custom GUI-based desktop program that streams programming language to a custom microcontroller program. The final desktop program was designed in the Visual Studio 2017 IDE (integrated development environment) and written in C# using the .NET Framework 2.5 and Windows Presentation Foundry. Earlier iterations used WinForm. The final microcontroller program was designed in Atmel Studio 6.0 and written in C. Earlier iterations were designed in the Arduino IDE. The codebase was built with an emphasis on clean design for readability and ease of edit. Therefore, the desktop program was written with the Model-View-Viewmodel architectural pattern and all code is thoroughly commented and adheres to Object-Oriented Programming standards as best as possible.

2.2.4 Documentation

All documentation for hardware assembly, operations guides, and source code for software is accessible online (www.modiprint.com/documentation). The user guide was designed in Word. Hardware assembly is guided by 3D models produced in Sketchup. Wiring and pneumatics diagrams were created in PowerPoint. The parts list consists of a macro-based price calculator written in Visual Basic for Applications built in Excel.

2.2.5 Stepper Control Equation Simulations

Error calculations of each Δt equation is done in Excel. Simulations of the calculation speeds and verification of each error equation is done with Atmel Studio's virtual simulation tools.

2.2.6 Preparation of Hydrogel and FRESH Support Bath

Alginate solution, 2% (w/v), was prepared by gently stirring alginic acid powder (Sigma 180947) with phosphate buffered saline (PBS) at 65°C. FITC-labelled alginate was created by mixing 0.1% (w/v) FITC powder (Sigma) with 2% alginate solution at room temperature. For viable prints, 2% RGD-linked alginate was used (NovaMatrix VLVG GRGDSP). To visualize the material, food coloring is sometimes suspended within the solubilized alginate.

All prints in this study used the freeform reversible embedding of suspended hydrogels (FRESH) gelatin support bath which was created according to the protocols of Hinton et al. [15] 4.5% (w/v) gelatin solution was created by gently stirring gelatin powder (Difco) with 11 mM CaCl2 (Sigma) in deionized water at 65°C. 30% of a 16 ounce mason jar was filled with the gelatin solution and solidified at 4°C overnight. The resulting gelatin puck was separated from its container and the mason jar was filled with 11mM CaCl2 solution before chilling at -20°C for ~40 minutes. The chilled contents of the mason jar were blended in an Oster Beehive blender (Oster) for 2 minutes. The resulting gelatin particle solution was centrifuged at -5°C at 3000G for 4 minutes. The supernatant was aspirated, and the gelatin particles were washed once with 11 mM CaCl2. The modification to the original protocol is that the support bath is cooled at 4°C for 24 hours before plating. Plated support baths are centrifuged at 1500G to evenly distribute the gelatin particles across the plate.

2.2.7 Bioprinting Process

3D models were designed in AutoCAD 2017 or taken from Free3D and converted to g-code via Slic3r 1.3.0. Some g-code used for 2-dimensional prints were written by hand. G-code was further processed with our custom desktop program to generate the custom commands language that is streamed to the microcontroller.

Only high-resolution parameters that generate ~100 μm diameter filaments were used in study. For the pneumatic extruder dispensing normal alginate, these parameters were 12 mm/s print speed, 2000 mm/s2 acceleration, a 0.01 junction deviation, and a 100 μm inner diameter chamfered nozzle (Nordson EFD). As RGD-linked alginate was less viscous, pressure was decreased to 3 psi and print speed increased to 25 mm/s to maintain high resolutions.

For generating concentration gradients, the microdispensing inkjet used ModiPrint software parameters of 500 μm droplet spacing and an exponential gradient with 35% strength, along with 5 psi, and a 100 μm inner diameter nozzle (The Lee Co.).

All prints were performed at room temperature with a 4°C. FRESH support bath. The petri dish containing the support bath is secured to the print surface. The print sequence begins immediately after the nozzle moves to starting position. Embedded constructs were placed in a 37°C incubator until the support bath was fully dissolved. Dissolved baths are aspirated, and printed constructs are washed with PBS before culture or analysis.

To achieve sterile prints, the bioprinter was moved inside a laminar flow biosafety cabinet. The bioprinter was exposed to UV light for 5 minutes before being thoroughly wiped with 70% ethanol. All syringe and nozzle components directly in contact with the hydrogel and cells were autoclaved. A HEPA filter was installed upstream of the syringe barrel and all pneumatic circuitry downstream of the HEPA filter was autoclaved.

2.2.8 Imaging and Resolution Characterization

Characterization of alginate filament resolution was performed with an inverted phase contrast microscope (Fisher Scientific) and measurements were performed with the imaging software's (Micron, Westover Scientific) digital measurement tools. Fluorescent images were taken with an epifluorescence microscope (Nikon TEU-2000) and NIS Elements AR 3.2.

2.2.9 Cell Culture and Fluorescent Staining

DF-10-0-7T human induced pluripotent stem cells (hiPSCs, WiCell) were cultured with mTeSR1 without antibiotics (Stem Cell Technologies) on a substrate of human embryonic stem cell (ESC)-Qualified Matrigel (Corning) at 37℃ under 5% CO2. Culture medium was refreshed every day and cells were sub-cultured every 3-4 days using Accutase (Stem Cell Technologies) as the lifting reagent. Printed hiPSCs were similarly maintained with daily refreshment of mTeSR1 at 37°C under 5% CO2.

Human iPSCs were fluorescently-labelled immediately before printing with CellTracker Green (Invitrogen) according to manufacturer recommendations. Viability assays were performed with LIVE/DEAD Kit for Mammalian Cells (Invitrogen) after washing printed structures with PBS and in accordance to manufacturer protocol. Viability assays were not performed with fluorescently-labelled hiPSC.

For flow cytometry, printed hiPSCs were first dissolved with a solution of 50 mM trisodium citrate dihydrate (Sigma) and 104 mM sodium chloride (Sigma) in PBS for 10 minutes in 37C, then cell clumps were dissociated with Accutase (Stem Cell Technologies) for 5 minutes at 37°C.

2.2.10 Statistical Significance

All statistical significance was performed with unpaired, two-tailed, heteroscedastic, student's t-Tests.

2.3 Results & Discussion

2.3.1 Design of ModiPrint

2.3.1.1 A Failed First Iteration

The first iteration of the custom bioprinter was based around the work of Faulkner-Jones et al. [73] who reported the first viable printing of hiPSC. They used fast acting, microdispensing VHS solenoid valves from The Lee Co. which dispenses with mild pressure and no other unnecessary forces. Therefore, I sought to build a multi-printhead bioprinter based around the VHS valve from The Lee Co.

The very poorly conceived design used a stripped PrintrBot as the XYZ stage. The thermoplastic extruder and electronic drivers were removed to accommodate modifications. DRV8825 stepper motor drivers replaced the removed drivers and a VHS valve was mounted in place of the thermoplastic extruder. However, mounting 4 printheads was not feasible as the PrintrBot was too small as a platform. Furthermore, the PrintrBot had subpar resolutions of 60 µm which did not fit the criteria of micropatterning.

The software to control the new device consisted of two parts: a desktop program and a microcontroller program. The desktop program was a GUI-based program written in C# using the .NET framework and WinForms. Although this program necessarily required a sizeable code base, I did not follow standards for creating scalable code. Quickly, this program devolved into a spaghetti of untenable bugs and scaling issues and had to be abandoned.

The microcontroller program was created with the Arduino library and controlled stepper motors with AccelStepper. The AccelStepper library had severe limitations in controlling stepper movement (detailed in Chapter 4). Particularly, AccelStepper was severely limited in its ability to drive stepper motors at sufficient speed. Furthermore, AccelStepper had no support for synchronizing multi-stepper movement.

Altogether, the first design was necessarily scrapped. A major design flaw was the overreliance on prebuilt components for a highly custom device. The next iteration, named ModiPrint, uses more custom arrangements for specialized features and better coding practices. Each aspect of ModiPrint was designed from scratch to accommodate the multitude of specialized features. To retain the ease of accessibility, all parts are commercially available with little modification required.

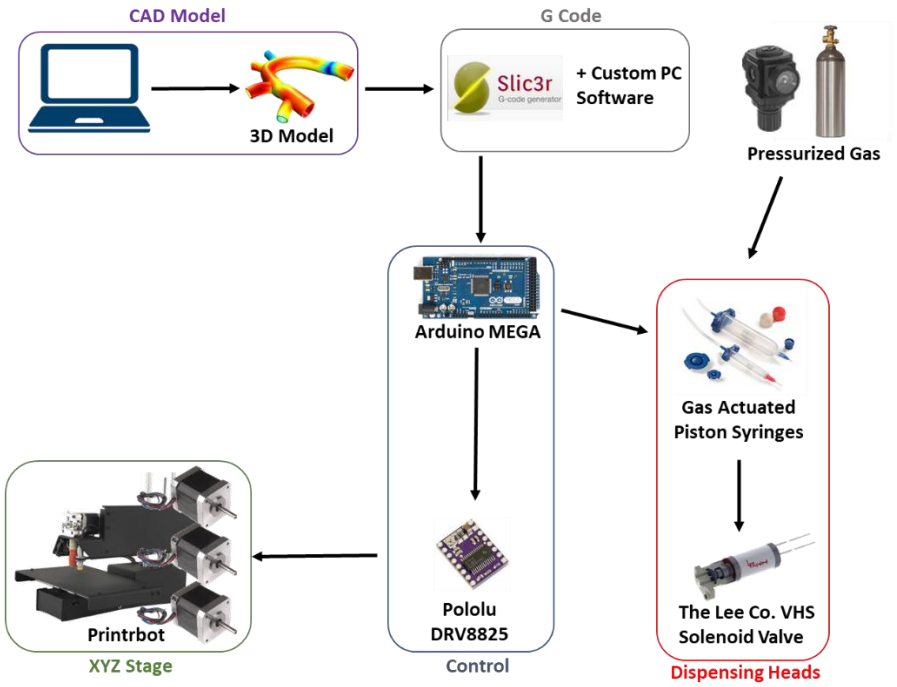

Figure 2.2 *Simplified diagram of the 1st iteration of the bioprinter design. Sliced computer-aided design (CAD) models are streamed to custom control software which operate a pressurized, valve-operated reservoir and XYZ stage synchronously.*

2.3.1.2 XYZ Stage Design

ModiPrint's XYZ stage is a custom design that is built primarily with modular V-slot components from Openbuilds. These V-slots enabled the many components of the bioprinter to be mounted at almost any location, improving the ease of assembly and accessibility of the design.

After several iterations, the final design uses two parallel Y actuators that acts are the bioprinter's structural frame and carries the heavy load of an elevated X actuator and a variable number of Z actuators (**Figure 2.3A**). While typical XYZ stage designs would give one or more planes of movement to the print surface, ModiPrint directs all movement to the printheads. This decouples potentially jerky movements from disturbing the printed material. Unlike conventional 3D printers, a bioprinter's printed material is comparatively soft and mechanically unstable. Therefore, this design prevents printed materials from being disturbed by XYZ stage movement.

The Z actuators are a custom design that uses Openbuilds parts but an arrangement unintended by the vendor (**Figure 2.3B**). The result is a very compact Z actuator with a width of ~60 mm. This was necessary because a multi-material bioprinter printing within the confines of a walled container (i.e. a petri dish) requires multiple printheads mounted on independent Z actuators. The multiple Z actuators must be compact else the bioprinter's frame would not fit within the sterile confines of a biosafety cabinet (**Figure 2.3C**). The total dimension of the bioprinter is less than 600 mm width by 600 mm length by 700 mm height.

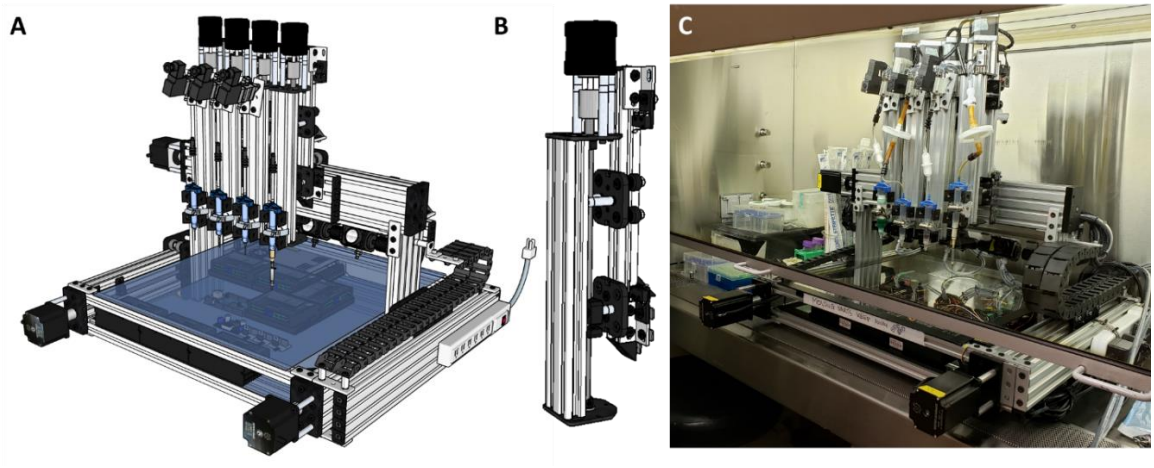

Figure 2.3 *Design of the XYZ Stage.* ***A)*** *CAD model of the bioprinter.* ***B)*** *Image of the CAD of the Z actuator.* ***C)*** *Image of the bioprinter within the compact, sterile environment of a biosafety cabinet.*

2.3.1.3 Printheads Design

ModiPrint's software supports the use of motor-driven printheads and valve-based printheads. I have designed and physically constructed two valve-based printheads, the pneumatic extruder and microdispensing inkjet, but have no designs for motor-driven printheads.

The pneumatic extruder is a pressure-driven extrusion printhead inspired by the precision dispensers of Nordson EFD (**Figures 2.4A and 2.4B**). The material rests within a disposable syringe barrel downstream of a 3/2 solenoid valve. In the ON state, the solenoid valve redirects a

pressurized gas source through a filter and into the syringe barrel. The pressurized syringe barrel dispenses material through a nozzle that is directly attached to the syringe barrel. In the OFF state, the solenoid valve exposes the syringe barrel to a vacuum source. This ensures that the printhead ceases dispensing immediately upon signal cutoff, and while idle, does not leak less viscous fluids.

The pneumatic extruder was designed for extrusion bioprinting of viscous materials. Downstream of the solenoid valve, every component is autoclavable and the pneumatics can fit a high efficiency particulate air (HEPA) filter (**Figure 2.4G**). As a result, this printhead can be adapted for sterile prints. A key feature of this printhead is the ability to modulate input pressure and print with single digit psi pressures. Furthermore, dead volume is minimized as the material reservoir is directly adjacent to the point of dispensing. This allows for the gently dispensing and minimization of shear forces to printed cells [20].

The microdispensing inkjet consists of a fast-acting, two-way VHS series solenoid valve from The Lee Co. directly downstream of a syringe barrel material reservoir (**Figure 2.4C and 2.4D**). This solenoid valve has a minimum open-close cycle time of single digit microseconds. This enables the valve to dispense miniscule volumes of fluids reported as low as the nanoliter range [73].

The microdispensing inkjet was designed for droplet bioprinting of low viscosity or aqueous materials. While the VHS solenoid valve cannot be autoclaved, it can be flushed with bleach or ethanol, much like the sterilization process of a flow cytometer. More importantly, the low droplet volumes enable the concentration gradient feature (to be discussed in Chapter 3) or other forms of micropatterning.

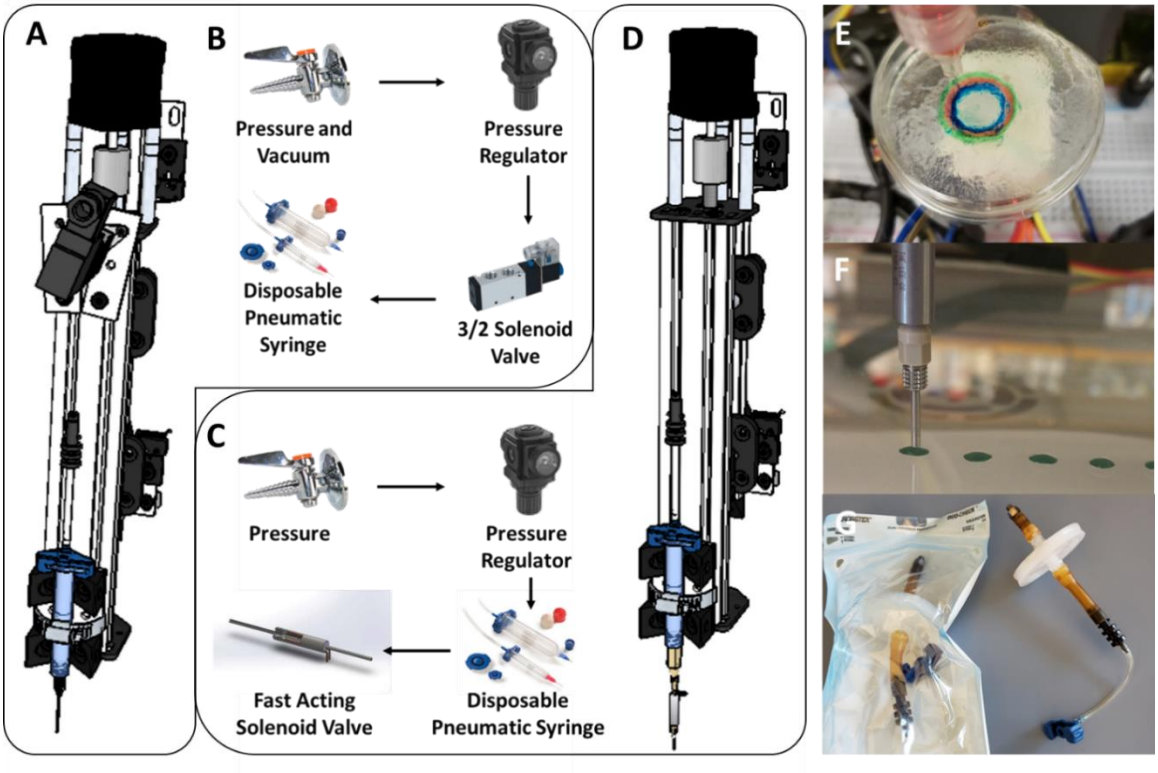

Figure 2.4 *Design and showcase of ModiPrint's valve-based printheads.* ***A)*** *CAD model of the pneumatic extruder.* ***B)*** *Diagram of the pneumatic extruder's pneumatic circuitry and primary components.* ***C)*** *Diagram of the microdispensing inkjet's pneumatic circuitry and primary components.* ***D)*** *CAD model of the microdispensing inkjet.* ***E)*** *Multi-material extrusion printing of dyed alginate in a sacrificial scaffold using the pneumatic extruder.* ***F)*** *Droplet printing of an aqueous solution using the microdispensing inkjet.* ***G)*** *Autoclavable components of the pneumatic extruder.*

2.3.1.4 Electronic & Pneumatic Circuitry

ModiPrint drives its hardware components with generic, plug-and-play drivers. The pneumatic circuitry also uses generic parts in line with the theme of affordable cost and ease of accessibility. Although most connections are easily screwed or plugged into their designated connections, there is a significant amount of splicing and soldering required for this custom circuitry.

At the heart of the bioprinter is a microcontroller with custom control software. 5V signals originate from this controller based on a custom programming language streamed from a desktop program. These 5V signals control the actions of various drivers which draws power from various power supplies to operate solenoid valves, stepper motors, and limit switches.

For stepper motor operation, the microcontroller sends pulses to a stepper driver where each pulse drives a single step of the motor. The driver is a two-phase hybrid driver powered by a 24V, 14A power source. For the X and Y actuators, it drives a 4 wire, bi-polar NEMA 23 stepper motor with a 1.8 step angle and a high 345 oz-in of torque. The high torque is a necessary part of the design to retain high resolutions in geometrically complex prints (detailed in Chapter 2.3). For the Z actuators, the stepper driver drivers a 4 wire, bi-polar NEMA 17 stepper motor with a more precise 0.9 step angle and 68 oz-in of torque. This higher precision stepper motor allows for a higher resolution in the Z axis as extruded filaments often sag and have a thinner height than width. With $1/8^{th}$ microstepping, Z actuators have a theoretical resolution of 5 µm whereas XY have 10 µm.

The 3/2 solenoid valve of the pneumatic extruder printhead receives simply toggles states based on a 24V (ON) or 0V (OFF) signal. To translate the 5V signal of the microcontroller to a 24V signal, the 5V signal first passes through a MOSFET driver. The driver redirects the power from a 24V power source to the solenoid valve only when the driver has received a 5V signal from the microcontroller. To avoid damaging the solenoid valve, a lower amperage (1A) power source is connected to the MOSFET drivers.

The VHS solenoid valve of the microdispensing inkjet must be driven by a spike and hold driver that outputs a specialized waveform. The spike and hold driver, alike the MOSFET driver, only toggles the solenoid valve to the ON state upon receiving a 5V signal from the microcontroller. It also redirects power from a 24V, 1A power source during this OFF to ON transition. However, it quickly lowers the operating voltage by redirecting to a much lower voltage (3.2V – 2.5V) power source to prevent damage to the sensitive valve. This lower power source is supplied by the microcontroller's 5V reference voltage after translation to a lower voltage via an adjustable converter.

Each printhead is operated by different gas pressures as each material may have different dispensing requirements. Therefore, each solenoid valve is connected to a different gauge. All

pressure gauges take an input pressure from a manifold which takes its input pressure from an outside source. A single vacuum can universally operate all pneumatic extruders, even if each printhead is loaded with different materials of varying viscosities. Therefore, all solenoid valves vacuum inputs come from a manifold which takes its input vacuum from a single vacuum gauge which takes its input from an outside source. All manifolds are mounted behind the X actuator and all gauges are easily accessible below the X actuator.

Limit switches are placed at the ends of each actuator. While the limit switch is not pressed, the circuit redirects the microcontroller's 5V reference voltage back to one of its GPIO pins. When pressed, the limit switches return a grounded (0V) signal whereby the microcontroller ceases stepper motor operations. The McCloskey lab's bioprinter features 8 actuators, 3 3/2 solenoid valves, 1 VHS solenoid valve, and 10 limit switches with accompanying drivers and power sources within compact dimensions. This poses a signal processing challenge where adjacent electronics create noise for limit switch inputs. Therefore, passive high pass filters are installed within each limit switch circuit.

With this amount of equipment, the bioprinter requires hundreds of wires and tubing. Given the compact dimensions of this device, these connections must remain organized, especially during operation where large sections of the bioprinter is moving. As such, for all equipment that is mounted on the X actuator, their wires and tubing passes through two drag chains to the electronics compartment underneath the print surface. For safety, all power supplies are connected a wall outlet via a generic power strip that is mounted conveniently on the device. A press of the power strip's activation switch will deactivate or power all components of the bioprinter.

All electronic and pneumatic wiring diagrams can be found in the user guide.

2.3.1.5 Desktop Software Design

ModiPrint's desktop software was written in C# using the .NET Framework 2.5 and Windows Presentation Foundry. In this sizeable codebase, debugging and scalability issues were present in the first iteration. To avoid these issues, ModiPrint's software follows the Model-View-ViewModel structure which enforces object-oriented programming conventions.

ModiPrint's desktop program serves several primary functions:

1. Takes g-code inputs and translates them into ModiPrint's custom programming language.
2. Takes user inputs for operation of the bioprinter.
3. Streams ModiPrint's custom programming language to the microcontroller.
4. Relays information from the microcontroller to the user.

A major function of the desktop program is to serve an intermediary between the translation of a CAD model and ModiPrint's hardware execution (**Figure 2.5A**). At the start of this workflow, users create a CAD model with the CAD program of their choice and convert it to g-code via a variety of other open source slicing software. ModiPrint's desktop program is fully compatible with the RepRap flavor of these g-code outputs and can therefore fully integrate with the features of these slicing tools. ModiPrint's desktop program can then generate ModiPrint's custom programming language based on the g-code and user inputs. These ModiPrint messages enable special features (droplet printing, concentration gradients, control of multiple Z actuators) and are

streamed, in real time during operation, to the microcontroller. The microcontroller then interprets these ModiPrint messages and signals the hardware to act.

This workflow is necessary for the user to print geometries that is otherwise impossible due to the complexities of generating tool paths. ModiPrint's custom programming language also possess special features that enable the user to write their own tool paths for simple geometries or specialized prints where slicing tools are inapplicable.

ModiPrint is intended to be modular and customizable by the user. Therefore, the desktop program can accommodate a variety hardware designs and print parameters (**Figure 2.5B**). To do so, it allows the user to specify any number of printheads, whether each printhead is motor-driven or valve-based, and operating parameters for each printhead as well as the XYZ stage. It also allows the user to specify a variety of print parameters such as print speeds, print styles (extrusion vs. droplet printing), and tool path. It also offers the user a control panel for setup, manual operation, and calibration that also displays information such status information and return messages from the microcontroller (**Figure 2.5C**).

The graphical user interface (GUI) was written in XAML and created within WPF. The color scheme was inspired by the dark color themes found in many IDEs and heavily integrated with my favorite color, turquoise. The user guide follows a matching, whimsical theme.

As much as possible, the GUI was designed to be intuitive. For example, many buttons and features are hidden or disabled until operations reach the point of their relevancy. Tooltips are embedded within every button, giving a short explanation for the user. To keep the GUI responsive, lengthy background features, such as serial communications and g-code conversion, is offloaded to a new thread. Ease-of-use was iteratively improved with feedback from non-engineer members of the lab.

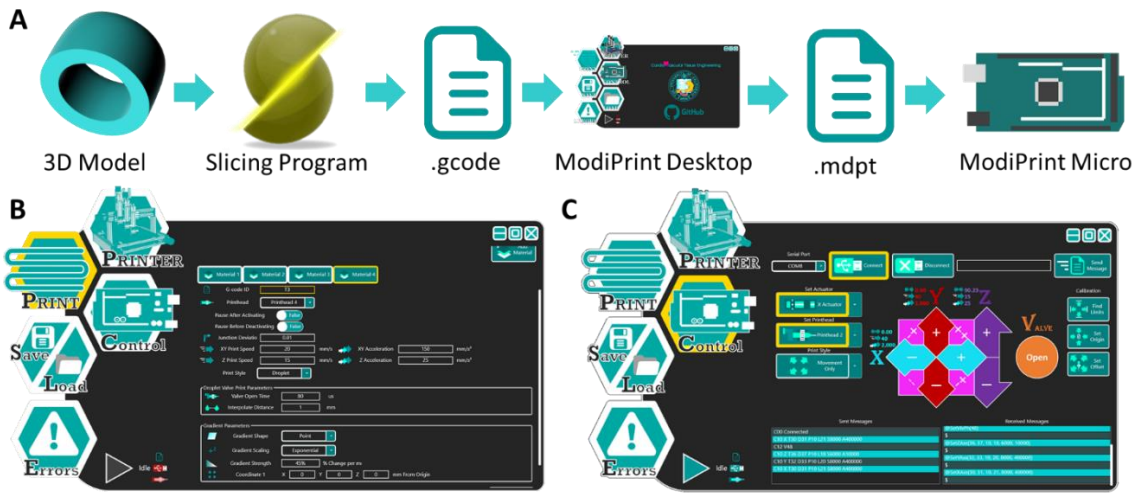

Figure 2.5 A) *Diagram of ModiPrint's software workflow that translates CAD models into machine operation.* ***B)*** *Screenshot of ModiPrint's desktop program's print settings menu and* ***C)*** *control panel.*

2.3.1.6 Microcontroller Software Design

The microcontroller program was written in Atmel Studio 3.0 and written in C using Atmel and C standard libraries. In its first iteration, there were performance issues caused by an inefficient program being run on a resource-limited microcontroller. Therefore, ModiPrint's microcontroller software is written with a focus on resource efficiency.

ModiPrint's microcontroller program aims to translate a custom programming language streamed from the desktop program into signals for hardware operations. If the program does not calculate signal timings in a timely manner, hardware operations will stall and have adverse effects on print quality. Furthermore, the XYZ stage must maintain high speeds in between linear movements to reduce excess material deposition (detailed in Chapter 3) which necessitates the software implementation of high XYZ stage speeds around junctions. Fast calculations required a novel stepper control algorithm that approximates linear acceleration (detailed in Chapter 4).

ModiPrint's microcontroller program requires a way to communicate the with desktop program that streams messages, buffering systems to store those messages, the ability to parse and interpret the messages, functions to calculate stepper movement, and an efficient stepper movement protocol. As the novel stepper control algorithm necessitates a different form of data buffering from other comparable open-source software, these components needed to be rebuilt from scratch.

All these processes act asynchronously and necessitate what is essentially multi-threading on hardware and frameworks that do not support it. Fortunately, Atmega's hardware features timers which can be programmed to execute functions when a hardware timer counts to a programmed number of cycles. This feature devolves the program into a spaghetti of triggers that loops the execution of various protocols (**Figure 2.6**).

The asynchronous protocols and their features have the following priorities where lower numbers are executed before higher numbers:

1. Pause Protocol: Protocol to halt all operations for a specified time.
2. Stepper Operation 1: Protocol to calculate Δt, rasterize stepper movement, and execute stepper movements from a movement buffer.
3. Stepper Operation 2: Protocol that follows Stepper Control 1 to turn off step pins.
4. Serial Communication: Handles receiving and sending data. Receive functions are executed when incoming data is present in the serial buffer. Send functions are executed when other protocols necessitate the sending of data.
5. Valve Control: Controls valve operations that are independent of printing and movement.
6. Main Loop: Responsible for parsing and interpreting incoming messages as well as checking system flags and buffers during idle time.

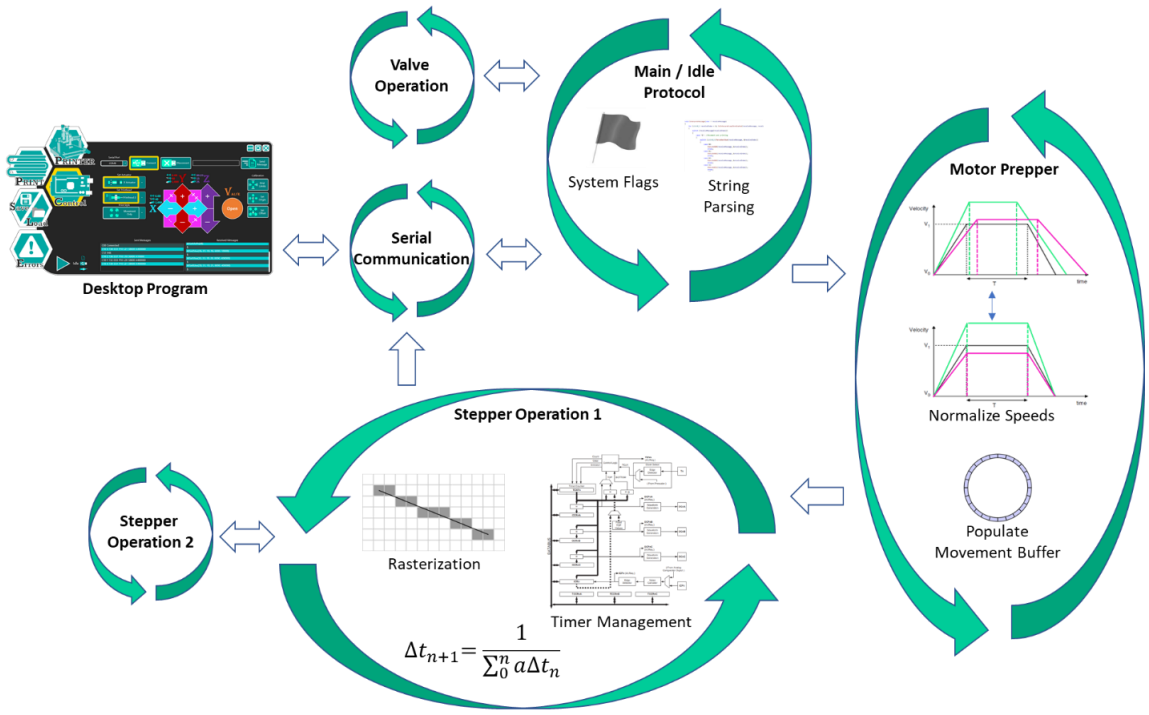

Figure 2.6 *Diagram representing the various asynchronous processes of the microcontroller program.*

2.3.1.7 Serial Communication Protocol

ModiPrint's desktop program and microcontroller program can stream hundreds of messages every second via serial communication. This necessarily occurs during hardware operations as the microcontroller has limited memory and must receive and interpret information for a print sequence in pieces. This well-optimized serial communication protocol is necessary to prevent stalls during printing which can lead to the unwanted deposition of excess material.

Microcontroller Serial Communication Protocol

The serial communication protocol is one of the self-contained, asynchronous processes in this microcontroller program. Its primary purpose is to communicate with the desktop program, either to receive new messages or to signal that certain protocols have been executed.

In the case that a new message is received, a message received protocol fires asynchronously to store the next serial byte into a serial incoming message ring buffer. If there are no other time sensitive operations to perform, the message received protocol will loop until the serial communication buffer in the hardware is transferred byte by byte to the RAM.

In the case that a new message needs to be sent by the microcontroller, a send message protocol fires within the main protocol. The message in question is stored into a serial outgoing message ring buffer and a timer is primed to fire whenever the serial communication hardware is ready to send another byte. This timer's protocol consumes the serial outgoing message ring buffer and shuts itself off when the ring buffer is empty.

To prevent multiple timers from overwriting the outgoing message ring buffer, only the main protocol can access the buffer. If a protocol outside the main protocol needs to call serial communications, they store their message in other buffers. The main protocol, when idle, transfers these other buffers to the primary buffer and executes the serial communication protocol.

Desktop Serial Communication Protocol

The desktop program has a similarly self-contained, asynchronous process. Unlike the microcontroller, the basic process of streaming messages is made easier by the .NET framework. To prevent overwhelming the microcontroller, the desktop program only sends messages if the microcontroller program signals that it is ready to receive a message. This ensures that the microcontroller's buffer is filled as much as possible without overflow and loss of data.

Whereas the microcontroller controls the pace of this process based on hardware requirements, the desktop program controls the pace based on user inputs for starting, pausing, resuming and aborting serial communications (and consequently, hardware operations). Starting and resuming simply begins the back and forth stream of messages. Pausing stops the streams and sends a message which tells the microcontroller to halt its operations as soon as hardware operations allow. Aborting sends a message to the microcontroller stops the streaming process immediately and both programs clear their buffers and message queues.

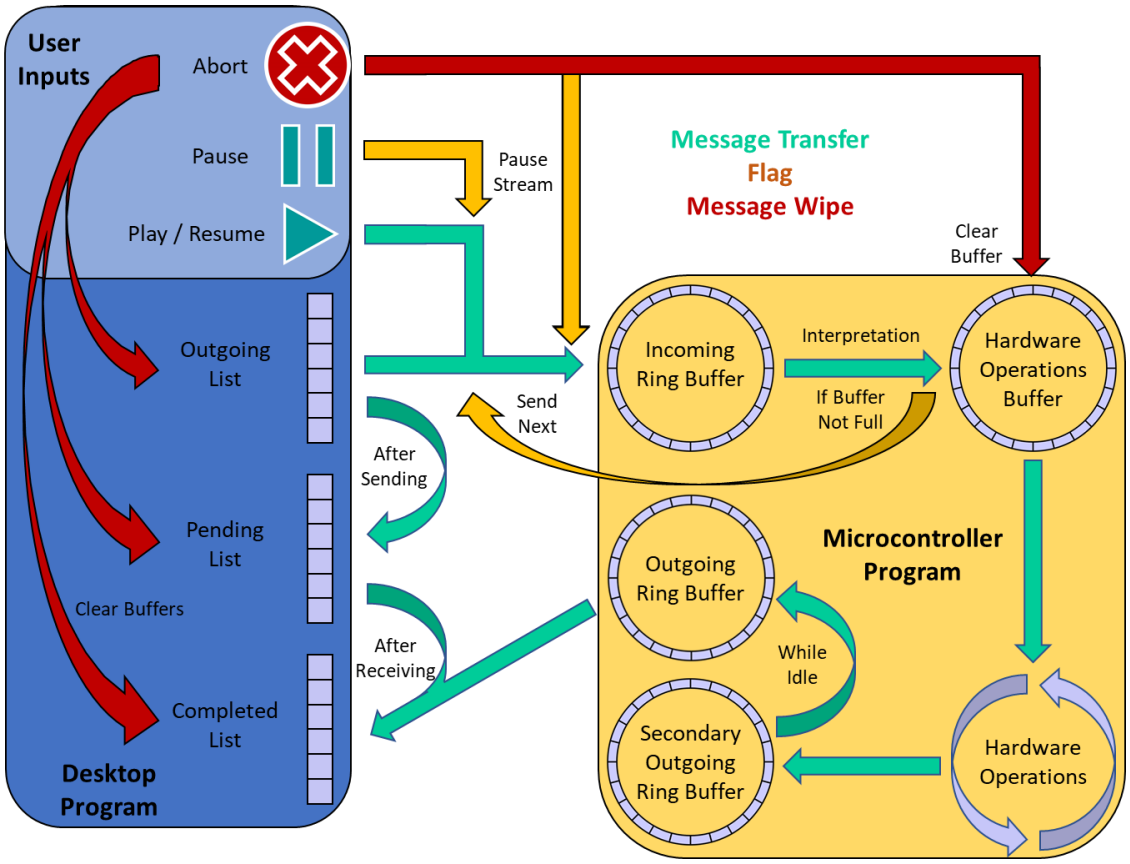

Figure 2.7 *Diagram of ModiPrint's serial communication protocol.*

2.3.1.8 Stepper Control Protocol

Stepper operation needs to be calculated and executed in real time as the microcontroller does not have the memory to store all Δt values. Preparations for each stepper movement also cannot be stored because of the same issue, but unlike the stepper control itself, the preparations can occur in a separate asynchronous operation which I will refer to as the prepper.

A major function of the prepper is to ensure that move multiple steppers simultaneously, which is required to drive the diagonal movements necessary for 3D printing. If the program is to feature the modularity of tunable max speed and acceleration parameters for each motor, then the program must normalize the velocity profile of each motor such that acceleration, cruise, and deceleration happens simultaneously without exceeding maximum speed and acceleration parameters. This creates diagonal movement between multiple stepper motors even though each motor has variable distances for movement.

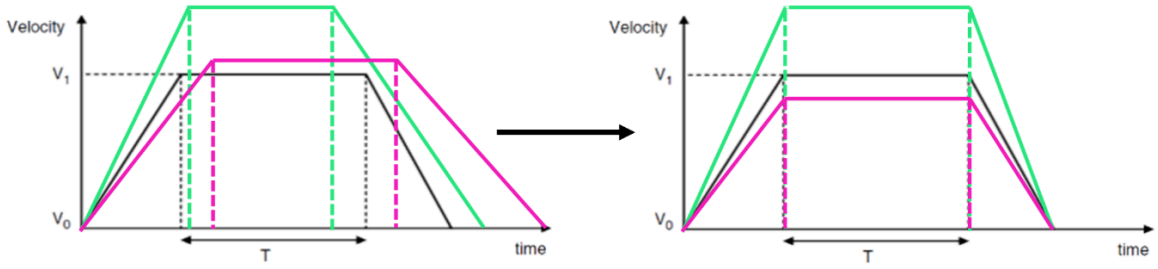

Figure 2.8 *Diagram depicting the normalization of stepper motor velocity profiles.*

Normalizing these velocity profiles and preparing for real time stepper movement requires the following steps:

1. Determine the stepper that will move the greatest number of steps (AKA leading stepper). The stepper control protocol will drive this stepper and all other steppers will follow this stepper in a manner determined by rasterization.
2. Determine speed and acceleration values of the entire movement and the leading stepper as limited by the slowest moving stepper.
3. Determine the velocity profile of the movement such that enough distance is allocated for full deceleration to the exit speed while maintaining the highest speeds possible.
4. Determine the initial values required to calculate Δt in real time.

These parameters are stored in a ring buffer which I will refer to as the movement buffer. The movement buffer is consumed by the stepper operation protocol. In between execution of individual steps, the prepper repeats its protocol and yields its priority if stepper operations so require. These normalization calculations must also be performed in the desktop program as the desktop program must calculate the parameter of junction speed and stream it to the microcontroller.

The stepper operation protocol operations with a repeating timer. This timer triggers the execution of the stepper operation protocol at the frequency specified by the Δt value. Therefore, the stepper operation protocol, while time sensitive, is not always in operation. The time Δt that is spent waiting for the next step is used to perform other operations, including use of the prepper for future movements. Each loop of the protocol consumes data from the prepper to perform the following:

1. Rasterizes multi-stepper movement via the Bresenham algorithm.
2. Checks is the stepper motor needs to step or if a corresponding limit switch is hit and accordingly sets the motor's corresponding step pin.
3. Set the second stepper operation protocol to fire. This secondary operation simply sets the state of the previously set step pin to low. This operation occurs at a time interval set by the user.
4. Calculate Δt for the next step.
5. Determine if the protocol needs to move to cruise or deceleration based on the velocity profile calculated in the prepper.
6. If a limit switch was hit, pause operations, and communicate the status to the desktop program.
7. Set this stepper operation to fire again after interval Δt.

2.3.1.9 G-code Conversion & Custom Programming Language

ModiPrint's desktop program facilitates the workflow from CAD models to machine execution by converting g-code to ModiPrint's specialized programming language. ModiPrint's desktop program uses print parameters as specified by the user and matches these parameters to sets of tool path g-code lines. On reading printing and moving g-code lines, ModiPrint's desktop program will directly convert these lines to its specialized language. After converting the entire file, ModiPrint's desktop program reads over all movement-based lines again to attach junction speed parameters. An overview of how g-code is converted to ModiPrint's specialized language is detailed in **Table 2.1**. A thorough documentation of how this language works, with examples, can be found in the documentation.

Table 2.1 *Conversion chart of g-code to ModiPrint's custom programming language.*

G-code	Conversion	ModiPrint's Language
	No conversion.	C00 # Check connection. Returns the # message.
T# Switch Tool Head	Switch printhead or change operations parameters. Converts a T g-code line to a set of C10 lines, a C11/12 line, and possibly a G00 lines if printheads need to be repositioned.	C10 X/Y/Z T# D# P# L# S# A#; Set axes parameters. Sets the GPIO pins, step pulse duration, speed and acceleration of the specified axis.
		C11 T# D# P# L# S# A# Set motor-driven printhead parameters. Sets the GPIO pins, step pulse duration, speed and acceleration of the motorized printhead.
		C12 V# Set valve-based printhead parameters. Contains the GPIO pin that drives the valve.
G00/G01 X# Y# Z# E# Movement (if no E parameter) or printing (if positive change in E). Contains the X, Y, and Z movement distances.	Movement and printing. During movement or extrusion printing, each G00/G01 g-code line is directly converted to a G00/G01/G02 line. During droplet printing, each G00/G01 g-code line is converted to alternating G00 and G11/G12 lines.	G00 X# Y# Z# T# Movement. Contains the X, Y, and Z movement distances with an exit speed.
		G01 E# X# Y# Z# T# Motor-driven printhead printing with movement. Contains the printhead, X, Y, and Z movement distances with an exit speed.
		G02 X# Y# Z# T# Valve-based printhead printing with movement. Contains the X, Y, and Z movement distances with an exit speed.
GX X# Y# Z# Printing with movement. Contains the X, Y, and Z movement distances.		G11 E# Motor-driven printhead printing without movement. Contains the printhead move distance.
		G12 O#/C Valve-based printhead operation without movement. Contains valve open time or specifies opening until commanded to close.
G90, G91, G92, M82, & M83 Use or set absolute or relative positions for following tool paths	No conversion.	

Table 2.1 details the part of the custom programming language used in print sequences and ModiPrint's workflow. However, manual user commands require additional lines detailed in **Table 2.3.** Not included in either table are the returns for error handling and specific returns associated with each of ModiPrint's lines in **Table 2.1**.

Table 2.2 *Additional commands and returns from ModiPrint's custom programming language.*

ModiPrint's Language	Action
*Center X# Y#	Calculates the midpoint for each axis requested. Outputs a command that moves all requested axes to and the midpoint plus a X and Y offset.
*OriginE/X/Y/Z	All participating axes now use this point as their origin (position = 0) and their max and min range values are recalibrated around this new origin.
*SetMinMaxPos EN/M# XN/M# YN/M# ZN/M#	Sets the current position of axes with the # value. Then sets as either the min (N) or max (M) position values to that # value. The distance between the minimum and maximum positions are maintained. If N or M is not specified, then set the position value only.
*Pause #	The desktop program will halt serial protocol (outgoing messages to the microcontroller and incoming messages from the microcontroller) will not execute for # milliseconds.
*SwitchMaterial "(Material Name)"	Expands to a series of commands to reposition printheads based on offsets then set new parameters for a new printhead and the XYZ stage.
*RetractZ	Moves the Z actuator back to the default position where the default position is 7.5 mm below the upper limit switch.
#	Pause all hardware operations at the earliest convenience.
%	Resume all hardware operations if previously paused.
&	Clear the hardware operations buffer.

Microcontroller Returns	Meaning
$	Ready to receive next message.
!LmtE/X/Y/Z(#,#,#,#)	Details the number of steps taken before hitting the limit switch.

2.3.1.10 Documentation

ModiPrint is thoroughly documented with the intent that users be able to easily assemble their own bioprinter and operate it to the fullest ability of its feature set. The documentation, which can be found at www.modiprint.com/documentation, contains:

1. Hardware assembly instructions with accompanying 3D models, wiring diagrams, and pneumatics diagrams.
2. Hardware modification guide.
3. Excel parts list calculator with pricing and links to all components.
4. Operations guide for ModiPrint's desktop program.
5. Guide on generating g-code tool paths for use with ModiPrint's desktop program.
6. Documentation of the machine code that is streamed to the microcontroller software.
7. Operations and parts selection guide for dispensing components.
8. Example protocol for achieving sterile prints.
9. Example protocol for fabricating the FRESH support bath.
10. Example protocols for calibration, characterizing resolution, optimizing print quality, and generating concentration gradients.

In total, the user guide consists of a 100 page+ manual with dozens of supplemental CAD, tool path, and other files.

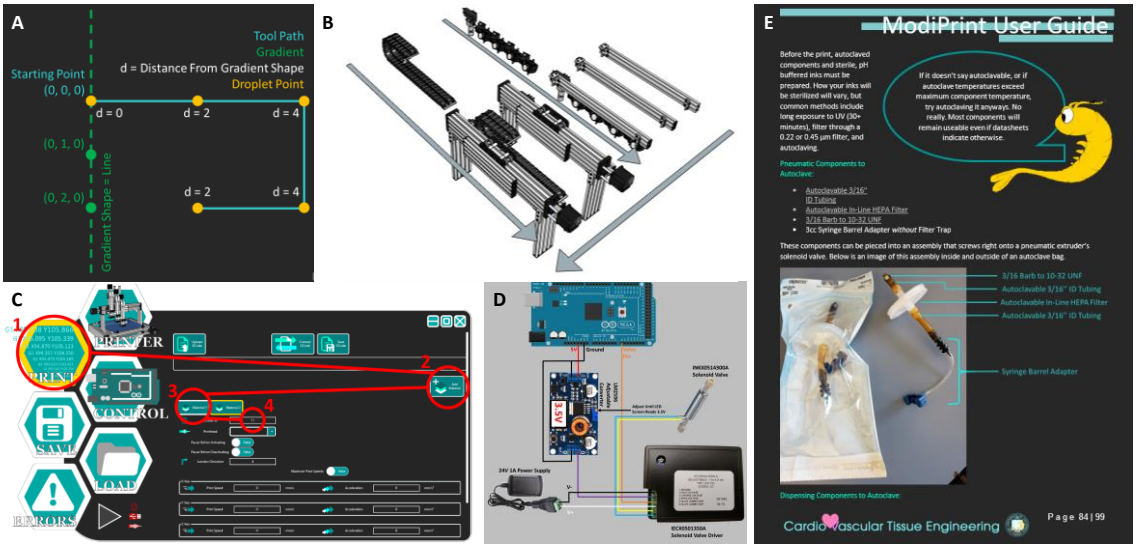

Figure 2.9 *Images from the ModiPrint user guide. A) Diagram detailing the effects of program parameters on droplet tool paths. B) Image of the interactive 3D model detailing the attachment of the drag chain and pneumatics to the X actuator. C) Representative image from the software operations section of the user guide. D) Wiring diagram for the microdispensing inkjet. E) A representative page of the user guide.*

2.3.1.11 Commercialization

Alongside fellow graduate student Rachel Hatano (who coined the name ModiPrint) and my PI Kara McCloskey, we acquired a $50,000 NSF I-Corps grant to conduct customer discovery for ModiPrint. With the help from our industry mentor, Elliot Botvinick, we interviewed over 100 members of the biotech industry. Interviewees included engineers, scientists, customer service personnel, lab directors, and CEOs representing small startups to large pharmaceutical corporations.

Our objective in these interviews was to determine pain points in operations of potential customers. To our surprise, despite the attrition rates of clinical trials, few interviewees in the pharmaceutical sector was using 3D tissue models to improve the pre-clinical screening process, let alone interested in bioprinting. There were adjacent needs that ModiPrint's technology could potentially pivot towards, such as the need for more easily programmed automation and more robust technology transfers to contract research organizations. But ModiPrint was not designed for these needs and adapting the technology may be too difficult. While the enterprise market was not a good fit, the few academic researchers we interviewed were excited by the idea of an affordable, multi-material bioprinter.

Therefore, ModiPrint was launched as an online business to service the academic market (www.modiprint.com). Leveraging the open source, DIY hardware design, ModiPrint runs on a partially open source model. Users are expected to acquire and recreate the system on their own and operate it with my open source desktop software and user guide, but they acquire the

proprietary firmware for a nominal cost. This perfectly suits the academic market which can absorb the extra needed assembly time with the excess manpower of students and acquire an affordable, highly customizable bioprinter that is suited to their specific research.

2.3.2 Stepper Control Optimizations for High Resolution Bioprinting

2.3.2.1 AccelStepper & Taylor Approximation

The first iteration of the microcontroller used an Arduino MEGA with embedded software that used the Arduino library [74] and AccelStepper library [75] and was programmed in C with the Arduino IDE. These libraries were initially chosen for their ease of use, as I was, at the time, not yet proficient in embedded programming. The Arduino library was necessary to establish a serial communication with the C#-based desktop program that processed g-code and streamed the custom programming language to the microcontroller. The C standard and Arduino libraries were used to parse then interpret the received messages. The AccelStepper library was necessary to execute these messages in the form of stepper motor movements.

However, it was soon apparent that AccelStepper had severe limitations for stepper control. The first limitation was its dependence on the Arduino library. The Arduino library automatically initializes unnecessary background processes which slow down the operations of AccelStepper. Furthermore, AccelStepper uses Arduino functions to control general purpose input output (GPIO) pin output which are orders of magnitude slower compared to the Atmega library or assembly code. In general, AccelStepper and the Arduino library sacrifices performance for ease-of-design which runs contrary to my design criteria. The result is that AccelStepper could not calculate Δt in a timely manner an inhibited the maximum speed of the stepper motors.

I attempted to decouple AccelStepper's stepper algorithm from the costly functions of the Arduino library. AccelStepper estimates Δt using an approximation of the Taylor Series, a method originally proposed by Embedded (**Equation 2.2**) [76].

$$\Delta t_{n+1} = \Delta t_n - \frac{2\Delta t_n}{4n+1} \quad (Equation\ 2.2)$$

Where n is the total step count.

A custom stepper control program was built around **Equation 2.2** using Atmel Studio and Atmega libraries as opposed to Arduino tools. **Equation 2.2** was originally intended to be used where Δt is a floating-point value. With floating-point values, the equation produces Δt values with almost no error compared to the ideal **Equation 2.1** (**Figure 2.10A**). Simulations within the stepper control software shows that it takes the Atmega2560 processor an average of 775 clock cycles to execute the equation. This equation would account for nearly half of the timer loop that executes stepper movement, where the rest of the execution takes on average 870 cycles.

The possibility of improving the equation's speed by using an integer data type for Δt was also explored as it reduces calculation times. An integer data type for Δt produces cumulative rounding errors with each iteration of the equation to where the Δt value becomes grossly inaccurate after a few dozen steps (**Figure 2.10A**). That inaccuracy results in a logarithmic velocity profile where

maximum speed is unideally limited by acceleration (**Figure 2.10B**). Therefore, an integer representation of Δt is inappropriate.

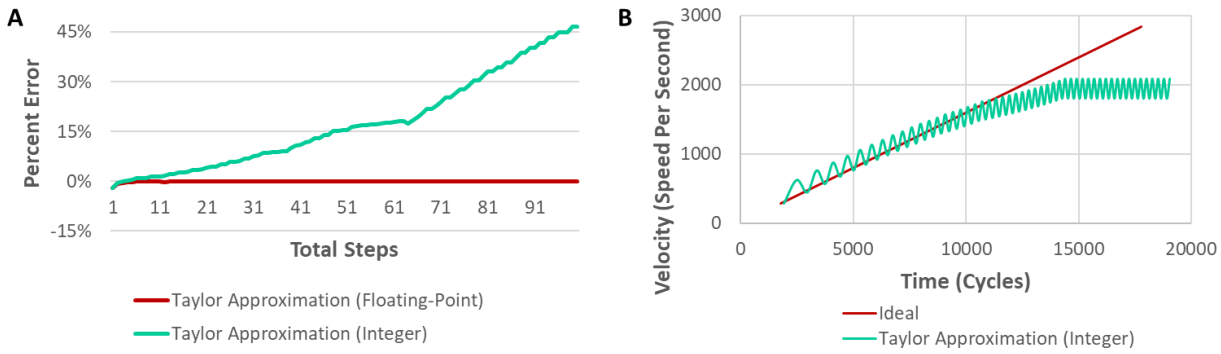

Figure 2.10 A) *Percentage error of the* ***Equation 2.2*** *compared to the Taylor approximation of* ***Equation 2.1*** *where Δt is typed as a floating-point or integer value at 40,000 steps/s*[3]*. When Δt is a floating-point value, the % error is within 2%. However, when Δt is an integer, the % error accumulates rapidly.* ***B)*** *Velocity profile of an ideal linear acceleration curve vs. that of the Taylor approximation of* ***Equation 2.2*** *using an integer value for Δt.*

The most glaring issue with **Equation 2.2** is its difficulty in utilizing a non-zero initial velocity (i.e. non-zero junction speeds). This stems from the fact that the Δt value at $n = 0$ is calculated via **Equation 2.3**.

$$\Delta t = 0.676 \frac{\sqrt{2a}}{a} \ (Equation\ 2.3)$$

Where a is the acceleration.

Equation 2.2 cannot be initialized at a value where $n > 0$. The workaround is to generate a lookup table where Δt is calculated for a variety of n values. However, as ModiPrint is made to be modular and support a range of speeds and accelerations which creates the challenge where the lookup tables are necessarily generated dynamically. Furthermore, there must be four lookup tables in total, one for each actuator of the XYZ stage, and one for a motor-driven printhead. This consumes a large amount of valuable memory which could instead be used to buffer against short movements.

While not impossible, the difficulty and compromises of integrating non-zero junction speeds with **Equation 2.2** makes it infeasible for the purposes of ModiPrint.

2.3.2.2 Modified GRBL

I also explored the prospect of modifying GRBL, an open source CNC control software made for the Arduino MEGA [77]. GRBL achieves a very high ~30,000 steps/s by altering the velocity profile into a piecewise function. GRBL calculates this by setting a time for each piecewise segment, the uses standard kinematics equations to calculate its Δt (**Figure 2.11**). This allows GRBL to still use costly operations but does not calculate step time for every step. Although acceleration is not as smooth, GRBL is validated by its use in thousands of CNC and 3D printing machines worldwide. More importantly, GRBL already implements non-zero junction speeds via **Equation 2.4** [78].

$$Junction\ Speed = \left| \frac{aJD \sin\left(\frac{\theta}{2}\right)}{1 - \sin\left(\frac{\theta}{2}\right)} \right| (Equation\ 2.4)$$

Where JD stands for junction deviation, a user defined parameter that ranges from 0 to 1. θ is the angle between movements.

While I did not modify GRBL to operate ModiPrint's programming language, I familiarized myself with GRBL's code and explored the prospect of a modified GRBL. Before attempting the daunting task of rewriting such a large codebase, I found several aspects of GRBL's design that was ill-suited to the intent of ModiPrint.

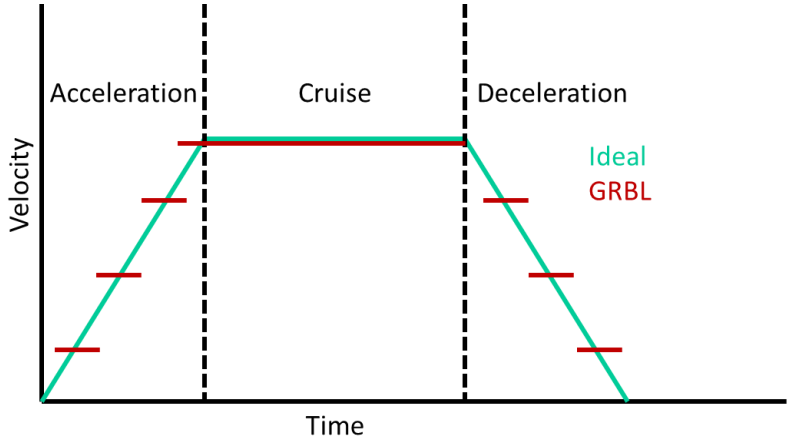

Figure 2.11 *Velocity profile of GRBL's velocity profile vs. an ideal linear acceleration velocity profile.*

GRBL may not produce smooth movements when printing the small line segments found in the tool paths of organically shaped models. This stems from the fact that the program calculates movement parameters in real time. Small line segments are executed by the hardware faster than GRBL can calculate new movements. Therefore, GRBL will stop, and in the case of pneumatically operated printing, excess material will be deposited. The issues of short movements can be

mitigated by buffering data, but GRBL can only buffer a few dozen microseconds of steps at most as it buffers the subdivisions of its piecewise acceleration [77,79]. A short buffer time means that idle time during longer movements cannot be used effectively to cover for short movements. Therefore, GRBL is not suited to print the organic shapes that would be found in many of the organically shaped objects a bioprinter would be required to produce.

Furthermore, GRBL has limited functionality when calculating junction speeds. GRBL's issue lies in the fact that GRBL only sees a limited number of movements ahead. Junction speed cannot be higher than the required speed needed to slow down to zero after a print's end. In very short movements (the kind of movements where excess material deposition in junctions is most prominent), GRBL must assume that the last known movement is zero velocity and throttles junction speed to leave enough "runway" for deceleration. Although this case is rare, it is a limitation for GRBL in junction speed calculations and its capability for fast junctions as stated in GRBL's source code comments [77].

Another limitation of GRBL is that way junction speed calculations are handled. Standard g-code does have a way to stream junction speed parameters and necessarily forces the microcontroller to perform such calculations [80]. GRBL must constantly recalculate junction speed parameters as its "runway" for deceleration increases. During a series of short movements, this aspect of the program can be overloaded, causing stalls and more excess material deposition.

These issues can possibly be alleviated by a rewrite of GRBL's structure. However, I was hesitant to invest the time into rewriting such a large, unportable codebase. After exploring these options, I decided to create my own stepper control protocol.

2.3.2.3 Novel Stepper Control Equation

My own stepper control program used my own novel approximation of linear acceleration. **Equation 2.5** approximates velocity based on the total time spent in the movement then calculates the next step time based on that velocity value.

$$\Delta t_{n+1} = \frac{1}{\sum_0^n a\Delta t_n} \quad (Equation\ 2.5)$$

Where a is acceleration, n is total steps taken.

Compared with the that Taylor Approximation (**Equation 2.2**), **Equation 2.5** is slightly faster at an average execution time of 691 clock cycles. More importantly, this equation easily supports non-zero junction velocities by initializing with **Equation 2.3.**

$$a\Delta t_0 = \frac{{v_0}^2/a + 2}{\sqrt{{v_0}^2 + 2a}} \ (Equation\ 2.6)$$

Where v_0 is the junction speed, and a is acceleration.

Like GRBL, v_0 is calculated via **Equation 2.7.** Unlike GRBL, **Equation 2.5** can be calculated and consumed at every step cycle and does not need to be buffered. As a result, entire linear movements can be buffered instead of individual Δt values. This longer buffering means the protocol is much more immune to stalling from shorter movements.

Furthermore, ModiPrint's special protocol calculates junction speed with the desktop program and streams the junction speed value as a parameter in a movement message. Unlike GRBL, the junction speed calculation is offloaded to a personal computer which has virtually unlimited RAM in this context, the look-ahead of junction speed calculations does not throttle the junction speed results. Because junction speed is not calculated on the microcontroller, there is also less risk of stalling from successive short movements.

I compared my approximation to a perfect velocity profile (**Equation 2.1**) in **Figure 2.3**. Beyond the second step, the percent error remains less than 1%. The more significant errors from the first two steps is not enough to distort stepper operations in practice. The protocol also achieves an acceptable 10,000 steps/s maximum speed, plenty for the purposes of ModiPrint's screw-driven actuators.

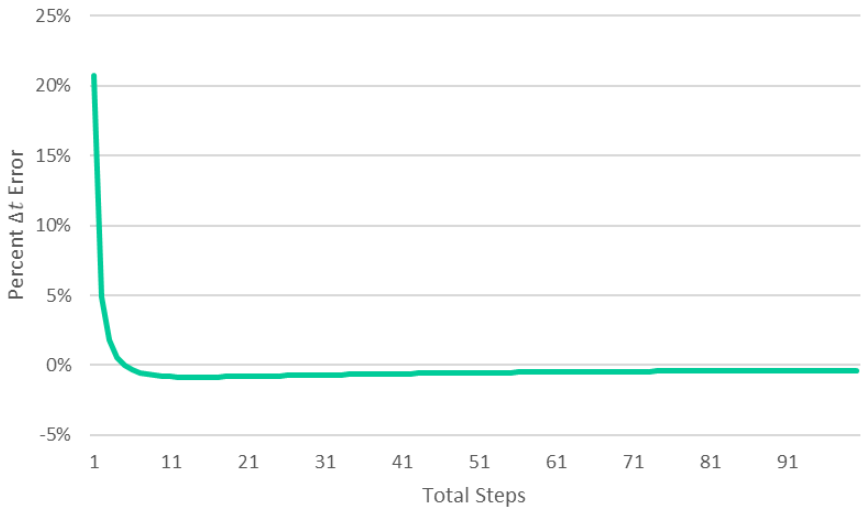

Figure 2.12 *Percentage error of the* Δt *result from* ***Equation 2.5*** *compared to result from* ***Equation 2.1*** *at 40,000 steps/s*[3]. *The 1st step has an error of 21%. The 2nd step has an error of 7.9%. Beyond the 2nd step, the percent error is below 1%.*

ModiPrint's stepper algorithm does have a minor disadvantage in deceleration. Deceleration follows the same equation as acceleration but incurs additional error that causes velocity to be slightly greater than intended. In practice, this makes no discernable difference in stepper operations.

As **Table 2.3** demonstrates, ModiPrint's program improves upon the alternatives except for GRBL's maximum speed. However, 10,000 steps/s is adequate for ModiPrint's hardware's screw-driven actuators, and in practice, does not limit operation speed.

Table 2.3 *Comparison of the different* Δt *equations and their effects on stepper motor control.*

	Ideal	Taylor Approximation	GRBL	ModiPrint
Δt Calculation	$\Delta t = \sqrt{\frac{2n}{a}} - \sqrt{\frac{2(n-1)}{a}}$	$\Delta t_{n+1} = \Delta t_n - \frac{2\Delta t_n}{4n+1}$	Piecewise	$\Delta t_{n+1} = \frac{1}{\sum_0^n a\Delta t_n}$
Initialization	Same as Δt Calculation	$\Delta t = 0.676\frac{\sqrt{2a}}{a}$	Same as Δt Calculation	$a\Delta t_0 = \frac{{v_0}^2/a + 2}{\sqrt{{v_0}^2 + 2a}}$
Calculation Speed (Clock Cycles)	1444	775	N/A	691
Maximum Speed	Slowest	~9,000 Steps/s	~30,000 Steps/s	~10,000 Steps/s
Velocity Profile	Linear Acceleration	Virtually Linear Acceleration	Piecewise Linear Acceleration	Virtually Linear Acceleration
Buffering	N/A	90 Movements	• 6 Δt Segments • 16-18 Movements	90 Movements
Junction Deviation	N/A	Difficult to Support	• 16-18 Movements • Calculated in microcontroller	• Unlimited Look-Ahead • Streamed

2.3.3 High Resolution Bioprinting

High resolution printing was originally optimized using 2% w/v alginate hydrogel printed from the pneumatic extruder. To improve resolutions, I also tested a freeform reversible embedding of suspended hydrogels, called FRESH hydrogel slushie [17]. FRESH is a support bath of gelatin particles that suspends fluids in 3D space as they crosslink. This partially prevents materials from "sagging" due to gravity, thereby decreasing XY resolution. FRESH also enables us to use alginate without the addition of unwieldly hydrogels, such as gelatin [81], which would otherwise be required to maintain structural integrity. In addition, I altered the FRESH protocol to produce more consistent filament diameters (**Figure 2.13**).

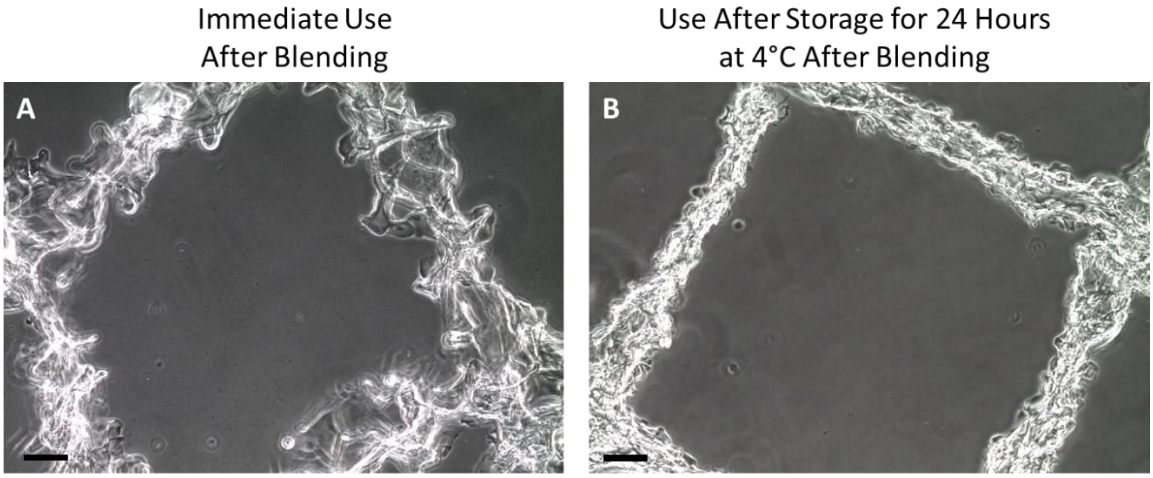

Figure 2.13 *Images of alginate filament quality with different FRESH preparation methods. A) Images of printed alginate filament quality immediately after the blending and washing step of the FRESH bath. B) Images of printed alginate filament quality after the FRESH bath has been stored at 4°C for 24 hours after blending. These filaments are more consistent in quality compared to those printed immediately after blending. Scale bars = 100 μm*

With FRESH and alginate, I used a 100 μm inner diameter nozzle, typically smaller than most other bioprinting studies. I characterized individual filament diameters by printing square grid patterns with a 0.5 mm pitch (**Figure 2.14**). This pattern was written by hand with ModiPrint's custom language and printing is completely automated by the device for repeatability. I found 500 μm pitches to be ideal for characterizing resolution as wider pitches created a structurally unsound sheet, but narrower pitches introduced too many overlapping paths that warped resolution. I iteratively improved resolutions by decreasing the print pressure to 5 psi and increasing print speeds to 12 mm/s which produced a mean filament diameter of 103 μm with a standard deviation of 19 μm (**Figure 2.14D**). Similar resolutions were maintained with additional hiPSC introduced into the ink (**Figure 2.14C**).

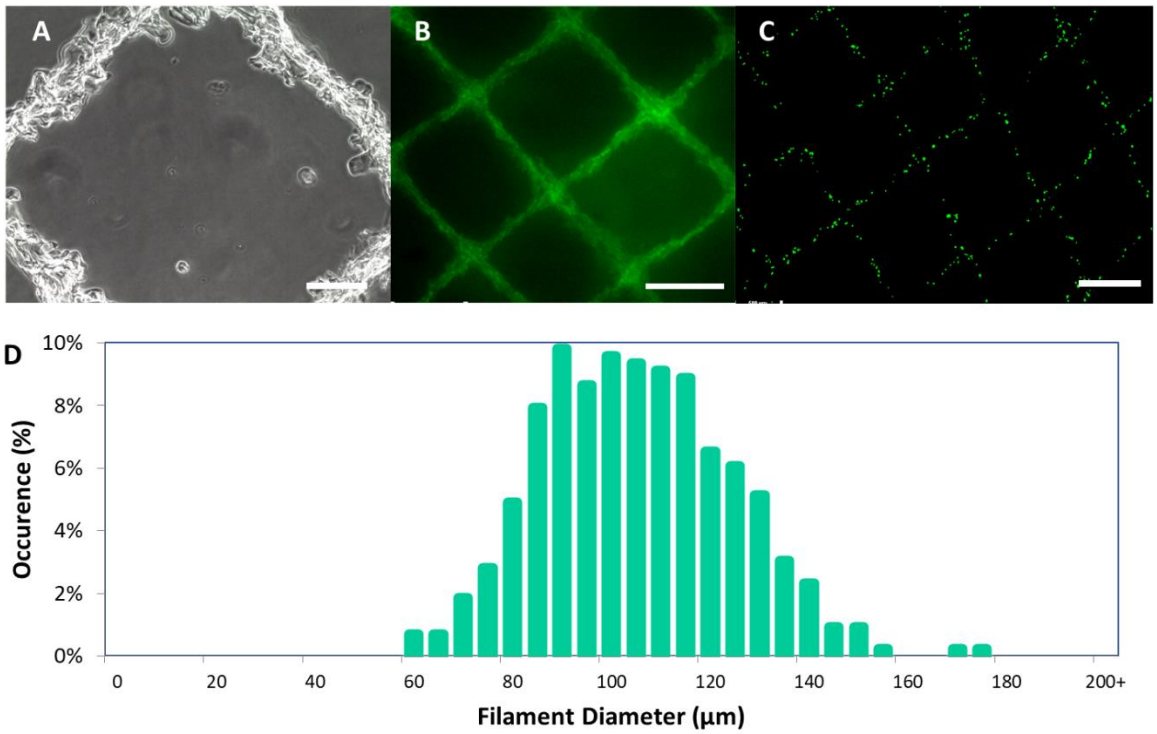

Figure 2.14 *ModiPrint can extrude high resolution, 100 µm alginate filaments A) Phase contrast image of printed alginate filaments, scale bar = 100 µm. B) Fluorescent image of printed alginate filaments mixed with FITC, scale bar = 500 µm. C) Fluorescent image of alginate filaments printed with CellTracker Green-labeled hiPSC, scale bar = 500 µm. D) A histogram of the distribution of alginate filament diameters, mean is 102 µm and standard deviation is 19 µm.*

I initially observed that resolution in constructs of complex geometries generated from extrusion were not as high as straight-line resolutions. The curves of organ-like shapes necessitate many line segments which forces the XYZ stage to slow down below its intended print speed while pneumatically driven printheads maintain the same dispense rates via a constant pressure acting on the reservoir. During this slow down, excess material is deposited during the transition between line segments. While other bioprinting studies have used a similar, pressure-driven extrusion method, only one other study to my knowledge has reported the same issue [61]. This is perhaps because few studies print at high resolutions with complex geometries where this issue is most exacerbated.

I sought to improve resolutions around corners by a combination of hardware and software optimizations. High torque motors enable high XY accelerations, resulting in less time spent at slower speeds transitioning between linear movements. The stiff frame and implementation of a simple cornering algorithm [78] (**Equation 2.4**) enables the maintenance of higher speeds around corners. Furthermore, the print surface was decoupled from the movements of the device, where only the machine is subject to jerky movements. The net result is that ModiPrint's XYZ stage maintains high speeds around corners for improved resolutions.

Corner resolution was characterized by printing with the pneumatic extruder through a 90-degree toolpath using the same alginate material and print parameters that generated 100 μm diameter filaments. These 90-degree angles were isolated with a custom print pattern made for this experiment. I measured the length of the angle's diagonal from the inner to the outer corner. In an ideal situation where there is no excess material deposited, the length of the diagonal would be a factor of square root of 2 larger than the straight-line diameter. Therefore, the ideal length of a 90-degree diagonal from my 103μm diameter filament is 145 μm.

Cornering speed is dependent on a parameter called junction deviation (JD), where 0 JD results in a full stop between linear movements and 1 JD results in no deceleration (**Equation 2.4**). A high acceleration of 2,000 mm/s^2 and a JD of 0.01 resulted in a diagonal length of 204 μm (**Figure 2.15A**) which is 40% larger than the ideal length. Removing the fast cornering feature by setting a JD of 0 resulted in a significantly ($p < 0.001$) larger diagonal length of 257μm. Decreasing the acceleration to 400 mm/s^2 further increased the diagonal length to 326 μm ($p < 0.0001$). Therefore, as cornering speeds and acceleration increases, unwanted deposition of excess material and the distortion of the intended print geometry is mitigated (**Figure 2.15A-D** and **Figure 2.15I**).

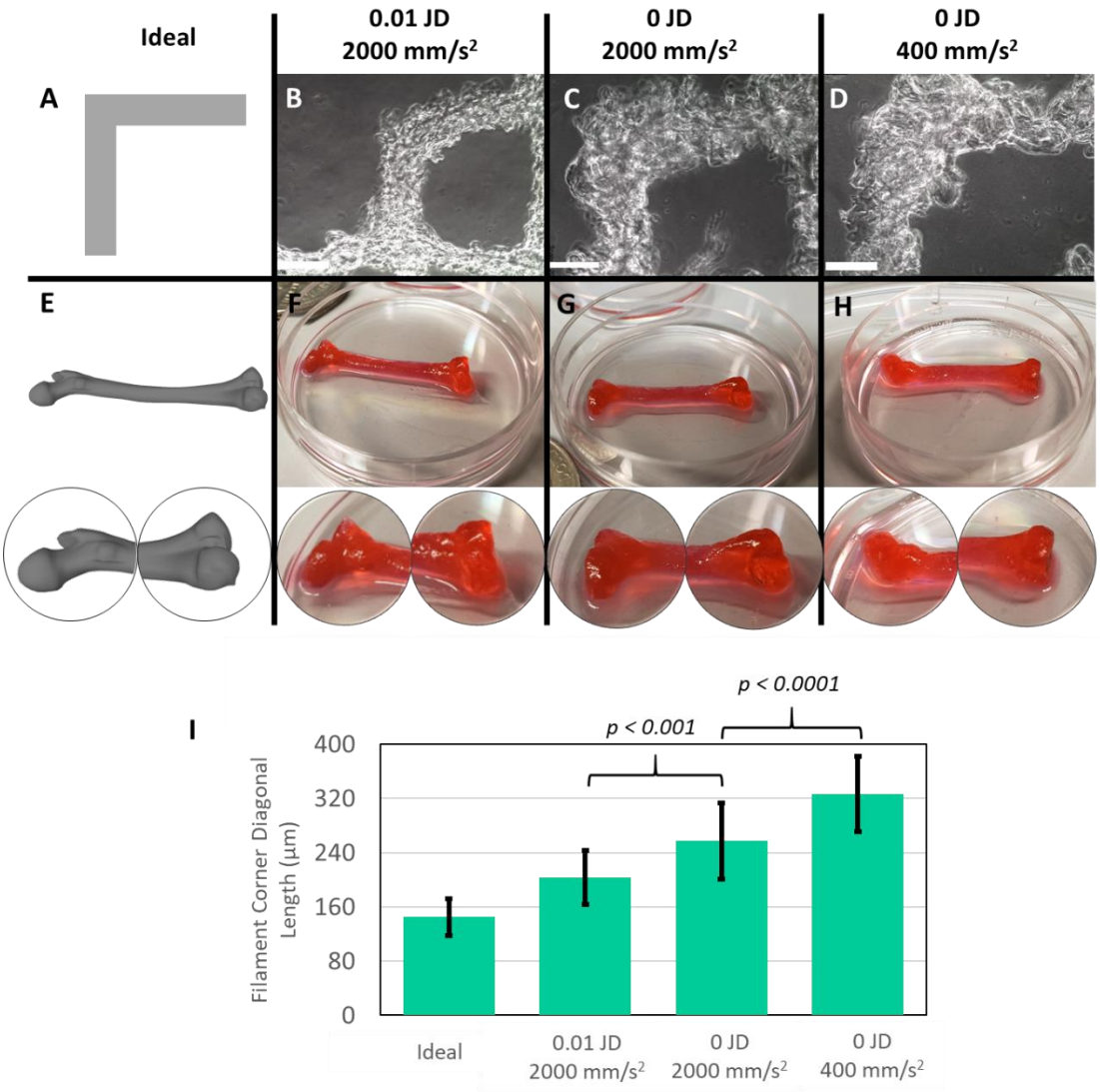

Figure 2.15 *Alginate filament resolutions during the extrusion of corners is affected by cornering speed and acceleration. A) A representation of a theoretically perfect 90-degree extrusion. B-D) Phase contrast images of 90-degree alginate filaments at various junction deviation and acceleration settings. E) A 3D model of a femur. F-H) 25 mm length alginate prints of the femur in Fig. 3F with various junction deviation and acceleration settings. For scale, all petri dishes are 35 mm in diameter. Scale bars in C-D are 200 µm. I) A bar graph of the width of the diagonal of a 90-degree alginate filament vs. various junction deviation and acceleration settings. The black bar represents the standard deviation. Here, ideal is a theoretically perfect corner.*

To demonstrate how suboptimal cornering speeds and excess material deposition can compound throughout complex prints, I printed very small, 25 mm length femur shapes with a rectilinear fill pattern and 100% infill (**Figure 2.15E-H**). Compared to the intended design of the CAD model, the high-resolution conditions of 2,000 mm/s^2 and 0.01 JD retains the fine details of the femur

shape. The same acceleration with a 0 JD loses these fine details. And a lower acceleration of 400 mm/s^2 with 0 JD mutilates any details of the object, demonstrating that a significant amount of excess material is still deposited during the transition between linear movements. Hardware that enables high acceleration and software that enables fast cornering mitigates the effects of this excess material deposition. This technique, along with FRESH hydrogel and optimized print parameters of low pressures, high print speeds, and small nozzle diameters can improve resolution in bioprinting.

2.3.4 Viable Printing of hiPSC

While bioprinting with hiPSC aligns with regenerative medicine's vision of engineered, autologous tissue [82], few published studies have demonstrated viable printing of fragile hiPSCs. To demonstrate that my extrusion techniques are gentle under high resolution conditions, I dispensed human induced pluripotent stem cells (hiPSC), which are notoriously fragile under shear stresses [35,36].

Although I initially struggled with sterility even though the entire set up was exposed to 30 minutes of UV before operating within a laminar flow biosafety cabinet, autoclaving all dispensing components and introducing a HEPA filter upstream of material reservoir fixed the issue. I also found that normal alginate was not suitable for maintaining viable hiPSC (data not shown) and I transitioned to 2% w/v RGD-linked alginate for my viability study. As this material was less viscous, I printed at a lower pressure of 3 psi and higher speeds of 25 mm/s to maintain similar filament diameters. The cells were printed in 10 x 10 mm square sheets with single filament thickness. It is worth noting that printing at high resolutions had the added benefit of reducing overall material usage such that a mere 100 µL of bioink produced four 10 x 10 mm sheets.

The printed hiPSC embedded in RGD-linked alginate remained viable and highly proliferative up to confluent-like conditions at day 30 (**Figure 2.16**). Although printed as single cells, by day 7 of culture within the RGD-linked alginate, the printed hiPSC grew in dense cell clumps, much like the colony formation of embryoid bodies. Cell viability was also quantified by LIVE/DEAD stained cells using flow cytometry. After 24 hours, the mean viability was 69% with a standard deviation of 13% (**Figure 2.16H**). Across the three replicates that were analyzed, the highest viability was 81%, and the lowest was 51%. After 7 days, the cells appeared to rebound with a greater viability of 86%. However, after 30 days, the viability dropped to 48%. I speculate that rapid cell proliferation accounted for the high viability at day 7 and that high confluence and excessive nutrient consumption accounted for the lower viability at day 30.

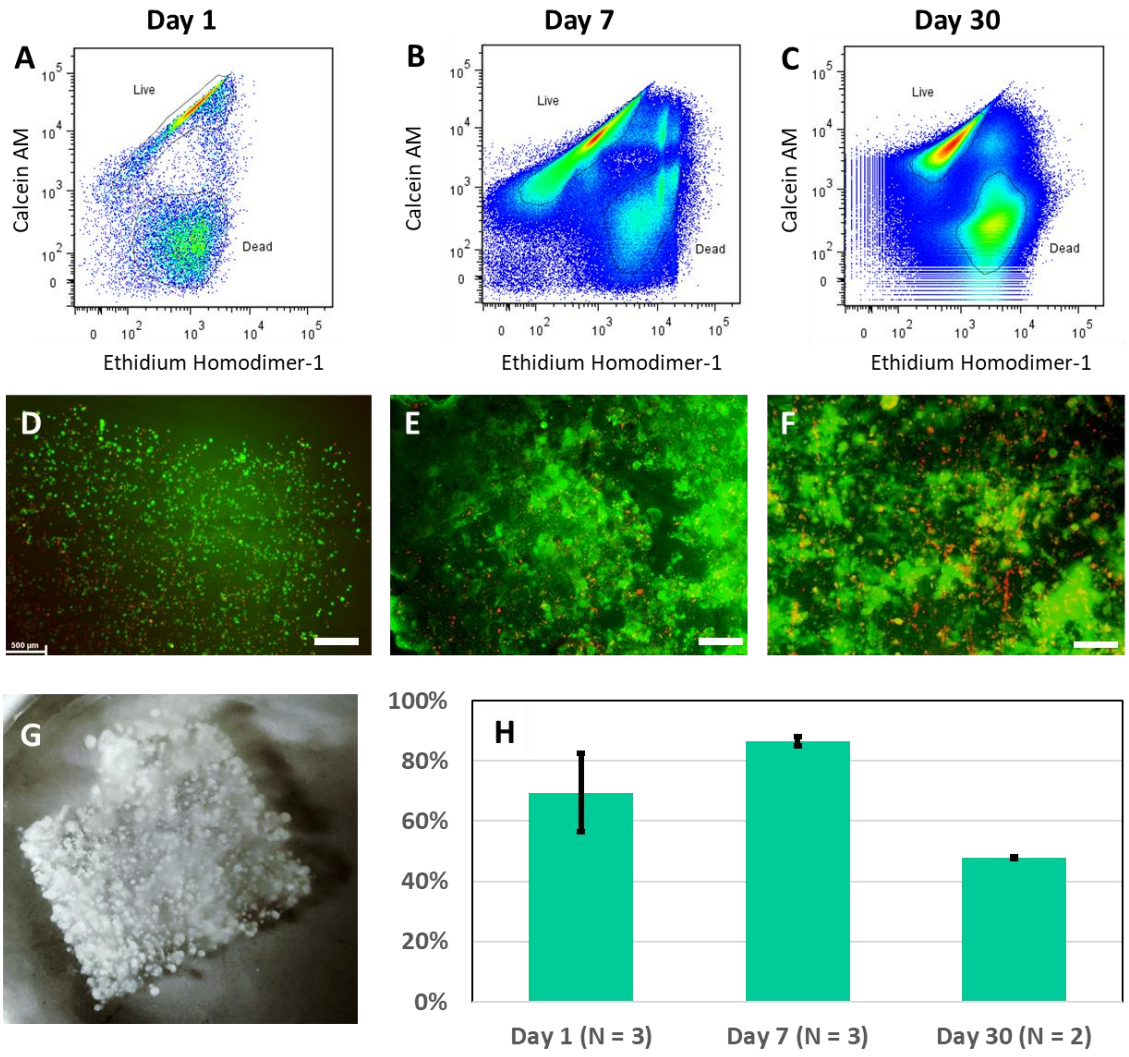

Figure 2.16 *Viability of hiPSC printed with ModiPrint in RGD-linked alginate over time. A-C) Flow cytometry scatter plots of the hiPSC LIVE/DEAD assay at Days 1, 7, and 30, respectively. D-F) Fluorescent images of the hiPSC stained with LIVE/DEAD. Scale bars = 500 μm. G) Image of the printed hiPSC embedded within RGD-linked alginate after 30 days with visible hiPSC colonies. H) Bar graph of hiPSC viability as determined by calcein AM staining and ethidium homodimer-1 resistance under flow cytometry. The black bar represents standard deviation.*

2.3.5 Fabrication of 3D Structures with Embedded Concentration Gradients

Concentration gradients play an important role in the cell's microenvironment by directing various cell fates and functions. These gradients have been mimicked in a variety of microfluidic devices and some 3D printing studies. However, artificially generating these gradients requires systems that expose cells to multiple channels of media, serial dilution devices [32], or the patterning of multiple materials of different concentrations [19]. These techniques are complex with limited choice of geometries of the gradients and the containing structures. Therefore, we aimed to leverage the

flexibility and CAD integration advantages of bioprinting to incorporate concentration gradients into the cell-material prints by the combination of extrusion bioprinting, drop-on-demand bioprinting, custom software, and the FRESH support bath. This flexible and automatable technique can generate 3D gradients of arbitrary geometry contained within 3D hydrogels of the either the same or distinct arbitrary geometry.

This is accomplished using ModiPrint's custom program which automatically integrates the concentration gradient with the toolpath specified by g-code input (Fig. 5). The system controls the deposition volume of a small molecule solution droplet by varying the valve dispense time of the microdispensing inkjet. This valve dispense time is determined by a function of distance from user defined geometries and a gradient strength parameter settable within ModiPrint's software (Equations 1 & 2). Then the microdispensing inkjet patterns a microdot array of the small molecules which is suspended in 3D space by the FRESH support bath. The movement of the nozzles create temporary gaps in the support bath which spreads the small molecules along the toolpath. The pneumatic extruder dispenses and mixes hydrogel with the suspended small molecules. As the alginate quickly crosslinks, the small molecules are entrapped within the material. Lastly, the support bath is removed, leaving a hydrogel construct embedded with a concentration gradient of small molecules.

$$Valve\ Open\ Time_d = Valve\ Open\ Time_0 * (1 + Linear\ Gradient\ Strength * d) \quad \text{(Equation 2.7)}$$

$$Valve\ Open\ Time_d = Valve\ Open\ Time_0 * (1 + Exponential\ Gradient\ Strength)^d \quad \text{(Equation 2.8)}$$

To visually demonstrate the results of this technique, I entrapped blue food coloring within 2% alginate, creating gradients of different shapes and sizes, located within different hydrogel geometries (Fig. 5B-D), including a cylinder (Fig 5D). To show that the cylinder remained hollow, red food coloring was perfused through the inner channel with a syringe.

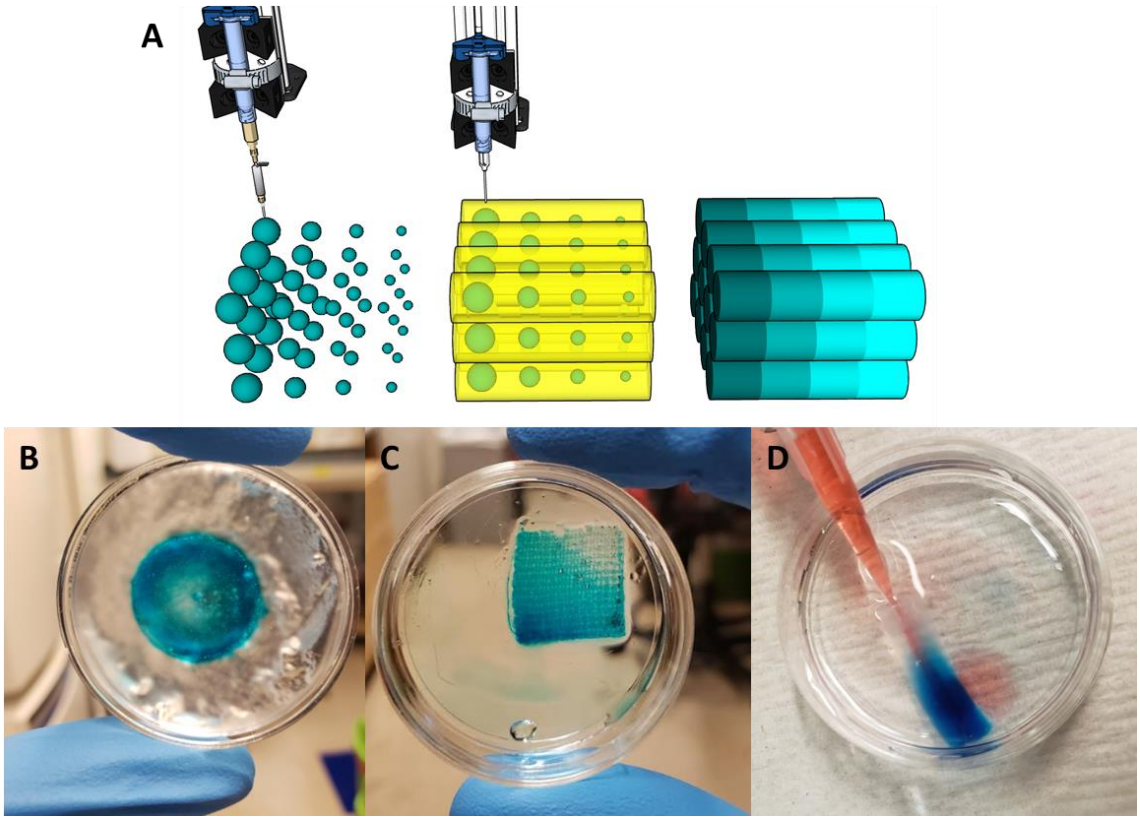

Figure 2.17 *Hydrogels embedded with concentration gradients are generated by A) Schematic representation of ModiPrint's process of generating concentration gradients embedded within hydrogels. ModiPrint's microdispensing inkjet produced droplets of varying sizes suspended within the FRESH support bath. Then, the pneumatic extruder prints and mixes hydrogels over the droplets. Crosslinking of the hydrogels entraps the droplets within. B) Blue food coloring is suspended within the FRESH support bath in a radial geometry with a radial gradient. C) Blue food coloring is entrapped in a radial gradient within an alginate hydrogel printed in a grid pattern. D) Blue food coloring is entrapped in a linear gradient within an alginate hydrogel printed in a cylindrical geometry with 4 mm outer diameter and 1 mm inner diameter. Red food coloring is perfused through the hollow, inner diameter of the cylinder via a syringe. For scale, all petri dishes 35 mm in diameter.*

Although, this bioprinting system can produce hydrogels of arbitrary geometries embedded with small molecule gradients, further work (Chapter 5) shows that gradients can be retained for a reasonable length of time. Other studies also indicate that these gradients direct cell function including using the entrapment of small molecules in its potential in drug delivery [83]. Release timing can be further controlled by altering alginate concentration or modifying the alginate with another hydrogel [84], Various extracellular matrix proteins can also be added or substituted to manipulate the bioactivity of small molecule gradients [85].

2.4 Conclusion

ModiPrint is an accessible, affordable, feature-rich bioprinter. For less than $4,000 in hardware, a user can assemble their own, modular, multi-material device, ModiPrint. ModiPrint is capable of high-resolution extrusion bioprinting of hiPSC. It also performs a novel technique to generate concentration gradients of small molecules embedded within hydrogels. It integrates these features with full support for g-code and other open source slicing tools. This is achieved via custom programming and novel hardware designs. Few other bioprinters has this wide range of features with such a low price, let alone, novel features that improve microscale complexity.

Chapter 3: Generation of Smooth Muscle Cells from Pluripotent Stem Cells

Abstract

Mural cells are indispensable for the development and maintenance of healthy mature vasculature and are valuable in the context of regenerative medicine for cell therapies and as developmental models. However, their functional plasticity, developmental diversity, and multitude of differentiation pathways complicate in vitro generation. Here, I optimize for the generation of vascular smooth muscle cells (VSMC) from pluripotent stem cells (PSC) by studying the effects of soluble signals, extracellular matrix, and induction time on cell fate efficiency. I briefly explored using mouse embryonic stem cells (mESC) using serum and trans retinoic acid (atRA) as well as a multi-stage, serum induction for human induced PSC (hiPSC). While the generation of a vascular progenitor cells from hiPSC was very successful, issues with commercially available VSMC marker antibodies impeded significant progress towards VSMCs. However, the limited data that was produced indicated that the hiPSC-derived population was a VSMC population that exhibited characteristic markers and vasculogenesis functions.

3.1 Introduction

3.1.1 Pluripotent Stem Cell-Derived Vascular Smooth Muscle Cells

The mural cell is a unique histological category encompassing pericytes (PC) and their developmentally related vascular smooth muscle cells (VSMC). These cells ensheath the inner endothelium of blood vessels where, typically, small diameter vessels are assigned a sparse population of PC while large vessels consist of multiple VSMC layers [86]. Mural cells provide our circulatory system with stability and contractile function. Without mural cells, organisms would not survive until birth due to hemorrhagic, permeable, and short-lived blood vessels [87]. While vessel stabilization is the mural cell's best known role, VSMC and the multipotent PC are also known for their significant contributions in developing vascular disease, promoting immune response, and remodeling the surrounding extracellular matrix (ECM) [88–90].

Due to their functional diversity, mural cells are important cells in several diseases and therapeutic applications. In vascular therapies, implanted mural cells can be used to enhance nascent vasculature for the repair of damaged, ischemic tissues [91]. For cellularized vascular grafts, the added smooth muscle layers can provide structure, contractility, and improved recovery [92]. Moreover, the phenotypic modulation of VSMC is often studied for its implications and potential therapies in vascular disease [90]. Mural cells are also being targeted to control the degree of vascularization in tumors [93].

Pluripotent stem cells (PSC) can provide an alternate approach to the application and study of VSMC. An often-limiting factor of cell therapies is the lack of a suitable cell source, but unlike many terminally differentiated adult cells, PSC are renewable and can be guided to differentiate into any cell lineage in the body. Moreover, these PSC-derived cells are less senescent and can be superior at promoting regeneration than their in vivo counterparts [94]. With the discovery of induced PSC, PSC can now be derived from otherwise terminally differentiated adult cells [5]. Furthermore, PSC can be used as in vitro models of development. By reverse engineering the natural embryonic microenvironment, developmental pathways can be isolated from an otherwise complex system. Interestingly, many VSMC developmental pathways overlap with phenotypic modulation pathways, allowing for implications in vascular disease [90].

However, generating PSC-derived VSMC is complicated by several factors including: 1) the multiple origins of VSMC – with correspondingly distinct functions - provide confounding development paths, 2) a wide range of microenvironment factors that can contribute to the development of VSMC with different combinations of factors yielding different resulting cells, and 3) a lack of lineage-specific surface marker sets for VSMC.

3.1.2 The Origin of Vascular Smooth Muscle in Embryonic Development

As with all cells of the body, VSMC arise from the developing embryo where they must navigate a labyrinth of developmental paths before reaching their destination. These paths must be replicated in the generation of VSMC from PSC. However, our understanding of these paths is complicated by the multiple embryonic origins of VSMC wherein fate decisions are tied to the cells' ultimate anatomic location and function.

The corresponding in vitro and in vivo development of VSMC begin with the embryoblast, an inner cell mass from which embryonic stem cells (ESC) are isolated. The embryoblast reorganizes into

an epiblast which derives the primitive streak (PS), a ridge-like formation that divides the organism bilaterally. Mesendoderm cells of the epiblast migrate through the anterior PS and replace hypoblast cells at the bottom of the developing embryo, forming the definitive endoderm. Migratory mesendoderm at the anterior PS also occupy between the epiblast and definitive endoderm to form the mesoderm. The remaining, non-migratory epiblast cells default to the final germ layer, the ectoderm [95]. This process by which the epiblast gives rise to the three distinct germ layers is known as gastrulation [96]. Of these three germ layers, VSMC are produced from specific regions within both the mesoderm and the ectoderm [97].

The mesoderm spreads laterally across the embryo outward from the PS into the axial, paraxial (PM), intermediate, and lateral plate mesoderm (LPM) regions. The mesoderm regions are specified by a bone morphogenetic protein (BMP)-4 gradient, which is most concentrated at the LPM [98]. As the organism matures, the PM forms into blocks of somite cells that line the embryo bilaterally and develop into bone, skeletal and smooth muscle as well as various mesenchymal tissues. Meanwhile, the LPM further segregates into the cardiac mesoderm (CM), from which most heart tissue is derived, and the hematopoietic mesoderm, which gives rise to most of the vasculature. Within the LPM is a specific subset of cells that express CD309, an iconic marker for vascular progenitors that derives both endothelial cells (EC) and VSMC in vitro [51]. Within the CM, the low concentration end of a bone morphogenetic protein-2 (BMP-2) gradient forms the proepicardium, a mesothelial lining in the heart. The concentrated side of the BMP-2 gradient transforms into the collective of cardiac and smooth muscle progenitors known as the secondary heart field [99]. All the while the ectoderm layer initially forms two regions, the neural region and the non-neural region. Cells from the neural plate of the neural region delaminate from the neural tube and form a third region: the neural crest (NC) [100]. A BMP-2 gradient specifies these three regions with the lowest concentration at the neural plate and the highest at the non-neural regions [101]. The neural crest, often called the fourth germ layer for its broad multipotential, goes on to generate a wide variety of cell types including VSMC.

Summarized in **Figure 3.1,** the in vivo specification of these developmental regions is largely controlled by BMP, Wnt, and fibroblast growth factors (FGF), as well as transforming growth factors (TGF) that activate Activin- and Nodal-related signaling pathways. These signals often form gradients which diffuse across the developing embryo [98,99,101]. Therefore, many in vitro models reflect these in vivo studies by activating the same major signaling pathways and even mimicking ligand concentrations [12]. Because PSC tend to differentiate spontaneously and randomly, these in vitro models aimed towards lineage specification are often supplemented with inhibitors to derive pure populations of the desired cells. Of note, cell fate pathways may differ between PSC types even under the same differentiation conditions as demonstrated by in vitro specifications between human and mouse ESC [102].

Many embryonic populations are actually heterogeneous sets of precursors. For example, the LPM includes a variety of cardiac and hemopoetic progenitors with different multipotential [103]. As a result, some protocols derive embryonic progenitors into these more specific subtypes. For example, PSC differentiation protocols have produced more specialized sub regions of germ layers, such as the well-studied neuroectoderm [104]. Furthermore, in vivo progenitors do not arise directly from PSC, but rather mature through many branches of a progenitor tree. As such, some protocols aim for faithful recapitulation as exampled the step-wise generation of the mesendoderm, the in vitro

analog to the primitive streak [102]. Thus far, chemically-defined derivation protocols exist for the generation of not only all three germ layers but a variety of more specific embryonic intermediates.

VSMC arise from several embryonic sites including: the NC of the ectoderm, the LPM, and the somites of the PM. In general, VSMC located above the heart originate from the neural crest. NC-originating VSMC have been found in the perivascular regions starting from the distal pulmonary trunk and outflow tracts up to the neck, face and ventral/anterior brain [105–108]. Similarly, the aorta, which partially loops above the heart, is invested with NC-originating VSMC at the aortic arch, ascending aorta, and branching arteries including the carotid arteries and right subclavian artery [105,108]. However, VSMC of the dorsal/posterior brain derive from the PM [108]. VSMC also arise from the LPM-derived secondary heart field and proepicardium. They are situated at the heart level and include the coronary arteries and veins, the proximal pulmonary trunk and outflow tract, aortic root [106,107,109–112], and abdominal aorta [112,113], although some NC-derived VSMC have also been found in the proximal coronary artery [105]. Lastly, PM-derived VSMC typically constitute regions most distal from the heart, such as the vessels in the limbs, body walls, and upper and middle descending aortas [112,114,115].

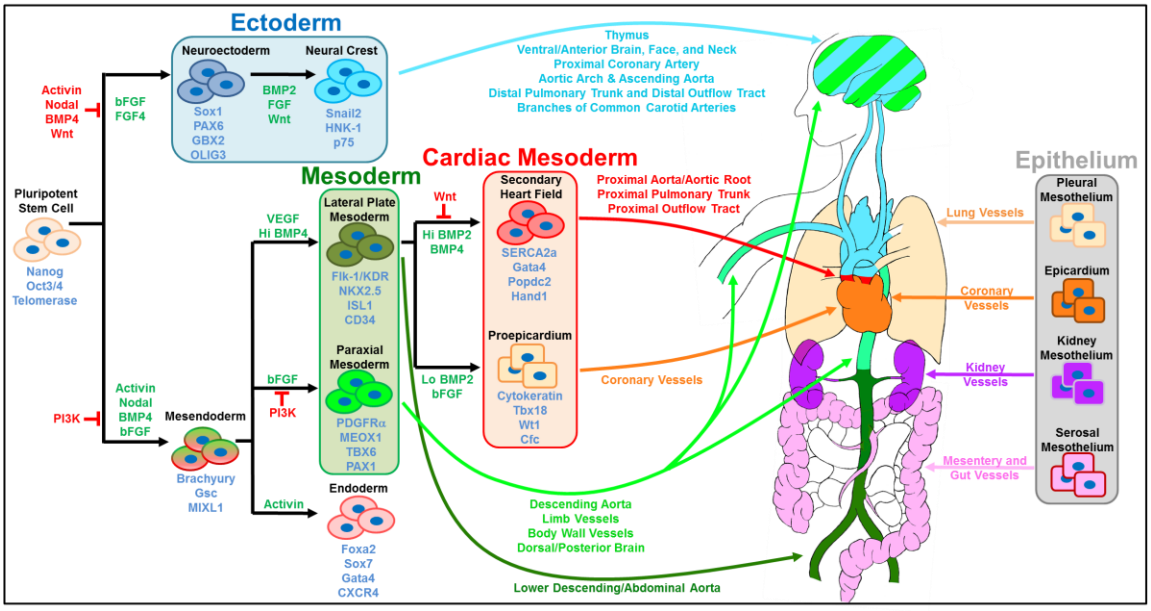

Figure 3.1 *Heterogeneity of mural cell development. Stem and progenitor cells cycle through several developmental stages before ultimately committing to a mural cell fate. Moreover, the specific path a cell undertakes will determine its final anatomic location and specific function. The signaling pathways depicted in this study are a culmination of information from various chemically defined in vitro differentiation schemes and where data were lacking, from in vivo and ex vivo studies. However, not all steps in embryonic development have been recapitulated in vivo and in vitro, nor have all known mural cell subphenotypes been generated using in vitro differentiation methods.*

It is noteworthy that VSMC progenitors are found not only in the developing embryo but also within adult tissues. Approximately one tenth of the post-development perivasculature consists of cells that express progenitor markers such as stem cell antigen-1 (Sca-1), c-kit, CD34 and CD309 [116,117]. In vivo, these cells are held undifferentiated within progenitor niches while mature cells reside around them. These progenitor reservoirs become active and serve as replenishable cell sources during tissue disease and wound healing, and as such, are studied for their potential in cellular therapies. It is speculated that adult progenitors are embryonic precursors held back in progenitor niches [63] and presumably lie in between an embryonic progenitor and a VSMC along the developmental timeline. Therefore, in vitro analogs of VSMC progenitors, which generate VSMC through PSC-derived analogs of adult progenitor intermediates, may serve as an additional checkpoint for further purification and verification of the developmental path.

3.1.2 Signaling Pathways Directing Vascular Smooth Muscle Fate

Commitment to a VSMC precursor only brings the cell halfway towards its ultimate identity. Before VSMC can be found in the developing embryo, VSMC precursors can be identified as PDGFR-β positive cells scattered around the developing vessel mesenchyme [118,119]. These cells are recruited into the first layer of VSMC by a number of soluble, cell-cell, and cell-matrix signals [120]. Likewise, adult VSMC precursors will differentiate when their precursor niche is altered by disease states.

The many in vivo signals known to be critical to VSMC recruitment can be used to direct VSMC fate in vitro (**Fig. 3.1**). Briefly, the soluble signals PDGF-ββ and TGF-β1 are the most well-known for in vivo and in vitro VSMC development. However, less studied factors such as sphingolipids, cell-cell contact signals, retinoids, mechanical forces, and ECM have also been shown to be necessary in VSMC fate.

VSMC signaling pathways have been shown to direct VSMC differentiation from many progenitor types of different species and origins. Therefore, many VSMC differentiation signaling pathways may be universal across different VSMC progenitors. Furthermore, many of these developmental pathways are retained in mature VSMC and continue to upregulate many VSMC-specific contractile markers in adult cells (a notable exception is PDGF-ββ which negatively regulates mature VSMC markers [90]). As such, signaling studies for VSMC development may extrapolate towards signaling studies for VSMC phenotype modulation and vice versa.

PDGF-ββ

EC secrete PDGF-ββ during the early stages of vessel development where the ligand finds its way to surrounding VSMC precursors and recruits them to the developing VSMC layers [119]. PDGF-ββ's important role in VSMC and PC development is highlighted by murine mutant models where inhibition of the ligand, receptor, or downstream events usually result in poor VSMC recruitment as indicated by sparse VSMC coverage, leaky vessels, and embryonic lethality [26,87,119,121].

While PDGF-ββ and its receptor PDGFR-β are the most implicated in VSMC development, there exists several isoforms of both the ligand and receptor. In total, there are four ligand monomers (A-D) which form five dimers (PDGF-αα, αβ, ββ, CC, DD) and two receptor monomers that form two receptor tyrosine kinase (RTK) dimers (PDGFR-α, αβ, β) [122]. Our isoforms of interest, PDGF-ββ and PDGFR-β, have especially high binding affinity to each other, though the ββ ligand

can also activate the other two receptor isoforms and the β receptor can also be activated by PDGF-DD [123].

On presumptive VSMC, PDGF-ββ binds to the receptor tyrosine kinase (RTK) PDGFR-β and proceeds to activate a multitude of RTK pathways [124]. Here, Src, Grb2, PI3K, Ras, SHP-2, PLCγ, and other unstudied pathways act coordinately to induce SMC differentiation where ablation of a single pathway does not completely abolish PDGF-ββ's effects. One target of these pathways is ERK, which is known to be upstream of MYOCD, a well-studied transcriptional cofactor of SMC genes [125].

The PDGF-ββ pathway is often associated with VSMC proliferation as it induces the proliferative/synthetic phenotype in mature VSMC [90]. Similarly, PDGFR-β+ cells in the pericapillary of the developing embryo proliferate in response to PDGF-ββ. Knockout of the ligand inhibits this proliferation and causes lethal vascular defects [119] while overexpression exacerbates proliferation resulting in an abnormally thick medial layer [126]. Although proliferation is often viewed as mutually exclusive to differentiation, PDGF-ββ has been shown to facilitate VSMC differentiation in many in vitro models ranging from PSC derived LPM, PM, and NC cells [12,127,128] to a wide variety of adult progenitors [129–133].

TGF-β

TGF-β is another growth factor that induces VSMC differentiation in vivo and in vitro. This ligand comes in three isoforms, TGF-β1/2/3, and targets several receptors on VSMC cells - Alk-5 (also known as TGF-βRI), Alk-1 (TGF-βRII), and endoglin (CD105) [134,135]. The three receptors coordinately direct the phosphorylation of Smad1/5/7 or Smad2/3, both of which associates with Smad4 and localizes to the nucleus to activate transcription factors.

In mouse models, impairment of the TGF-β pathway through SMC-specific deletion of Alk-5 [136] or endoglin [137] leads to poor SMC recruitment while epicardial-specific deletion of Alk-1 prevents the epithelial to mesenchymal transition of the epicardium into VSMC [138]. Similarly, in vitro, TGF-β1 has been used extensively for VSMC differentiation as demonstrated with multipotent adult stem cells [130,133,139] and in vitro analogs of embryonic precursors [12,128,140,141]. Though less utilized, TGF-β3 has been demonstrated to induce SMC differentiation in MSC [139,142].

Although it is unclear how the TGF-β receptors activate the different Smad pathways [143], Smad2/3 has been demonstrated to be critical for VSMC development. During VSMC differentiation, the Smad2/3/4 complex translocates to the nucleus where it activates transcriptional activators of SMC genes such as MYOCD of MSC in vitro [142] and MRTF-B of NC cells in mice and in vitro [144]. Furthermore, siRNA inhibition of Smad2/3 impairs the differentiation of SMC from embryoid bodies (EB) [145].

Retinoic Acid

Retinoic acid (RA), also categorized under vitamin A, is responsible for the development of many tissues. RA can bind to three nuclear membrane RA receptors (α, β, or γ RARs) which then form dimers with RXRs (α, β, or γ) [146,147]. After recruiting coactivators, the dimer may induce epigenetic changes or bind to cofactors to activate transcriptional activity of development-related genes [148].

The earliest models of PSC to SMC differentiation used RA in an EB model [149]. Since then, RA has been used to induce SMC in a variety of cell types of different species in EB or monolayer induction [145,150–152]. Interestingly, SMC origin need not be specified as RA and serum can direct PSC towards SMC in one-step differentiation protocols, making RA protocols among the simplest to execute. Origin specification is still an option as RA can also guide multipotent SMC precursors towards SMC fate [12,150]. Furthermore, it has been shown that RA upregulates MYOCD during in vitro SMC differentiation [150].

Although RA mediates vascular development in vivo [153] its effects are not limited to vascular cells, but also contributes to the organization of many embryonic organs [154]. Likewise, RA-mediated differentiation of PSC yield not only SMC but also cardiomyocytes, skeletal muscle, and neuronal cells depending on the concentration of the ligand [155,156].

Biochemical Signaling in the Extracellular Matrix

Biochemical regulation of VSMC fate is not limited to soluble signals as VSMC precursors are also stimulated by ECM ligands through integrin receptors. There are a total of 18 α and 8 β integrin subunits which combine to form at least 24 integrin dimers [157]. These integrins mechanically couple the cell to the ECM and activate focal adhesions and downstream pathways that play direct roles in regulating cytoskeletal components and therefore cell migration, cell shape, and cell differentiation [158].

Typically, VSMC specific knockout of integrin receptor subunits such as β1 [159], α4 [160], α7 [161], α5 and αv [162], but not α5 alone [163], yield similar phenotypes with disturbed VSMC recruitment and vessel organization. However, these defects are not the result of ablated VSMC differentiation but rather impaired migration, proliferation, and association with maturing vessels. Knockout of the downstream focal adhesion protein α-parvin yields similar effects where VSMC recruit improperly and respond abnormally to PDGF-ββ mediated chemotaxis [164]. Similarly, deletion of the ECM proteins themselves can cause deficient VSMC recruitment as was the case with brain vessels and astrocyte-specific laminin-γ1 knockout [165].

It is clear that ECM are critical components for VSMC development, but which ECM proteins constitute the correct microenvironment? This is difficult to answer as the vessel's ECM changes as the vessel matures, and there are multiple distinct vessel layers each with unique ECM composition. Furthermore, the vessel layers form sequentially during embryonic development, starting with the initma and building toward the adventitia. Therefore, vascular precursors sense different ECM compositions at different stages of vascular maturity.

In a mature blood vessel wall, the bulk of the main structure and mechanical strength is constituted by fibronectins (FN), laminins (LN), elastin, and collagens. Further structural support and function is provided by fibrillins and fibulins, which form microfibrils, nidogen and perlecan which tie together other ECM, and HSPG which provide additional binding sites for integrins and soluble proteins. Note this is a general overview, as detailed descriptions of each ECM protein will indicate overlapping roles (reviewed in detail by Rhodes et al. [166] and Kelleher et al. [167]).

The blood vessel architecture is formed from multiple distinct layers with unique ECM compositions [167]. At the lumen face, the tunica media contains EC held primarily within fibronectin. This layer rests on the basement membrane which consists mainly of collagens, laminin, enactins, Von Willebrand Factor (vWF), HSPG, and in microvasculature, PC [168]. Around the

basement membrane lies the internal elastic laminae, a cell-free tissue of primarily elastins and microfibrils. Between the internal, and a similarly composed external, elastic laminae lies the tunica media. The tunica media is constituted by alternating layers of VSMC in collagens and more cell-free lamellae composed of elastin and microfibrils [158,167]. Circumferenced around the other layers, the adventitia is comprised of fibroblasts in collagen-rich ECM. These specific ECM compositions play key roles in vascular function and transduce biochemical and mechanical signals necessary for proper recruitment of VSMC.

For in vitro cell culture, the ECM substrates typically used are fibronectin, laminin, vitronectin, collagen, or its denatured form, gelatin. Of these ECM, collagen-type IV (CIV) and gelatin have been used extensively to derive VSMC [12,51,151,169]. Indeed, blocking antibodies against integrin subunits α_1, α_v, or β_1 repressed the collagen IV-mediated VSMC differentiation of mESC-derived Sca-1+ progenitors [132]. Although few studies directly compare the in vitro effects of ECM composition on VSMC differentiation, it was shown that cardiac progenitor cells in SMC maintenance media with PDGF-ββ most preferentially differentiated into SMC in FN compared to LN, CIV, vitronectin, and gelatin [170]. In contrast, MSC in MSC maintenance media has the highest expression of SMC markers on CIV over LN and FN [171]. However, with a simple media of DMEM and serum, MSC prefer SMC differentiation under collagens, elastin, and FN over LN [172]. These studies highlight the fact that ECM effects on SMC differentiation are coupled with the progenitor type and other microenvironment conditions.

Growth Factors in the ECM

A major role of the ECM is to bind soluble ligands that would otherwise have limited exposure to their target cells. Able to bind both cell integrins and soluble growth factors, the ECM is able to concentrate soluble signals to cell surface receptors [173]. This localization is primarily attributed to HSPGs [174] but other proteins, such as laminin and fibronectin [173], also have soluble signal binding domains. Many growth factors and cytokines bind to ECM, including the PDGF and TGF-β families that are necessary for VSMC development [173,174].

Currently, there are no in vitro studies that demonstrate ECM-bound soluble signals for the differentiation of VSMC. However, the in vitro implications are demonstrated through in vivo studies where matrix-bound PDGF-ββ has been shown to be necessary to maintain the microenvironment for mural development.

In vivo, mutant mice with the deleted ECM sequence that binds PDGF-ββ (known as the retention motif) resulted in impaired PC recruitment to the retinal and glomerular microvessels [87]. In addition to decreased PC density, it was found that PC migration and dendritic extensions were likely guided by the concentration gradient of ECM-bound PDGF-ββ. Similarly, interference with the N-sulfation of heparin sulfates prevents proper recruitment of PC to mice hindbrain microvessels [175]. In mice tumor microvessels supplemented with exogenous retention motif, PC demonstrated improper recruitment with enlarged microvasculature compared to wild type controls [176]. Overexpression of PDGF-ββ by the tumor cells did not restore tight PC-EC attachment, demonstrating that ECM-bound PDGF-ββ has unique mural recruitment mechanisms distinct from that of its soluble counterpart.

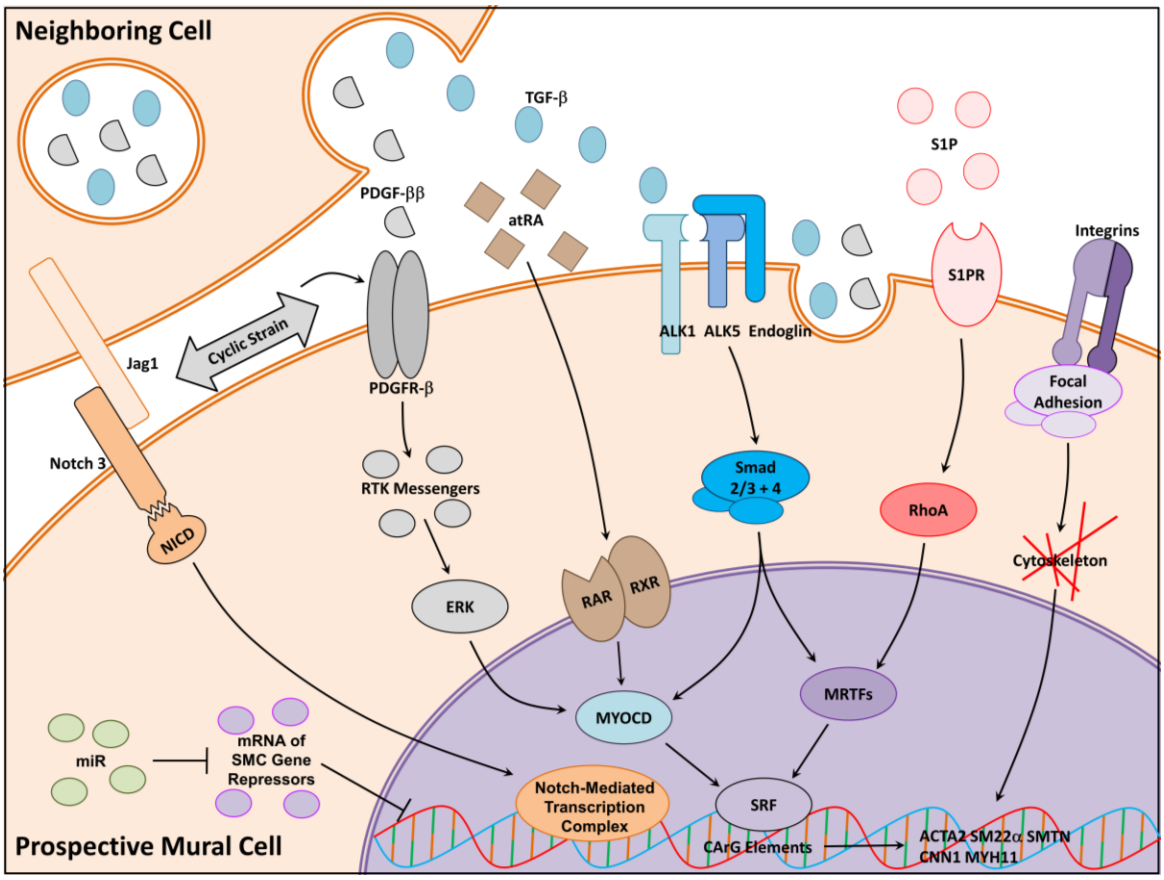

Figure 3.2 *Signaling pathways for mural differentiation. Mural development occurs through the combinatorial effects of multiple signaling pathways. Shown in this study is a simplified depiction of the major pathways and their key ligands, receptors, intermediates, and transcriptional regulators necessary for mural differentiation.*

Considerations for Combinatorial Signaling In Vitro

By far, the most popular in vitro differentiation signals for VSMC differentiation are PDGF-ββ and TGF-β1. However, there are many more microenvironment factors and pathways that are required for VSMC fate. These necessary signals are implied to be endogenously expressed, but few studies explore their exogenous potential. Ideally, though impractically, these factors would be tightly controlled in the perfect in vitro differentiation model. Likewise, the parameters of each signal, such as ligand concentration in soluble signals, would be considered. Currently, differentiation protocols typically focus on one or two of these signals.

3.1.3 Developmental Timescale and VSMC Function

During in vitro differentiation, the proceeding final step is the assessment of the product cell and determination of protocol success. Typically, this process involves the characterization of markers and functions of the product cell. There are two key properties to cell markers and function, ***specificity*** and ***timescale***. Together, the information on the specificity and kinetics of differentiating

cells can be used to determine a cell's degree of commitment to a specific lineage and resemblance to its in vivo counterpart.

In vivo, initiation of heartbeat, blood flow, and consequent hemodynamic forces occur right before the onset of VSMC marker expression [89,177]. It is thought that these hemodynamic forces, particularly circumferential cyclic strain, play a significant role in the recruitment of VSMC. The earliest indicator of VSMC lineage is the expression of PDGFR-β in the developing vascular mesenchyme [118]. These cells migrate toward the endothelium where they form an initial perivascular layer in direct contact with EC [112,118]. Around this time, these cells will express the first contractile marker, αSMA [115,118,178,179]. VSMC progenitors may also express SMC gene regulator, SRF, which will catalyze the eventual synthesis of intermediate to late stage VSMC contractile markers [178]. At this time in development, there is no clear distinction between the future PC-populated basal lamina and VSMC-populated tunica media [118]. Potentially, the early αSMA+ cells may be αSMA+/neural/glial antigen 2+ (NG2) (some of which are also desmin+ [119]) ancestors of both VSMC and PC [180,181]. This progenitor's lineage choice may be distinguished by its αSMA expression, the persistence of which may indicate VSMC fate and the discontinuation of which would may indicate PC fate [180].

If a progenitor chooses VSMC fate, it will then begin building SMC-specific contractile machinery. Chronologically, the presumptive VSMC will express SM22α [179], calponin-1, h-caldesmon [179,180], then the SM1 isoform of SMMHC [182]. Sometime after caldesmon expression, the VSMC-ensheathed vessel will gain stability and resistance to hyperoxia [180]. Vascular cells will begin to upregulate production of collagens and elastin, ECM proteins that constitute the majority of the tunica media [167]. VSMC will also begin forming additional perivascular layers while aligning circumferentially [118]. As the contractile complex develops, VSMC will acquire intermediate filaments, followed by dense bodies, then thick filaments [183]. Finally, the VSMC will complete its toolset with the expression of smoothelin-B [184], then close to birth, the expression of the SM2 isoform of SMMHC [185–187].

Generally, VSMC markers later in the developmental timeline are more lineage-specific. One of the earliest markers, PDGFRβ, is the most nonspecific VSMC marker mentioned in this review. While it is expressed in both mural cells, it is also expressed in other vascular cells including vascular progenitors [131], endothelial cells [188], fibroblasts [189], and a number of non-vascular embryonic and adult cell types [190]. αSMA is the next earliest marker and is also found in vascular progenitors [130,191] while αSMA and SM22α can both be found in myofibroblasts [192]. Furthermore, αSMA, SM22α, and calponin-h1 are all transiently expressed in early embryonic cardiomyocytes and skeletal muscles [179,193–195]. The markers that are exclusive to VSMC are h-Caldesmon, smoothelin-B, and the SM1 and SM2 isoforms of SMMHC [196].

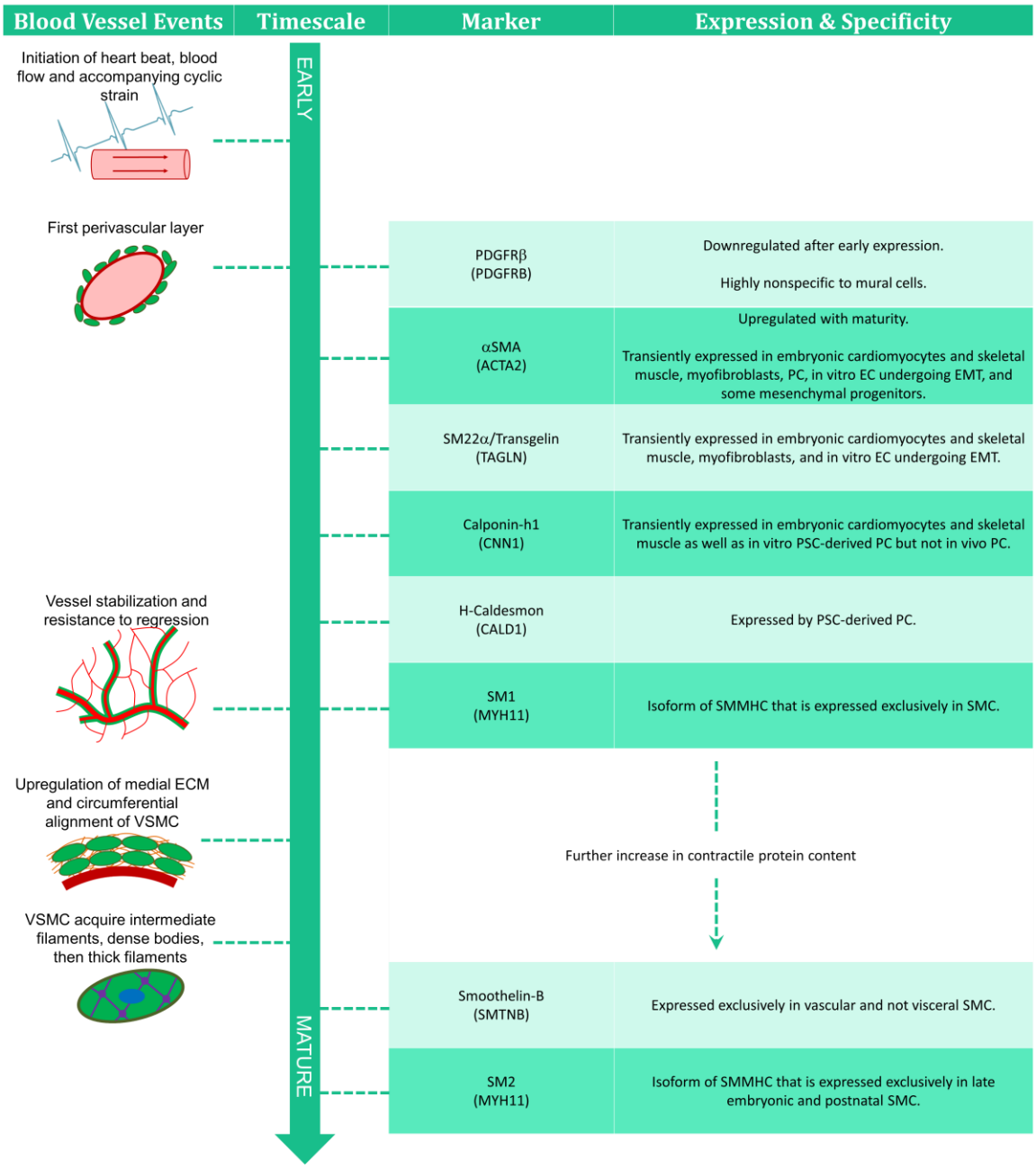

Figure 3.3 *Developmental timeline of the vascular smooth muscle cell. VSMC express their multitude of characteristics with varying lineage specificity and time points in development. Therefore, the presence or absence of certain traits can indicate the cell's degree of VSMC commitment and maturation level. Note that in embryonic development, timescales will vary across species and vessel location. As such, this diagram estimates the relative occurrence of events and marker acquisition. VSMCs, vascular smooth muscle cells.*

Functionally, mature VSMC regulate vessel tone by contracting in response to agonists such as angiotensin II, endothelin, and carbachol [152,197,198]. Also, VSMC would exhibit phenotypic

modulation (downregulation of contractile markers and increase of proliferation, migration, and ECM remodeling proteins) under dedifferentiation factors such as PDGF-ββ and serum (reviewed in detail by Owens et al. [90]).

An important consideration, vascular SMC are not easily distinguishable from visceral SMC. Aside from anatomic location, the most apparent distinction is in contraction, where SMC of different organs will display varying degrees of tonic or phasic activity [199]. However, this distinction is lost in vitro as the molecular makeup of the SMC types are not so different and cellular contractions are not signaled by their native microenvironment. Indeed, all VSMC contractile markers are also expressed in visceral SMC with the exception of the vascular-specific smoothelin-B [12,184,200]. Other differences between vascular and visceral SMC are relatively minor, including the vascular SMC's higher vimentin-desmin ratio and αSMA content [201] and the visceral SMC's additional 7 amino acid sequence on SMMHC heads [202]. Furthermore, large-scale gene analysis reveals that vascular SMC, compared to visceral SMC, preferentially express genes related to the activation of the TGF-β pathway, activation of the immune system, and communication with EC [203]. This hints at many potential distinctions between the two SMC and further studies are needed to distinguish specific properties for in vitro identification.

A key function of VSMC is the integration and stabilization of vasculature. This behavior can be observed by simply seeding VSMC with EC undergoing angiogenesis. Typical techniques include in vivo implantations with Matrigel plugs [12,128], in vitro Matrigel vasculogenesis assays [133], and microfluidic devices for generation of in vitro perfusable vessel formation [204]. With the inclusion of VSMC, these nascent vessels may display attributes associated with stability and tone regulation such as the narrowing of vessel diameter, increased longevity, decreased permeability, and contractile function [204–206].

Furthermore, VSMC are significant contributors to vessel wall remodeling and express a variety of ECM, MMP, and TIMP [128,207,208]. However, most cell types contribute to the surrounding ECM to some degree, and ECM proteins are not specific to any one tissue. Therefore, there is a large degree of nonspecificity regarding the expression of any ECM and ECM-related protein.

3.1.4 Considerations for Generating Pure VSMC Populations in Vitro

A major challenge in stem cell engineering is the generation of pure cell populations. Heterogeneous populations can exhibit unpredictable and undesirable behaviors when used in research or clinical applications. Specifically, for the clinical application of PSC-derived populations, any remaining pluripotent cells risk the formation of cancerous teratomas. In fact, the ability to form teratomas is a hallmark of PSC [48]. So how can we achieve the generation of pure VSMC populations? Typically, cells can be purified via flow cytometry where the cell in question must express a highly lineage-specific surface marker set. Failing that, as in the case with VSMC, the process of generating pure populations becomes a significant challenge.

VSMC do not express lineage-specific surface receptors nor receptor combinations. All specific proteins are located within an internal contractile complex, making purification via flow cytometry impossible without modifications to the cell. Because VSMC uniquely express SMMHC, which has not been found any other cell type thus far [182,209], the expression of SMMHC alone is near definitive proof of VSMC lineage. Transgenic cells that express fluorescent labels or puromycin resistance have been developed with SMMHC [197,198,210]. While these transgenic cells can be purified to produce high purity VSMC populations, the addition gene modification step may not be

practical in a clinical application setting. However, VSMC progenitors are varied and numerous with many potential surface markers. A viable alternative would be the purification of an intermediate population combined with a highly efficient differentiation protocol.

3.1.5 The McCloskey Lab's Expertise in Vascular Tissue Engineering

The McCloskey lab has previously established a protocol for the chemically-defined generation of ECs from human [23] and mouse [48–50] PSC sources. The protocol is multistage and first creates a kinase domain receptor (KDR) positive, multipotent progenitor before inducing EC fate. This KDR+ progenitor (also known as a vascular progenitor cell, VPC) is analogous to a cell in embryonic development's LPM and is known to be multipotent for both ECs and VSMCs [51]. The McCloskey lab is in the process of modelling the codifferentiation of ECs and VSMCs from VPCs.

The McCloskey lab also has expertise in forming microvasculature within the compartmentalized environment of microfluidic devices [46]. These devices typically drive vasculogenesis of human umbilical vein ECs (HUVECs) via direct contact with fibrin gel and paracrine signaling from fibroblast cocultures [47]. The McCloskey lab is in the process of improving microfluidic vascularization by optimizing the different mural cell types that are cocultured. Furthermore, to move towards the long-term, clinical goals of the regenerative medicine field, the McCloskey lab wants to induce vasculogenesis with PSC-derived cell types.

To support the goals of the McCloskey lab, I aimed to derived VSMC from PSC. Specifically, I aimed to generate VPC via the lab's well-established protocol, then guide the VPC to VSMC fate. As VSMC cannot be purified, I aim to optimize conditions to generate high purity populations of PSC-derived VSMC.

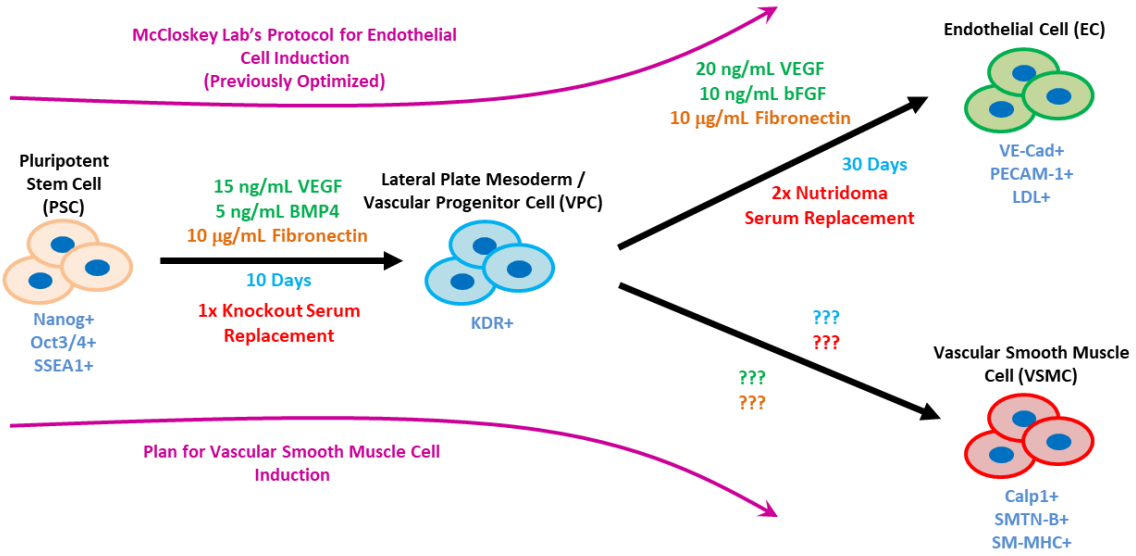

Figure 3.4 *Adapted protocol for VSMC generation from PSC. The McCloskey lab has previously established a protocol for EC generation from PSC via a VPC intermediate. I will instead guide this VPC intermediate to VSMC fate by optimizing the growth factors, ECM, serum replacement, and timescale for differentiation.*

3.2 Materials & Methods

3.3.1 Mouse Embryonic Stem Cell Culture

A3 and R1 mouse embryonic stem cells (mESC) are maintained on a feeder layer of mitomycin c-treated mouse embryonic fibroblasts (MEF) seeded on 0.5% gelatin-coated plates. The cells are collectively maintained with chemically defined media containing Knockout Dulbecco's Modified Eagle Medium (Invitrogen), 15% Knockout Serum Replacer (KSR; Invitrogen), 1x Non-essential Amino Acids (Invitrogen), 1x Penicillin-Streptomycin (Invitrogen), 2mM L-glutamine (Invitrogen), 0.1mM 2-mercaptoethanol (Calbiochem), 2000 Units/ml of leukemia inhibitory factor (Chemicon), and 10 ng/ml of bone morphogenetic protein-4 (BMP-4; R&D Systems). Media was refreshed every 2 days and cells were passaged via 1/2x Trypsin (Corning). Passaging included the use of 5 minutes of gravity separation to isolate healthy mESC from dead and MEF populations. Initial seeding density was 3-5k cells/$cm^{3.}$

3.3.2 Mouse Embryonic Stem Cell Induction

mESC were induced on 0.5% gelatin-coated plates without a feeder layer. The cells were exposed to a base media containing alpha-MEM (Cellgro), 1X penicillin-streptomycin (ThermoFisher), 1X nonessential amino acids (ThermoFisher), 2 mM L-glutamine (ThermoFisher), 0.05mM 2-mercaptoethanol (Calbiochem), and 20% fetal bovine serum (FBS, Corning). Optimizations varied the concentrations of all-trans retinoic (0-50 μM, atRA, Sigma) in the media, initial seeding density, and ECM coating of the substrate.

3.3.3 Intracellular Mouse Cell Staining

Mouse cells were first fixed with 4% paraformaldehyde (Tousimis) for 15 minutes at room temperature, permeabilized with 0.7% Triton X-100 (MP Biomedicals) for 5 minutes, then blocked in a cocktail of 1 mg/mL bovine serum albumin (BSA), 2% FBS, and 2% Human Fc Block (BD Bioscience) for 15 minutes. The cells were stained overnight with a 1:200 dilution of anti-αSMA-FITC (Sigma F3777), 1:100 dilution of anti-Calponin-h1 (Sigma, C2687), or 1:10 dilution of anti-MYH11-PE (Santa Cruz sc-6956). These stained cells were matched to respective isotype controls (Biolegend), processed on an LSR II flow cytometer (BD Biosciences), and analyzed on FlowJo (FlowJo).

For fluorescent microscopy, cells were stained with a 1:500 dilution of anti-αSMA-FITC (Sigma F3777) and 1:15000 dilution of anti-Caponin-h1 (Sigma, C2687).

3.3.4 Primary Mouse Vascular Cell Isolation and Culture

Mice from a number of strains (TgN(TIE2GFP)287Sato/J, C57BL/6-Tg(alpha SMA-RFP), xCDH5-CRE, Rosa-GFP, C57BL6, NSG, and CDH5-Cre x Rosa GFP) were rendered unconscious via cotton-ball soaked isoflurane exposure (Sigma) in a bell jar then euthanized via cervical dislocation. For sterility, the mice were thoroughly sprayed with 70% ethanol and dissected within a biosafety cabinet. The aorta was removed, and the adventitia was physically stripped.

To isolate primary mouse VSMC, the aorta was minced and incubated in 1.132 mg/mL Collagenase type II (Worthington) in phosphate buffered saline (PBS) at 37°C. Dissociated VSMC were plated on 0.5% gelatin (Difco) coated plates with SmGM-2 (Lonza) media. These cells were fed every other day and passaged with Trypsin (Corning).

To isolate primary mouse aortic endothelial cells (MAEC), the aorta was cut into small sections (several mms in diameter). Each piece was sandwiched in between two drops of Matrigel on 0.5% gelatin coated plates. Each piece was cut and oriented such that the lumen surface faced the bottom of the culture plate. These pieces were maintained with EGM-2 with Bulletkit (Lonza) with an additional 20% FBS that was refreshed every other day after initially waiting 4 days for cells to settle. After MAECs have migrated onto the plate, the aorta was removed, and the cells were maintained in EGM-2 with Bulletkit.

3.3.5 Human Pluripotent Stem Cell Culture

DF-10-0-7T human induced pluripotent stem cells (hiPSCs, WiCell) were cultured with mTeSR1 (Stem Cell Technologies) on a substrate of human embryonic stem cell (ESC)-Qualified Matrigel (Corning) at 37°C under 5% CO_3. Culture medium was refreshed every day and cells were sub-cultured every 3-4 days using Accutase (Stem Cell Technologies) as the lifting reagent.

3.3.6 Human Pluripotent Stem Cell Induction

hiPSC are induced with a base media consisting of α-MEM (Cellgro), 20% knockout serum replacement (ThermoFisher), 1x penicillin-streptomycin (ThermoFisher), 1x nonessential amino acids (ThermoFisher), 2mM L-glutamine (ThermoFisher), and 0.05mM 2-mercaptoethanol (Calbiochem).

hiPSC are first induced to KDR+ VPCs for 10 days on 100 mm, 10 ng/mL fibronectin-coated plates with the aforementioned base media supplemented with 15 ng/mL vascular endothelial growth factor (VEGF, Peprotech) and 5 ng/mL basic fibroblast growth factor (bFGF, Peprotech). The initial seeding density is 10,000 cells/cm^2 and the hiPSC are subcultured on the 5^{th} day. Cell media is refreshed on the 3^{rd} and 8^{th} days.

Sorted cells are cultured in induction media supplemented with an additional 5 μM Rho Kinase Inhibitor (STEMCELL Technologies) for 24 hours after sorting.

KDR+ progenitors are further induced in the base media supplemented by any combinations of platelet derived growth factor beta (0-50 ng/mL, PDGF-ββ, Peprotech) and/or transforming growth factor beta 1 (0-25 ng/mL, TGF-β1, Peprotech). Optimizations also varied the initial seeding density, ECM coating of the substrate . Where specified, KSR is replaced with 2x Nutridoma (Sigma).

3.3.7 Human Cell Staining

For extracellular markers, human cells are filtered through a 100 μm strainer (Corning) and stained at 5-20 million cells per mL with a 1:75 dilution of anti-CD309-PE (also known as KDR, Biolegend 359904), anti-PDGFR-β-APC (Biolegend 323608), and 1:1000 of a Viability Fixative e780 (eBioscience 65-0865-14) in media on ice for 15 minutes.

For intracellular markers, human cells are stained at 200,000 cells per mL with either: 1. the Transcription Factor Staining Buffer Set (eBioscience 00-5523-00) according to manufacturer instructions with a 24 hour staining time or 3. fixation with 4% paraformaldehyde (Tousimis) for 15 minutes at room temperature, permeabilization with 0.7% Triton X-100 (MP Biomedicals) for 5 minutes, then staining overnight. Analysis of hiPSC pluripotency was done with method 2 and a 1:50 dilution of anti-Oct3/4-PE (eBioscience 12-5841-82). Other antibodies, their dilutions, and other staining parameters will be listed with the results.

3.3.8 Statistical Analysis

All statistical significance was performed with unpaired, two-tailed, heteroscedastic, student's t-Tests.

3.3 Results & Discussion

3.3.1 Optimization of Mouse Vascular Smooth Muscle Fate

3.3.1.1 Optimization of VSMC Fate from A3 mESC

I began optimization of VSMC fate using atRA. An immediate challenge of using this method is the inherent toxicity of atRA. I induced a set of A3 mESC for 6 days at various concentrations of atRA from 0 to 50 µM. I quantified the cell count of each condition via hemocytometer along with their αSMA and SMMHC expression via flow cytometry. Results (**Figure 3.5**, N = 1) clearly indicate trend where increasing atRA concentration results in decreasing yield. Images of the cell culture reveal the qualitative information that increasing atRA concentration results in a larger fraction of nonadherent cells (data not shown). This information collectively implies that increasing atRA is correlated with increasing cell death. αSMA positive and SMMHC positive cell yields decrease along total cell yield. Therefore, even though atRA is an inducer of VSMC fate, its increasing concentration does not necessarily result in increasing VSMC yield.

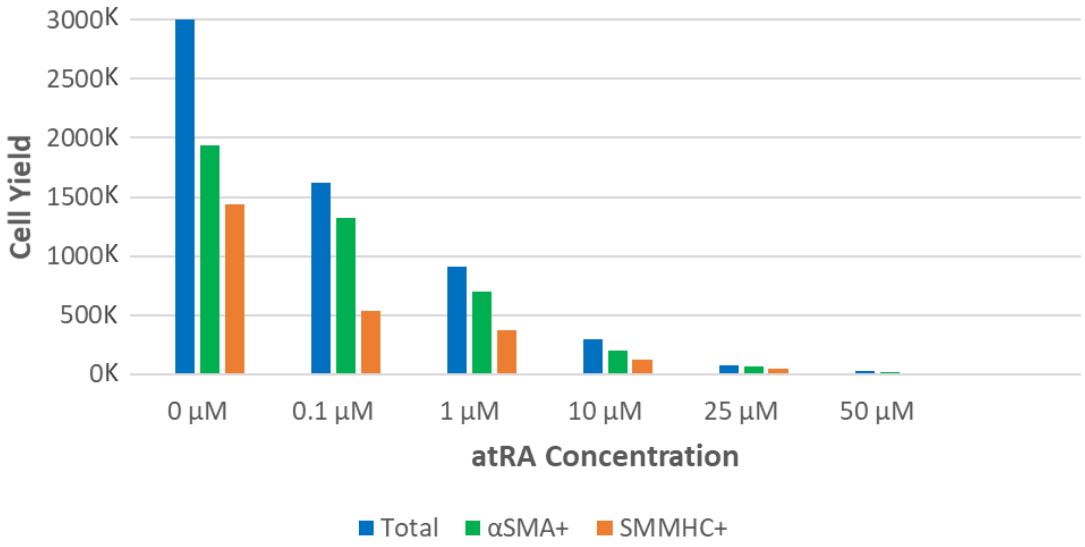

Figure 3.5 *The effects of atRA concentration in an A3 induction on total cell and VSMC yield in a 6-day induction and 5k cells/cm^2 initial seeding density on 0.5% gelatin coated substrate (N = 1). These an inverse relationship between atRA concentration and cell yields.*

Although increasing atRA concentrations result in decreasing yield, I explored the possibility that it would increase purity. As VSMC lacks surface markers, it cannot be easily sorted, making purity

an important result of a differentiation protocol [70]. I induced a set of A3 mESC at various concentrations of atRA from 0 to 50 μM and analyzed the results at days 6, 9, and 13. Results (**Figure 3.6**, N = 1) indicate that atRA concentration has little effect on resulting VSMC purity. Surprisingly, a complete absence of atRA yields a similar result to any condition containing atRA. This result is difficult to explain as it appears highly coincidental that just serum can guide a significant fraction SMC fate. Perhaps this is simply noise from the undefined nature of serum and an N = 1. Or, as I will explain later in the chapter, there can be significant issues with VSMC marker antibodies. However, compared to an absence of atRA, cells exposed to atRA demonstrate an elongated, striated morphology associated with muscle cells (**Figure 3.6B**).

Meanwhile, increasing the time scale beyond 6 days results in a steady decrease in the percentage of the population with SMMHC. After 6 days, the αSMA percentage increases to near 100%. This result is congruent with the paradigm of VSMC plasticity where mature VSMC will dedifferentiate after exposure to high concentrations of serum. This dedifferentiation results in a loss of mature marker expression such as SMMHC [70].

To demonstrate that this atRA induction protocol was applicable to the other mESC cell lines, R1 mESC were induced with 25 μM of atRA and stained with VSMC markers then imaged with fluorescent microscopy (**Figure 3.6C**).

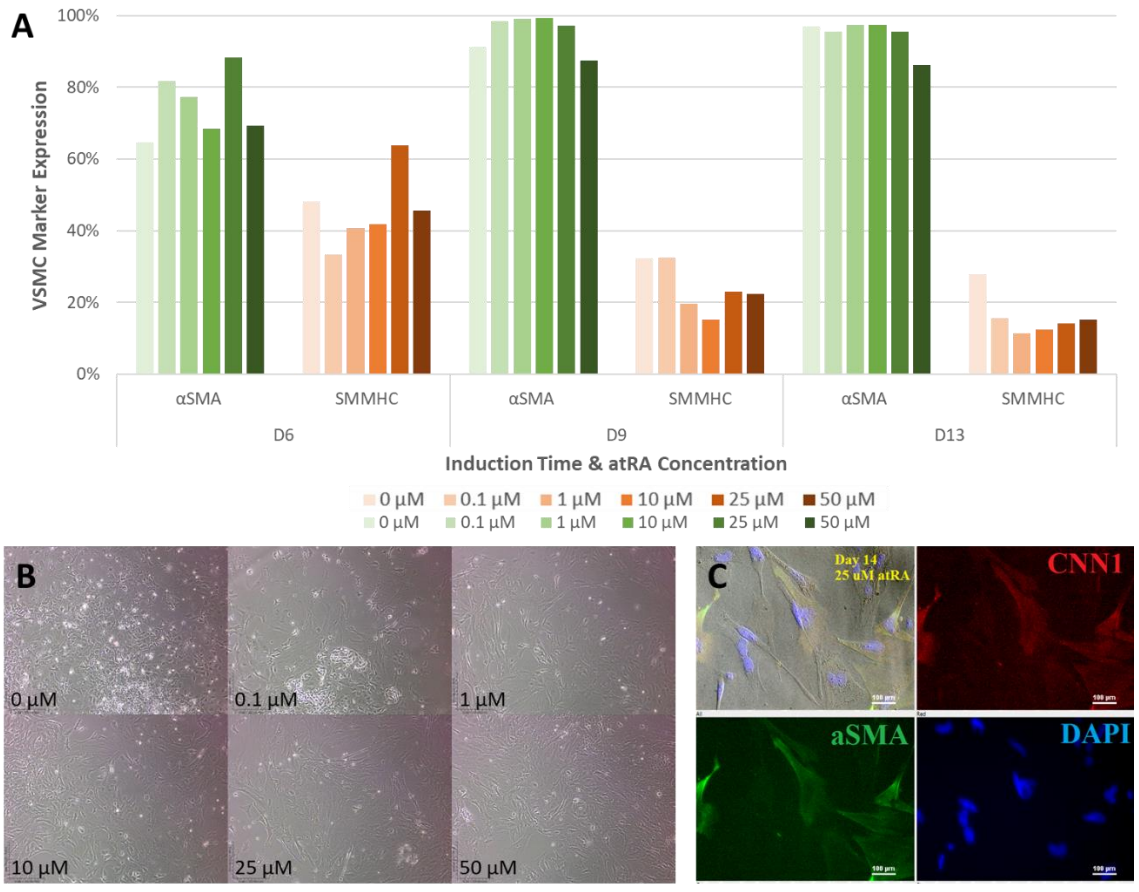

Figure 3.6 *atRA-based induction of VSMC from mESC.* ***A)*** *Percentage VSMC marker expression induced with 0.5% gelatin with respect to changing atRA concentration and induction time (N = 1).* ***B)*** *Cell morphology at day 6 with respect to changing atRA concentration.* ***C)*** *Fluorescent imaging of R1 mESC-derived VSMC after 14 days of 25 μM atRA exposure.*

Next, I attempted to optimize for purity with different ECM substrate. I induced a set of A3 mESC for 13 days with 10 μM atRA with either μg/mL collagen IV (CIV), 50 μg/mL laminin (LN), 50 μg/mL fibronectin (FN), and 0.5% gelatin. Results (**Figure 3.7**, N = 1) indicate that CIV yields the highest purity of SMMHC followed by G, FN, then LN. Gelatin and CIV yield the highest αSMA expression and these two ECMs can be considered to yield the highest purity of VSMC. This is congruent with the fact that in vivo, CIV is most closely associated with VSMC as CIV resides alongside VSMC in the tunica media [168]. Gelatin is a denatured form of CIV while FN is found on the lumen face of the vessel with the ECs and LN is found in the basement membrane alongside PC [158,167].

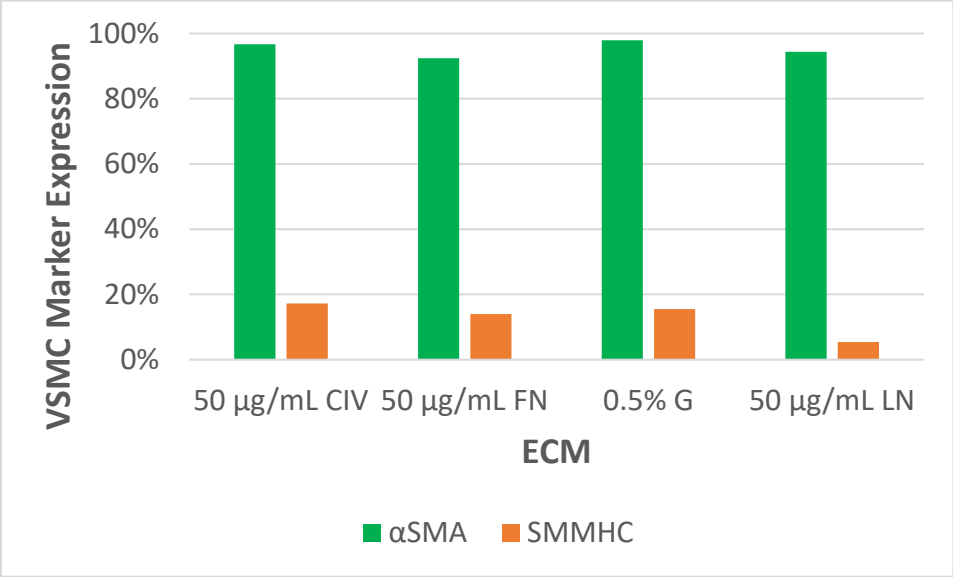

Figure 3.7 *The effects of different ECM on VSMC marker expression in an A3 induction with 5k cells/cm^2 initial seeding density taken to 13 days with 10 μM atRA (N = 1). CIV yields the greatest SMMHC expression while gelatin yields the highest αSMA expression.*

Next, I attempted to optimize for purity by varying initial seeding density. I induced a set of A3 mESC for 9 days with 10 μM atRA with an initial seeding density of 1,000 cells/cm^2, 5,000 cells/cm^2, or 20,000 cells/cm^3. Results (**Figure 3.8**, N = 1) indicate that lower initial seeding densities correlate with higher SMMHC expression but lower αSMA expression.

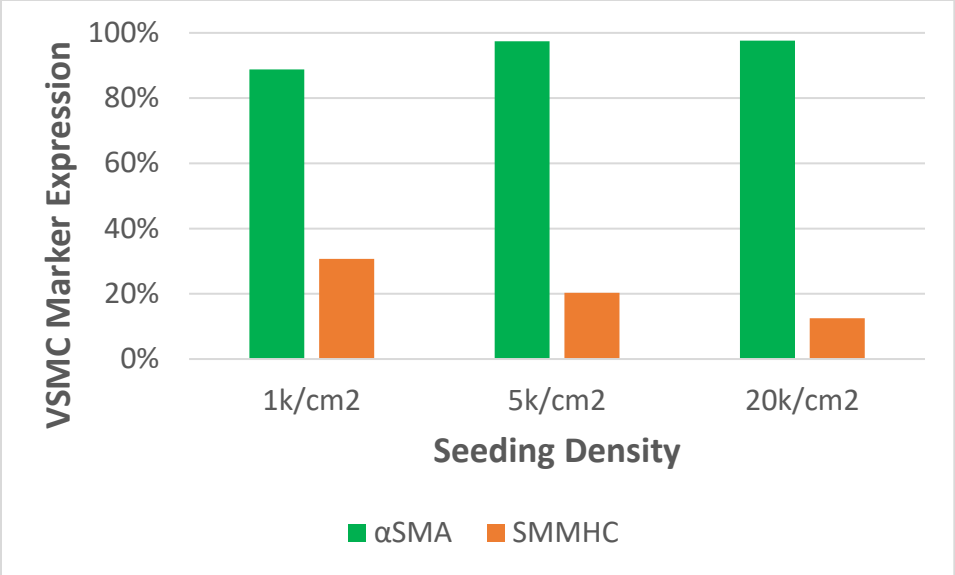

Figure 3.8 *The effects of different initial seeding densities on VSMC marker expression in an A3 induction with 0.5% gelatin coated plates and 10 μM atRA (N = 1). Lower seeding densities correlate with higher SMMHC expression but lower αSMA expression.*

Optimization of Primary VSMC Isolation

I also sought to compare my derived cells with its primary counterpart by isolating and analyzing mouse aortic smooth muscle cells (mASMC). After surgically extracting the aorta, the cells need to be isolated via collagenase digestion (**Figure 3.9A**). This was a sensitive process that did not yield any or too few attached cells in the initial trials and required optimization.

The parameters of consequence involved the digestion and initial seeding density of the aortas (**Figure 3.9B**). For the thick layers of ECM in the tunica media to be digested properly, the aorta needed to be thoroughly minced. This was not achievable until the purchase and use of surgical grade dissection scissors. It also required cutting until the aorta was no longer reduceable, which took 5 minutes per aorta. Furthermore, the minced aorta needed to be digested in a collagenase solution for over 1 hour, or else cells would not be released. The released cells would not survive until a minimum seeding density was achieved. This number was optimized to 2 aortas per a 6 well plate (9.5 cm^2 growth area).

Other potentially consequential concerns were explored, including the age of the mice, media refreshment time after plating, and aorta idle time in PBS. Cells are known to be less proliferative as they age, which could impede the isolation and expansion of mASMC with older mice. This concern was eventually dismissed after the successful isolation and expansion of mice that were over a year old. The newly isolated mASMC also required some time to settle and attach to the plate. However, longer wait times could mean that the cells exhausted their supply of nutrients before media refreshment. After a week-long wait yielded viable cells, this concern was dismissed.

Furthermore, I analysed the VSMC marker expression of the isolated mASMC. As the digested vessel also contained ECs and potentially cells of the basement membrane and adventitia, mASMC purity is necessarily tested. Flow cytometry analysis indicated a majority fraction of cells possessed

αSMA (83.5%), an early VSMC marker, Caplonin-h1 (63.3%), an intermediate VSMC marker, and SMMHC (78%), a mature VSMC marker (**Figure 3.9C**). These results indicate that the isolated primary cell population is representative of the target mASMC population.

Mouse aortic ECs (MAEC) were sometimes isolated alongside mASMC for the projects of other lab members. Aorta pieces would be cultured within Matrigel ECM which would induce angiogenesis of the MAECs. These MAECs would migrate out of the aorta piece and onto the culture surface, after which the aorta piece would be removed and processed to isolate mASMC (**Figure 3.9D**).

B **mASMC Protocol Parameters**

Mincing Time	Collagenase Digestion Time	Minimum Initial Seeding Density	Age of Mice	First Media Refreshment
~5 minutes	Over 1 Hour	2 Aortas per 6 Well Plate	Inconsequential	Inconsequential

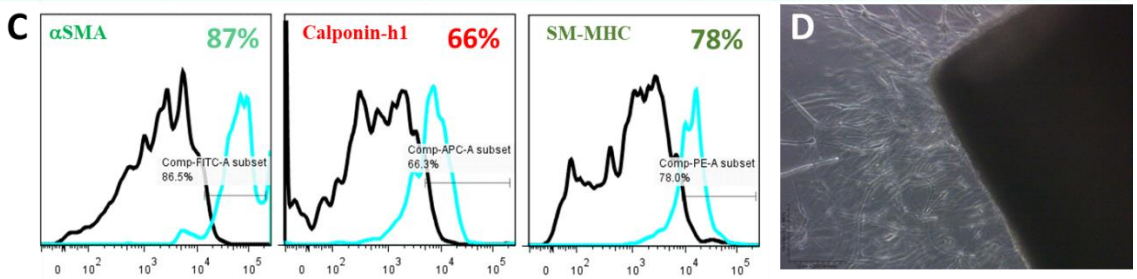

Figure 3.9 *Isolation, optimization, and analysis of primary mASMC.* ***A)*** *Protocol for isolation of mASMC. An aorta is surgically removed from a euthanized mouse and its adventitia is physically stripped. The aorta is then minced and digested in Collagenase II. The remains of the aorta are plated and maintained with smooth muscle media.* ***B)*** *Optimized protocol parameters for mASMC isolation. The crucial parameters for successful isolation involve digestion and initial seeding.* ***C)*** *Flow cytometry analysis of VSMC markers demonstrate that isolated populations are majority VSMC (N =1).* ***D)*** *MAECs undergoing angiogenesis from a section of a mouse aorta.*

Summary of Mouse Cell Optimization

Both A3 and R1 mESC were guided towards VSMC fate with FBS and atRA. The induction protocol was optimized for purity and yield with a variety of conditions. Results indicate that increasing atRA concentration yielded lower numbers of VSMC and that atRA concentration had

no effect on VSMC purity. However, earlier timescales, lower initial seeding densities, CIV or gelatin ECM are all conditions that increase VSMC purity.

Furthermore, mASMCs were isolated from mice to service as positive controls to compare with mESC-derived VSMC. Various conditions in the isolation protocol were optimized to procure viable and pure mASMCs.

However, each experiment was not repeated (N = 1) because the focus of my research pivoted towards the serum-free induction of human PSC towards VSMC fate. The lack of serum and use of human cells would make the protocol more clinically relevant and potentially more reproducible. Moreover, other lab members were moving their studies towards human cells and required human-induced VSMC to support their studies. Therefore, the mouse VSMC induction protocol was abandoned and replaced with optimization of a new protocol.

3.3.2 Optimization of Human Vascular Smooth Muscle Fate

Generation of KDR+ Vascular Progenitors

The protocol for generating this progenitor cell, which was optimized by other members of the McCloskey lab, involves inducing hiPSC for 10 days with 15 ng/mL of VEGF and 5 ng/mL of bFGF. Instead of serum, the base media uses the chemically defined Knockout Serum Replacement (KSR) (**Figure 3.10C**).

First, I ensured that the hiPSC I was using was properly maintained and pluripotent. Regular validation of hiPSC pluripotency showed that the hiPSC used had a mean Oct ¾ expression of 83% and a standard deviation of 16% (N = 4, data not shown).

Then, I ensured that I could repeatably preproduce the protocol for the generation of pure populations of KDR+ VPCs with human induced pluripotent stem cells (hiPSC). While KDR+ cells are known to be multipotent for VSMC [51], the earliest marker of VSMC recruitment in embryonic development is PDGFR-β [118]. To optimize for VSMC multipotency, I analyzed both PDGFR-β and KDR expression of the progenitor specification protocol at varying times (**Figure 2.10B**). Results indicate that the 10^{th} day of induction, the originally optimized time scale, yielded the highest percentage expression of PDGFR-β (N = 1, 36%) and nearly the highest percentage expression of KDR (77%). Across all time points, the majority of PDGFR-β+ cells coexpressed KDR (data not shown). Regular validation of the multipotency marker KDR on the 10^{th} day showed that on average, 88% of the induced progenitor population was KDR positive with a standard deviation of 5% (N = 10, data not shown).

As VSMC possess no cell type-specific surface marker, VSMC are difficult to purify. Therefore, I sought to purify the precursory KDR+ VPCs via FACS, which, in theory, should result in a higher final VSMC purity. Initially, the sorting process did not yield viable cells and required optimization. Sorting is a stressful process for the cells where the involved cells are passed through a pressured channel and exposed to potentially harmful shear forces. Furthermore, cells are exposed to cold temperatures during the staining process before sorting. Therefore, the protocol was necessarily included the use of a viability stain to prevent the sorting of nonviable cells (**Figure 2.10D**).

Moreover, sorted cells are treated with 5 µM Rho Kinase Inhibitor (ROCKI), an inhibitor of apoptosis, for 24 hours following the sort which greatly improves viability (**Figure 2.10E**). Sorting speed was also lowered, thereby reducing sorting pressure, but this parameter made no noticeable difference in viability (data not shown).

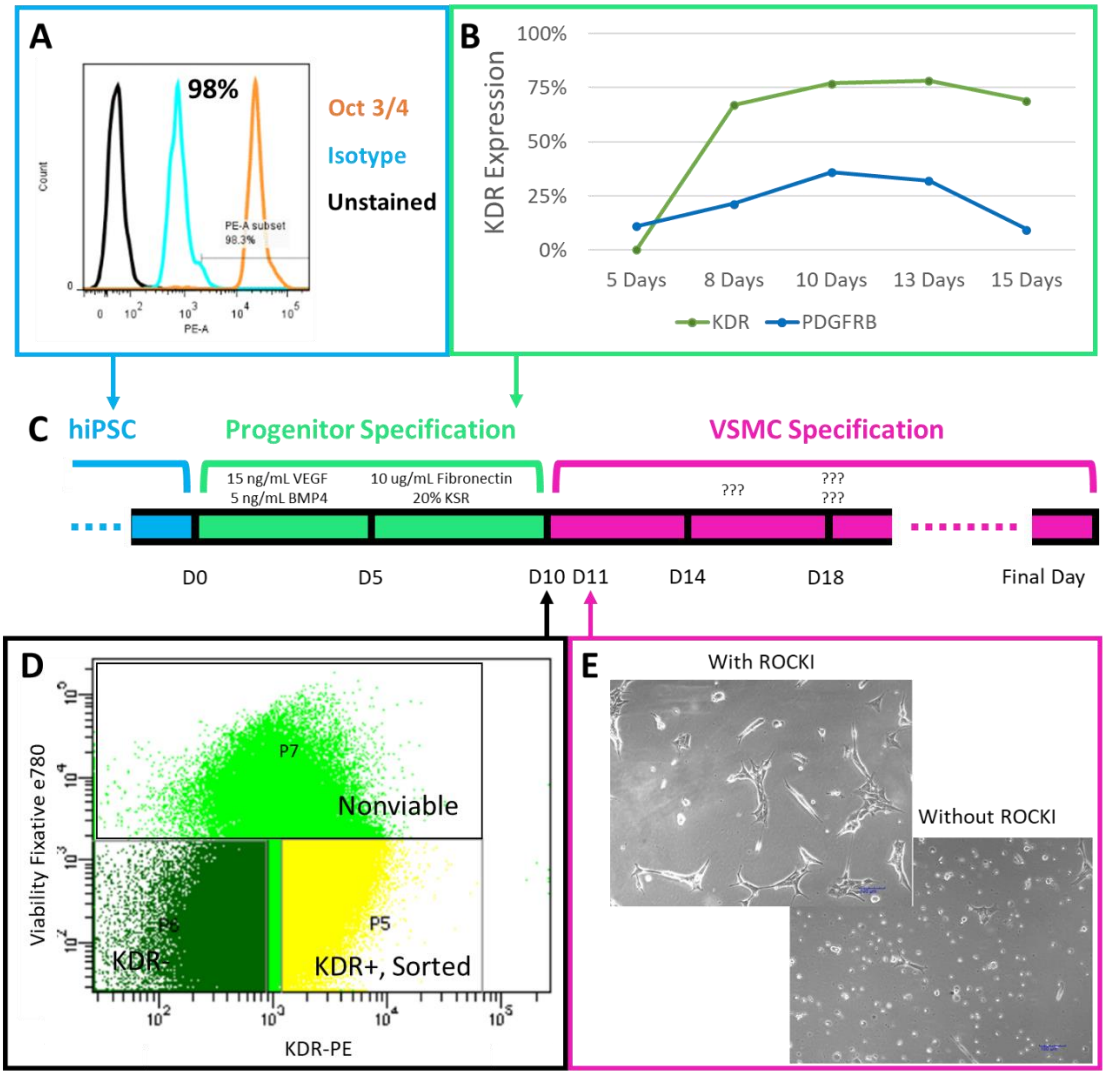

Figure 3.10 *Generation of KDR+ Vascular Progenitor Cells.* ***A)*** *Validation of the pluripotency of hiPSC.* ***B)*** *Analysis of the multipotency markers KDR and PDGFR-β over time during the progenitor specification step. Both markers peak at around the 10th day of progenitor specification (N = 1).* ***C)*** *Stepwise protocol for the generation of VSMC from hiPSC.* ***D)*** *Screenshot of the flow cytometry software, BD Diva, demonstrating gates for the sorted and unsorted populations.* ***E)*** *Phase contrast images of sorted KDR+ cells 24 hours after the sorting process with and without ROCKI supplementation. ROCKI supplementation keeps the cells viable where without ROCKI, the cells are nonviable.*

In sum, I was able to replicate the McCloskey lab's protocol for generating vascular progenitors with high efficiency. I also analyzed the PDGFR-β expression, an indicator of VSMC multipotency, in the resulting progenitor and concluded that the protocol generates a significant fraction of VSMC progenitors. I also optimized the KDR sorting protocol for viability.

However, the sorting process was eventually removed from the protocol in favor of typical passaging. While the sorting process produced viable cells, it greatly reduced the yield of progenitors. Furthermore, it greatly increased the cost and effort required for progenitor specification and introduced new points of failure. Moreover, the sorting process was deemed unnecessary as the purity of KDR+ progenitors was consistently high (mean 88%, stddev 5%, N = 10). Also, the reliance of the sorting process on ROCKI could potentially affect VSMC specification as Rho Kinase is known to play a significant role in VSMC differentiation via sphingolipids [211].

Nonspecificity in Smooth Muscle Marker Antibodies

After KDR+ vascular progenitor specification, the stem cells are optimized for VSMC marker expression with different media formulations. I conducted experiments to determine the effects of serum replacements, growth factor concentrations, ECM types, and timescales on VSMC fate. However, the majority of anti-VSMC marker antibodies used was defective in the context of the experiment. They either did not react with a primary VSMC positive control or they reacted with a non-VSMC negative control, even compared to isotype controls.

This antibody nonspecificity issue resulted in years of inconsistent results. The worst of which occurred during an induction with KDR+ cells taken to different time points using base media supplemented with varying concentrations of PDGF-ββ (**Figure 3.11**). All 30 data points yielded disagreeing values of αSMA, Calponin-h1, and SMMHC expression. Where all three markers should simultaneously upregulate or remain negative, Calponin was expressed very highly whereas αSMA and SMMHC were negative.

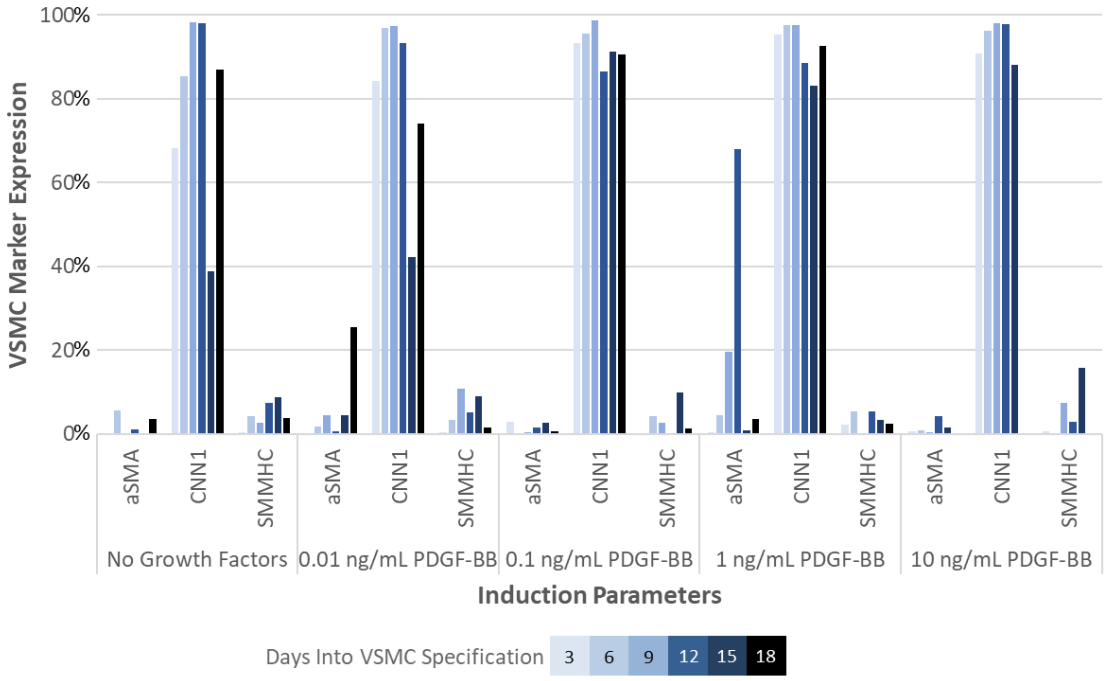

Figure 3.11 *VSMC marker expression with varying time and PDGF-ββ concentration during VSMC specification of VPC. Calponin is high expressed which disagrees with the low expression of αSMA and SMMHC.*

Chapter 4 details rigorous validations of 7 VSMC marker antibodies in response these analysis issues. A SMMHC antibody (eBioscience 53-6400-82 at 1:200 titration) was determined to be able to identify its intended epitope most accurately and will be used for the remainder of this chapter.

From KDR+ Vascular Progenitor to VSMC

Unsorted KDR+ progenitor cells were directed towards VSMC fate with 10 ng/mL PDGF- ββ and 3.5 ng/mL TGF-β1 with different timescales, soluble signals, and ECM (**Figure 3.12A**). Initial results were promising, yielding up to 70% SMMHC expression. It also indicated that LN and CIV were more conducive towards VSMC fate. Furthermore, SMMHC expression peaked at day 12, the later timepoint, which is in line with the knowledge that SMMHC is a late stage marker [185–187].

However, these initial results (N = 1) were not repeatable (**Figure 3.12B**). The next 4 attempts consistently produced SMMHC expressions below 20%. In addition, many samples were lost due to nonadherence issues despite attempts to debug with different initial seeding densities (**Figure 3.12C**), taking the induction to 20 days, and the use of either TrypLE (Fisher), Accutase (Corning), or Trypsin (Corning) as lifting reagents (data not shown). It was eventually discovered that only

~30% of the progenitor population was expressing KDR instead of the ~90% that the protocol was optimized at. Further debugging experiments could not be conducted due to time constraints. The fact that each induction takes over a month, years was spent for faulty data with bad antibodies, and the outbreak of COVID-19 halted further research activities.

Although the marker expression could not be validated, the hiPSC-derived populations were introduced to microfluidic devices as support cells for vasculogenesis. Briefly, human umbilical vein endothelial cells (HUVEC) and support cells, typically fibroblasts, VSMC, or PC, are seeded in a microfluidic channel(s) containing crosslinked fibrinogen. Media is diffused into this ECM-dense compartment via adjacent channels [212]. Two other graduate students, Lian Wong and Jose Zamora, were each provided presumed hiPSC-derived VSMC as support cells and conducted independent experiments 2 years apart. Both graduate students were able to leverage the hiPSC-derived population to induce network formation in the HUVECs (**Figure 3.12E&F)**. This demonstrates that the hiPSC-derived populations behaved as perivascular populations do in the context of vasculogenesis.

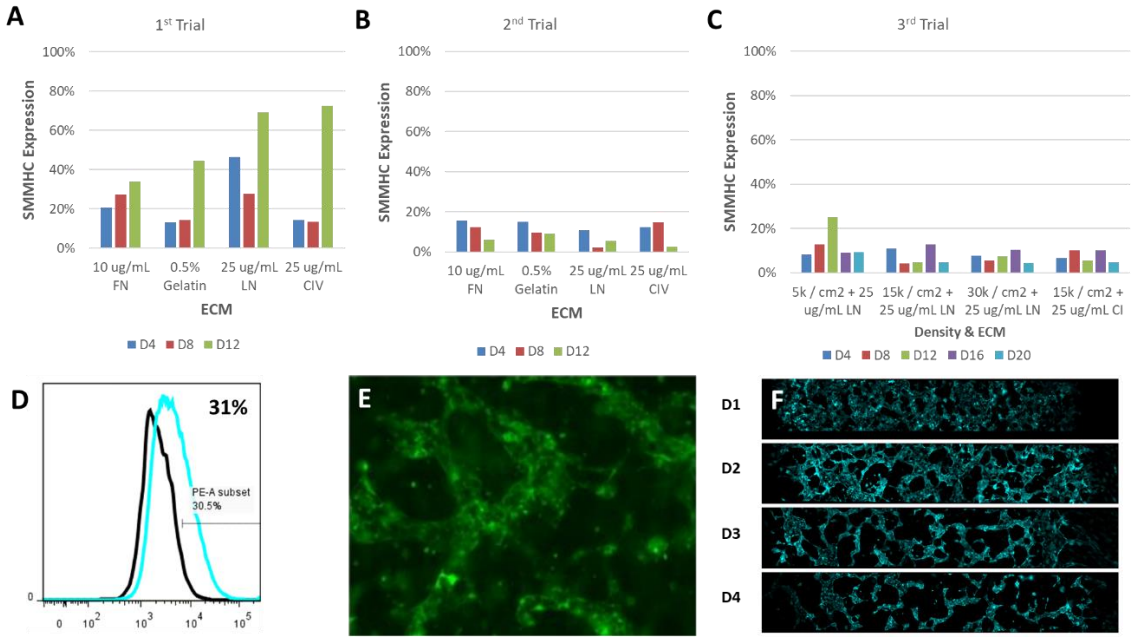

Figure 3.12 *Marker and functional analysis of hiPSC-derived VSMC.* ***A)*** *Time and ECM were varied and SMMHC expression was analysis.* ***B)*** *Repeating the same experiment yielded different results.* ***C)*** *Attempts to debug the issue by varying seeding density did not alleviate lower expression levels.* ***D)*** *KDR expression of progenitor cells during VSMC induction debugging.* ***E-F)*** *hiPSC-derived VSMC promoting vasculogenesis of GFP or CellTracker labelled HUVECs courtesy of* ***E)*** *Lian Wong and* ***F)*** *Jose Zamora.*

3.4 Conclusion

mESC were guided towards VSMC fate with a serum-based atRA induction model while hiPSC were guided towards VSMC fate with a serum-free, multistage induction model. Mouse atRA induction results indicated that CIV and gelatin as well as low seeding densities were more conducive for a purified mESC-derived VSMC population. While the first stage of hiPSC induction of KDR+ vascular progenitors was very successful, VSMC specification was hindered by faulty commercially available antibodies. However, the limited analysis of hiPSC-derived VSMC indicated that the protocol could, albeit inconsistently, produce a VSMC population expressing a late stage marker SMMHC. Based on SMMHC expression only, CIV and LN as well as a 12+ day induction time is preferred for VSMC fate. Furthermore, this population was able to promote vasculogenesis in HUVECs, which is in line with the function of native mural cells.

Chapter 4: Inadequate Antibodies for Vascular Smooth Muscle Cell Characterization

Abstract

Flow cytometry, paired with fluorescent antibodies, is a common method for characterizing cell phenotypes. However, many commercially available antibodies can be unreliable and validating such antibodies is becoming increasingly important. Our laboratory is interested in deriving and characterizing vascular smooth muscle cells from embryonic and induced pluripotent stem cells. However, most of the commercially available antibodies examined were found to be problematic. Attempts to resolve the issues included exploring a range of incubation times, blocking reagents, staining kits, and titrating dilutions against both positive and negative control cells. In the end, I found that only the smooth muscle myosin heavy chain (SMMHC) antibody at one titrating dilution could clearly distinguish between positive and negative controls. Moreover, without adequate antibodies for labelling smooth muscle cells, I was not able to continue with my studies on smooth muscle cell fate.

4.1 Introduction

Flow cytometry is a popular and powerful tool for the characterization of cells. Specifically, flow cytometry enables high-throughput, single cell quantification of size, granularity, and multiple fluorescent reporters [213,214]. Paired with antibodies that mark specific epitopes with reporters, flow cytometry allows researchers to identify and sort phenotypes with distinct marker profiles within a larger cell population. As such, flow cytometry has been used in the characterization and isolation of many heterogeneous cell [215–217] and stem cell-derived populations [23,218,219].

Critical to the accurate measurement of epitope presence is the optimization of antibody staining parameters. Because cells exhibit autofluorescence and antibodies exhibit non-specific binding, signal-to-noise ratio must be optimized for each experiment. Typically, antibody concentrations need to be titrated to maximize signal for positive control samples relative to the background signal [220]. Negative control samples, and sometimes isotype controls, are used to exclude the possibility of non-specificity [221]. Nonspecific binding can be further mitigated with the introduction of blocking reagents that compete for nonspecific binding sites [222,223]. For example, Fc receptors found on many cells bind antibodies via their constant Fc domain rather than the antigen specific Fab domain, leading to false positives and meaningless data. In order to prevent this type of binding, Fc blocking immunoglobulin from the matching species can ensure that only antigen specific binding is observed [223]. Serum is another regularly used blocking reagent but potentially contains lower levels of immunoglobulin compared with Fc blocking immunoglobulin.

However, despite these best practices, commercial antibodies have been reported to be unreliable, nonspecific, or completely dysfunctional [224–227]. Berglund et. al validated over 5,000 commercially available antibodies with immunohistochemistry and Western blot experiments and found that approximately half were defective [228]. Other studies have detailed the frustrations and wasted resources of researchers who have stumbled upon faulty reagents [229,230]. This has led to the need that antibodies be rigorously validated before their results can be trusted [231,232].

Our laboratory is most interested in vascular and cardiovascular stem cell differentiation, including studies on vascular smooth muscle fate from vascular progenitor cells. The most common markers for identifying VSMC are intracellular contractile markers with no cell surface markers available for vascular smooth muscle cell identification for live cell sorting. During embryonic development, nascent VSMC first express the early marker alpha smooth muscle actin (αSMA) [118] and later, the intermediate marker calponin-h1 [179,180]. However, αSMA is also expressed in myofibroblasts [192] and both αSMA and calponin-h1 are expressed in early cardiomyocytes and skeletal muscles [193,195]. More specific, mature markers include the smooth muscle myosin heavy chain (SMMHC) [182] and smoothelin-B (SMTNB) [200], and of these markers, only smoothelin-B distinguishes vascular smooth muscle from visceral smooth muscle.

Here, I report my findings on a variety of antibodies advertised for characterization of vascular smooth muscle cells (VSMC). I perform flow cytometry tests on each antibody using primary human aortic smooth muscle cells (HAoSMC) as the positive control and non-VSMC types thought to be negative for VMSC marker expression. I used two different commercially available intracellular staining kits and tested the effects of blocking and stain time on signal quality. Each antibody was titrated with the positive and two negative controls. My studies indicate that out of the eight antibodies tested, only one antibody was could confidently distinguish between positive and negative controls, and only at a specific concentration.

4.2 Materials & Methods

4.2.1 Cell Sources

HAoSMC (Lonza) were used as positive controls for the anti-SMC marker antibodies. Negative controls consisted of human umbilical vein endothelial cells (HUVEC, Lonza), human induced pluripotent stem cells (hiPSC, WiCell), as well as Jiyoye, Jukrat, K562, and U937 cells (donated from Escape Therapeutics). HAoSMCs were expanded in SmGM-2 BulletKit (Lonza), HUVECs were expanded in EGM-2 BulletKit (Lonza), and hiPSC were expanded on hESC-certified Matrigel (Corning) in mTeSR1 (STEMCELL Technologies).

4.2.2 Staining Protocol

Cells were fixed and stained immediately after thawing from cryopreservation. Fixation and staining methods followed the manufacturer protocol of each staining kit (eBioscience Foxp3 Staining Kit and Biolegend Transcription Factor Buffer Set). Unless otherwise stated that cells were analyzed with Viability Fixative e780, cells were fixed for 10-15 minutes, blocked with either 0.5% Human Fc Block (Biolegend) or 2% FBS (Corning) for 30-60 minutes, stained overnight at 4°C, and if applicable, stained with secondary antibodies for 30 minutes at 4°C. All primary samples are matched to a corresponding isotype and unstained sample. All isotype and secondary antibodies are used at the same IgG concentration. All samples were processed at 100,000 cells per 100 µL. **Table 4.1** details the catalog numbers of each primary antibody, matching isotype controls, and secondary antibodies. Of the 8 antibodies, 6 are advertised to be applicable for flow cytometry. Viability Fixative e780 (eBioscience) was used at 1:1000 concentration.

Table 4.1 *Antibody list with vendor and catalog numbers, matching isotype, and secondary antibodies used in this study.*

Intended Epitope	Primary	Isotype Control	Secondary
αSMA	Sigma F3777	Biolegend 400210	
Calponin-h1	Sigma C2687	R&D MAB002	Abcam ab6816
SMMHC	Sigma M7786	R&D MAB002	Abcam ab6816
SMMHC	Santa Cruz sc-6956	Santa Cruz sc-2866	
Smoothelin-B	R&D MAB8278	R&D MAB002	Abcam ab6816
Calponin-h1	Invitrogen MA5-11620	Invitrogen MG128	Invitrogen P30013 (Conjugation Kit)
αSMA	eBioscience 50-9760-82	eBioscience 50-4724-80	
SMMHC	eBioscience 53-6400-82	eBioscience 50-4717-80	

4.2.3 Flow Cytometry and Data Analysis

Cells were analyzed on a LSR II flow cytometer (BD Bioscience) and data was processed on FlowJo (FlowJo). Datapoints with very low forward scatter (FSC) and side scatter (SSC) were gated out to exclude debris and very high forward scatter (FSC) were gated out to exclude doublets. Signals from the stain were gated at starting above the last 5% of the isotype signal. Samples with highly irregular data (i.e. fluorescent intensities lower than unstained controls) were omitted.

4.3 Results & Discussion

My original intent was to debug the issues related to staining my hiPSC-derived VSMC. Therefore, I tested antibodies for specificity by validating antibodies against HAoSMCs, which should be positive for all VSMC markers, as well as hiPSCs, HUVECs, and several blood cell lineages, which should be negative.

I began by testing the effects of primary antibody incubation time (**Figure 4.1A-C**) on three antibodies, anti-αSMA (eBioscience), anti-caplonin-h1 (Invitrogen), and anti-SMMHC (eBioscience). I compared the 30 minute incubation time recommended by the Foxp3 staining kit manufacturer for intracellular staining against an overnight incubation. While the overnight incubation increased an otherwise low detection signal from all three antibodies used to stain the HAoSMC positive controls, it also undesireably increased the signals from the two negative controls. I decided to use the overnight incubation in proceeding experiments since it was able to raise the overall expression levels of the positive cell type.

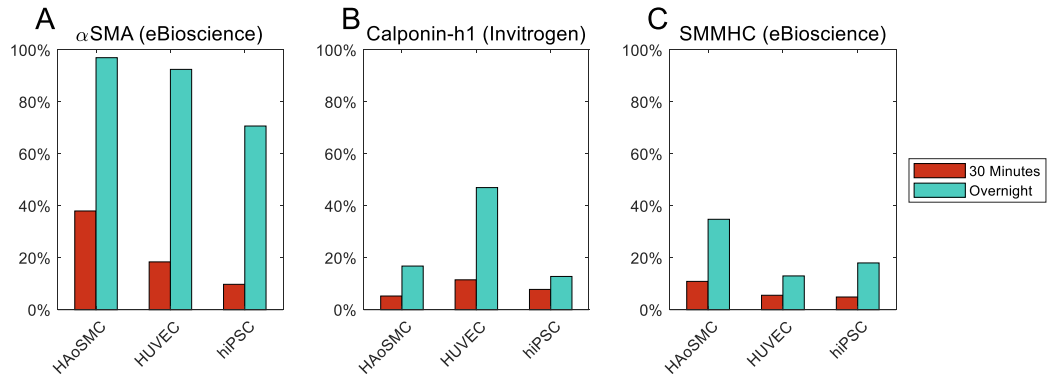

Figure 4.1 *The effects of incubation time on VSMC marker staining. Here, we stained HAoSMCs as the positive control and cell types, HUVECs and hiPSCs, as negative controls. A) The effects of incubation time of αSMA (eBioscience) antibody. B) The effects of incubation time of Calponin-h1 (Invitrogen) antibody. C) The effects of incubation time of SMMHC (eBioscience) antibody. Staining was conducted at 1:100 concentrations using the Foxp3 staining kit with no blocking.*

I then examined the effects of a few different blocking buffers on the signal quality of the poorest performing antibody, αSMA (eBioscience, **Figure 4.2A**), and its corresponding isotype control.

Blocking with either 0.5% Human Fc Block (Biolegend) or 2% FBS (Corning) yielded no change in signal compared to unblocked samples.

HUVECs have been reported to transdifferentiate into myoblast or VSMC-like phenotypes under certain conditions [233–235]. And hiPSC, being pluripotent, can differentiate into any cell type in the body. Under these circumstances, VSMC markers could possibly be expressed on hiPSC and HUVEC negative controls Therefore, I additionally tested Jurkat T-cells, K562 bone marrow cells, and U937 macrophages as three additional negative cell lines and found the same high level of nonspecific binding from αSMA (eBioscience), calponin-h1 (Invitrogen), and to a lesser extent, SMMHC (eBioscience) antibodies (**Figure 4.2B**).

Protocols often mention that dead cells can cause significant background signal via autofluorescence, so I tested the marker expression in conjuncation with Viability Fixative (VF). Marker expression was compared between VF+ (dead), VF- (live), and whole populations (**Figure 4.2C**). While VF+ populations had marginally higher expression, it was not at a level that could account for the high amount of nonspecificty shown in this study.

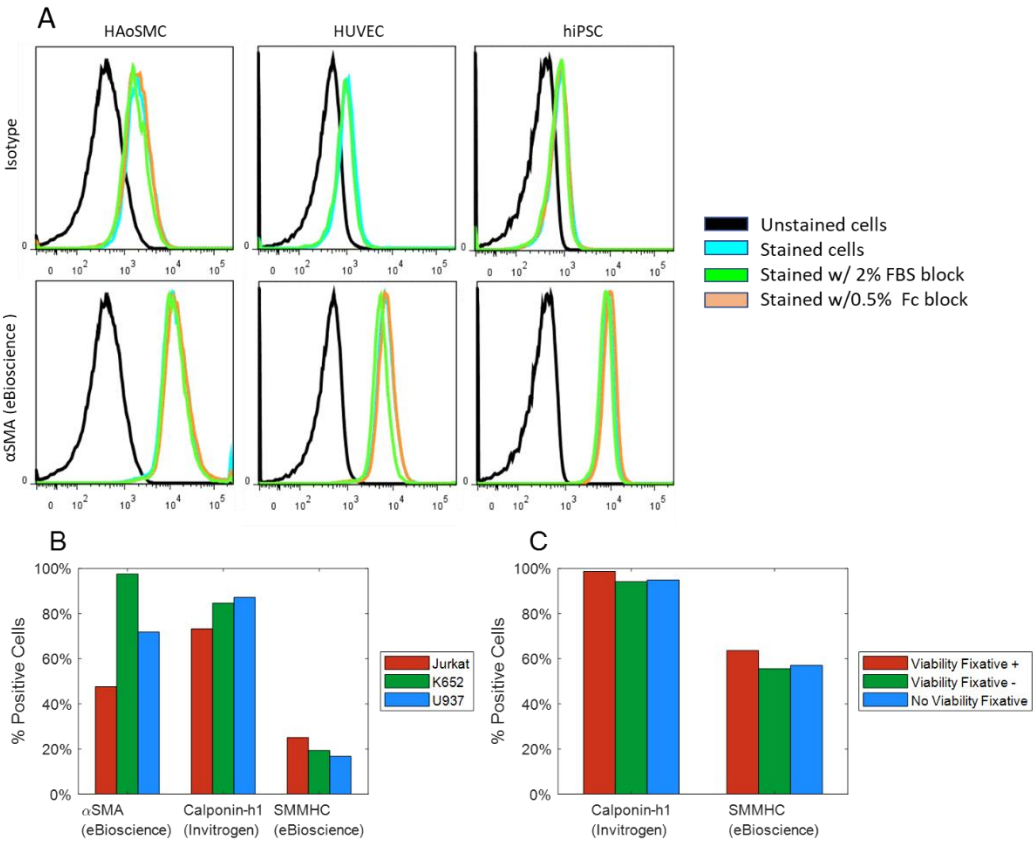

Figure 4.2 *A) The effect of blocking reagents on a-SMA antibody (eBioscience) staining positive HAoSMCs and two negative cell types, HUVECs and hiPSCs. Cells stained with the primary antibody or isotype control and blocked for 30 minutes before staining with either 2% FBS or 0.5% human FC receptor block. Staining was conducted at 1:100 concentrations using the Foxp3 staining kit. E) Three different VSMC marker antibodies αSMA (eBioscience), calponin-h1*

(Invitrogen), and SMMHC (eBioscience) were also examined on Jukat T-cells, K562 bone marrow cells, and U937 macrophages as negative controls. Cells were blocked with 2% FBS before overnight incubation at 1:100 concentrations with the Foxp3 kit. C) hiPSC were stained with the Transcription Buffer Staining Kit using 1:200 Calponin (Invitrogen) and 1:100 SMMHC (eBioscience) in conjunction with Viability Fixative e780. Marker expression is analyzed on populations that are Viability Fixative positive, negative, or without viability gating.

Next, I performed titrations on each of the three antibodies against both positive and negative controls with two different staining kits: eBioscience Foxp3 Staining Kit and the BD Transcription Factor Buffer Set (**Figure 4.3**). Primary and isotype antibodies exhibited typical of titrationing dose responses where higher concentrations of staining material led to increased numbers of cell expressing a fluorescence signal.Among all three antibodies and both kits, only the SMMHC antibody (eBioscience) was able to distinguish correctly between positive and negative controls, however the window in which the antibody exhibited the correct staining was very small, only at the 1:200 concentration (**Figure 4.3C&F**). However, the SMMHC antibody exhibited this same consistency across both labeling kits, but reported large differences in the % positive cells with 80% reported from the BD Transcription Factor Buffer Set and only 55% positive from the eBioscience Foxp3 Staining Kit. Moreover, both the calponin-h1 and αSMA antibodies report more positive expressing cells in the negative controls compared to the positive control cells across almost all titrating dilutions.

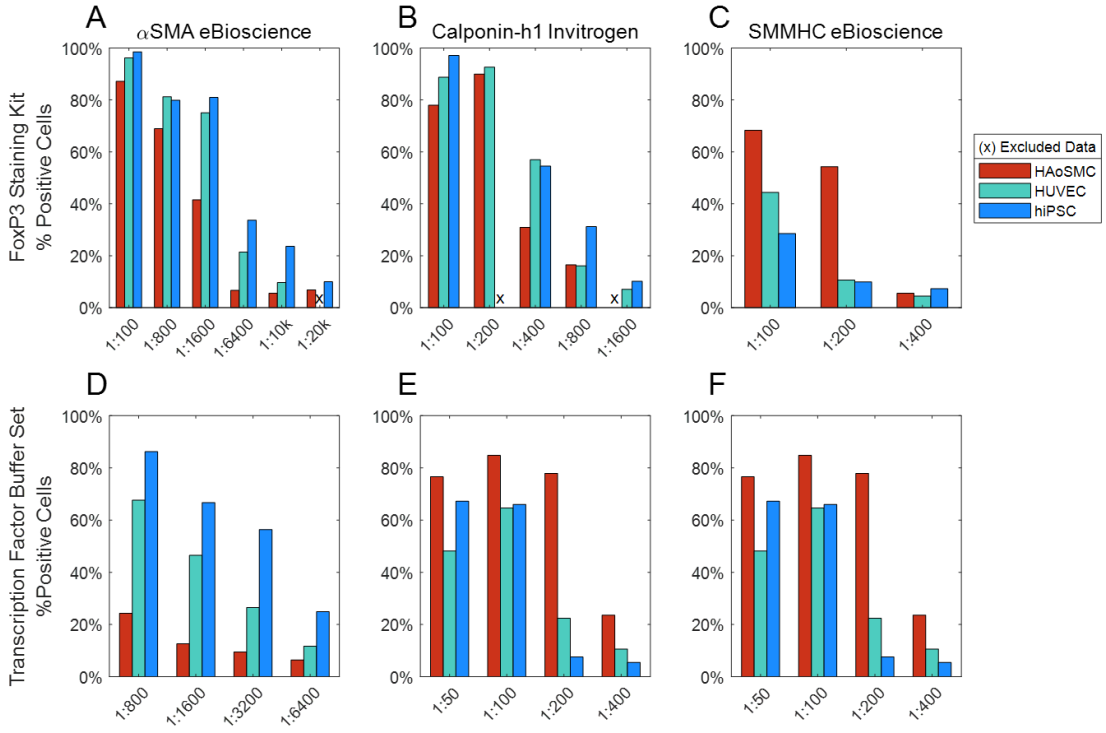

Figure 4.3 *Percent VSMC Marker Expression vs. Staining Protocol and Titration. Antibodies were titrated against positive (HAoSMC) and negative (HUVEC and hiPSC) controls with* ***A-C)*** *Foxp3*

*staining kit with 2% FBS as the blocking buffer or **D-F)** Transcription Factor Set with 0.5% Human Fc Block.*

I proceeded with the use of the Foxp3 kit to titrate 5 additional SMC antibodies (**Figure 4.4**). The two additional SMMHC antibodies (Santa Cruz **Figure 4.4A** and Sigma **Figure 4.4B**) examined expressed low signal on positive controls compared to the negative control cells. I also titrated anti-SMMHC (Santa Cruz) at a higher concentration (1:5-1:50), but that only exacerbated the issue (**Figure 4.4A**). Additionally, neither smoothelin-B (R&D **Figure 4.4C**) nor αSMA (Sigma **Figure 4.4D**) could distinguish between positive and negative controls at any titrating dilution. Only calponin-h1 (Sigma **Figure 4.4E**) at 1:400 was able to distinguish between positive and negative cell controls. However, the negative controls' expression was still too high, reporting 21% and 39% for HUVECs and hiPSCs, respecitvely. Although Cheung et al. were able to distinguish between their stem cell-derived VSMCs from PSC and HUVEC negative controls, using 1:500 αSMA (Sigma), 1:30,000 calponon-h1 (Sigma), and 1:500 SMMHC (Sigma) antibodies using the BD Cytofix kit [12],their results were published in 2012, and likely used a different batch of antibodies.

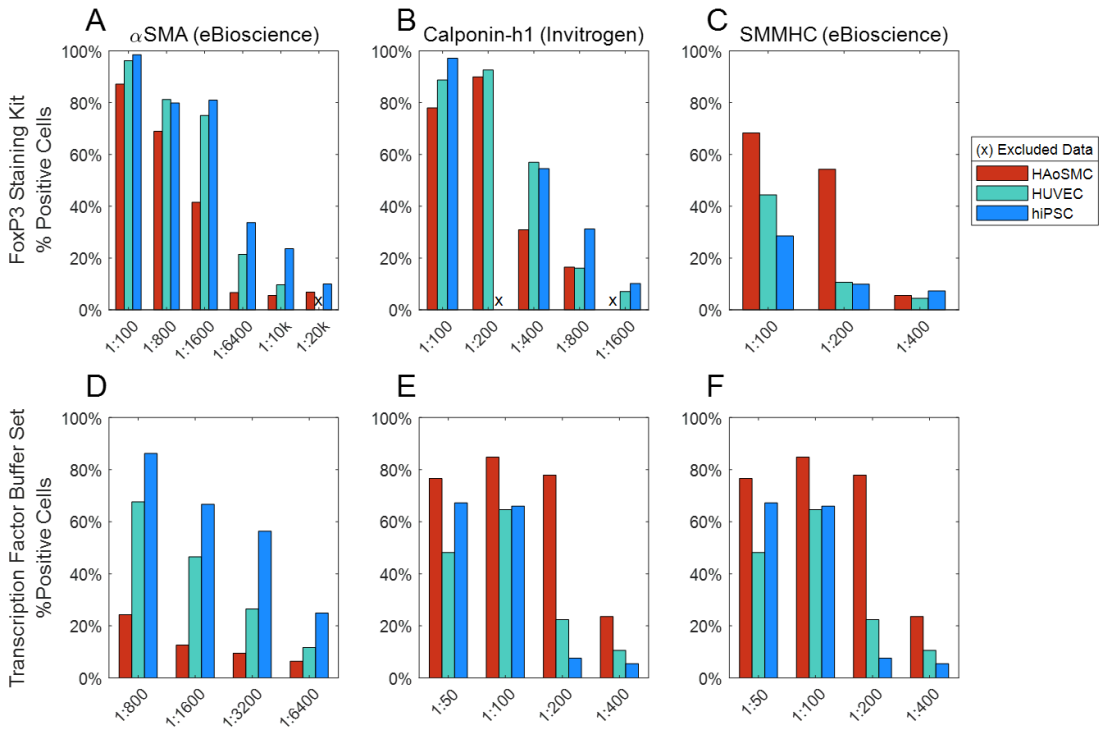

***Figure 4.4** Percent VSMC Marker Expression vs. Titration. Dilution for SMMHC antibody from A) Santa Cruz, B) Sigma, C) smoothelin-B from R&D, D) aSMA from Sigma, and E) calponin-h1 from Sigma. All antibodies were titrated against positive and negative controls with Foxp3 staining kit. B, D, and E were not blocked. A and C were blocked with 2% FBS and 2% Human Fc for 30 minutes.*

4.4 Conclusions

In summary, the SMMHC antibody (eBioscience) exhibited the best signal, though only at the 1:200 concentration (**Figure 4.3C&F**). Calponin-h1 (Sigma) also exhibited a positive signal on the positive control cells, but the signal on negative controls was still too high to use this antibody with confidence (**Figure 4.4E**). Based on these results, I recommend that researchers not only titrate antibodies for maximum signal, but also titrate positive and negative cell controls. Many blocking buffers do not necessarily mitigate nonspecific binding and cannot be relied upon without further investigation, and incubation time and different staining protocols and kits can have a noticeable impact on the signal output of antibodies and should be considered during antibody evaluation and optimization. Unfortunately for my work on deriving SMCs from hiPSCs, the one low-expessing antibody that I find acceptable to use is not enough to proceed with SMC characterization. I have still not found enough antibodies that I can use confidently in my studies evaluating SMC fate.

Chapter 5: Bioprinting Concentration Gradients for Guided Vascularization

Abstract

Vascularization has long remained a hurdle in producing artificial thick tissue. While other tissue engineering techniques have great success producing microvasculature network formation, few bioprinting studies have created similar networks. Here, we draw inspiration from microfluidic protocols to produce a bioprinted construct conducive to vascular network formation. Our optimized alginate/fibrinogen hydrogel was able to coax human umbilical vein endothelial cells (HUVEC) cocultured with normal human lung fibroblasts (NHLF) to produce networks after 5 days and retain these networks for over a month. The hybrid hydrogel was also able to retain a printed VEGF gradient for at least 2 days. Furthermore, we assessed the different network formation outcomes with use of different combinations of accessory cells (smooth muscle and pericytes). The addition of printed VEGF gradients to these constructs causes the vascular cells to aggregate to (what is presumed) the high end of the gradient.

Chapter 5 was completed in collaboration with graduate student Maria Mendoza who performed all the cell culture, imaging and data analysis of live cells, as well as the printing and material preparation alongside me.

5.1 Introduction

The field of regenerative medicine has long been limited by the constraints of vascularization [38]. Thick tissues, no matter the method of generation, are subject to the 100-200 μm of oxygen diffusion and require perfusable vasculature to supply nutrients [39,40]. Native vasculature achieves this with large diameter, contractile arteries that progressively branch into small diameter, diffusive capillaries. Vessels of all sizes consist of an endothelial cell (EC) lumen surrounded by a host of perivascular cells. The larger arteries possess a thin basement membrane containing pericytes (PC), a thick tunica media containing vascular smooth muscle (VSMC), and an adventitia with fibroblasts. Meanwhile, smaller capillaries typically consist of just the EC lumen with a very sparse layer of PC [70].

To fully recapitulate native vasculature, artificial thick tissue must necessarily be complex, multicellular constructs that integrate multiple vascular cell types with other cells. The current paradigm is to interlace large vasculature (>100 μm diameter) with tissue via engineered patterning methods [16,41,42]. Meanwhile, capillaries that are smaller than the resolution of engineering techniques should self-assemble or sprout from the large diameter vessels [43–45]. Incorporation of these requirements in a scalable manner is the holy grail of vascularization in regenerative medicine.

Concentration gradients of growth factors are a crucial regulator of the assembly and regeneration process in all tissue. These gradients are well known for guiding cell migration and the reorganization of tissue [71]. The presence of natural ECMs provide heparin sulfate proteoglycans (HSPG) that bind to growth factors, enabling HSPG to modulate the diffusion of growth factors through the microenvironment [236,237]. Vascular endothelial growth factor (VEGF) is one such small molecule that is a key promoter of vessel formation where concentration gradients of VEGF are known to control sprouting [72]. Interactions between VEGF and fibrin have been known to elicit unique responses from EC [238]. Recapitulating gradients can therefore be a valuable tissue engineering technique for recreating the complexities of native tissue.

Bioprinting is a regenerative technique that has gained enormous traction for its promise of creating organ-like tissue [33]. However, these tissues are subject to the same vascularization limitations, necessitating vascularization techniques to be incorporated into bioprinting [239]. Most vascularization strategies in bioprinting involves the fabrication of large diameter vessels with techniques such as coaxial extrusion [240–242], fugitive bioinks [16,243], or simply printing hollow structures [41,244]. Thereafter, EC can be locally seeded, and perfused nutrients can be diffused to the lumen surroundings. But due to a limited resolutions and inability to manipulate the microenvironment, the field of bioprinting has struggled to induce small diameter network formation [245]. Furthermore, current bioprinting techniques have a limited ability to manipulate the microenvironment. In terms of microscale complexity, bioprinters only produce 3D environments that are sometimes embedded with a uniform distribution of growth factors. This results in a rather undirected tissue assembly process.

Meanwhile, organ-on-a-chip microfluidic devices have had success recreating perfusable vascular networks in vitro [246,247]. Contrary to bioprinting, microfluidic devices can be fabricated with high resolutions and compartmentalize fluids for precise control of cell microenvironments [30]. This enables vessel-on-a-chip designs where EC are seeded into a 3D environment with fibrin and

accessory cells that secrete soluble signals or initiate cell-cell contact signaling to promote vessel formation [45]. Adjacent channels allow media to diffuse into the dense, cell-laden hydrogel. Key to this network formation are accessory cells such as mural cells, fibroblasts, and stem cells, which are known to have significant effects on EC functions and vessel formation in vivo [248]. This compartmentalization also allows microfluidic devices to generate concentration gradients of small molecules [32]. Microfluidics studies have recapitulated VEGF gradients to direct the sprouting and vessel formation process [249–251]. Yet despite these advantages, vascularization and microenvironment complexity, vessel-on-a-chip designs are not suited for recreating organs as they are not conducive to the organ level scales and geometries that bioprinting can achieve.

Here, we draw inspiration from vessel-on-a-chip designs and incorporate VEGF-guided EC network formation into bioprinting while retaining bioprinting's flexibility and scalability. We optimized the composition of a hybrid alginate/fibrinogen bioink that was conducive to network formation as well as the printability, crosslinking, and mechanical stability requirements of bioprinting. We then quantified the concentration of entrapped gradients with a standard curve. Finally, we entrapped a VEGF gradient in our hydrogel and observed the effects of the gradient on seeded vascular cells.

5.2 Materials & Methods

5.2.1 Preparation of Hydrogel

Alginate solution, 2% (w/v), was prepared by gently stirring alginic acid powder (Sigma 180947) with phosphate buffered saline (PBS) at 65°C. Fibrinogen solution (Sigma F8630), 10 mg/mL, was dissolved in PBS at 40°C for 3 hours. The 2% alginate and 10 mg/mL fibrinogen solutions were well mixed at a 1:1 ratio to form our bioink. 2% RGD-linked alginate (NovaMatrix VLVG GRGDSP) was used as is. To visualize the material, food coloring is sometimes suspended within the solubilized hydrogels.

5.2.2 Preparation of FRESH Support Bath

All prints in this study used the freeform reversible embedding of suspended hydrogels (FRESH) gelatin support bath which was created according to the protocols of Hinton et al. [15] 4.5% (w/v) gelatin solution was created by gently stirring gelatin powder (Difco) with 11 mM CaCl2 (Sigma) and 0.1 U/mL thrombin (Sigma) in deionized water at 65°C. 30% of a 16 ounce mason jar was filled with the gelatin solution and solidified at 4°C overnight. The resulting gelatin puck was separated from its container and the mason jar was filled with 11mM CaCl2 solution before chilling at -20°C for ~40 minutes. The chilled contents of the mason jar were blended in an Oster Beehive blender (Oster) for 2 minutes. The resulting gelatin particle solution was centrifuged at -5°C at 3000G for 4 minutes. The supernatant was aspirated, and the gelatin particles were washed once with 11 mM CaCl2. The modification to the original protocol is that the support bath is cooled at 4°C for 24 hours before plating. Plated support baths are centrifuged at 1500G to evenly distribute the gelatin particles across the plate.

5.2.3 Bioprinting Process

All bioprinting was done with our lab's custom bioprinter, ModiPrint, which was described in detail in Chapter 2.

Print sequences were programmed with handwritten commands in the form of modified g-code. ModiPrint's control software converts these commands into a custom language that is streamed to the firmware. All print geometries in this study were single-filament thick constructs printed in a grid pattern.

All extrusion used a 100 μm inner diameter chamfered nozzle (Nordson EFD) with 2000 mm/s^2 acceleration, 0.01 junction deviation, and a 250 μm pitch. 2% Alginate was printed at 12 mm/s print speeds at 5 psi. 0.5% Alginate hybrid hydrogels were printed at 25 mm/s print speeds with 3 psi. All drop-on-demand printing used a 100 μm inner diameter nozzle (The Lee Co.). All gradients used a 2 mm interpolate distance, 80 μs initial opening time, point geometries, exponential gradients, and 500 μm pitch. Live cell prints and FITC-Dextran prints used 45% gradient strength with 200 ng/mL of VEGF whereas fluorescent VEGF prints used 95% with 2 ug/mL of VEGF.

All prints were performed at room temperature with a 4°C. FRESH support bath. The petri dish containing the support bath is secured to the print surface. The print sequence begins immediately after the nozzle moves to starting position. Embedded constructs were placed in a 37°C incubator until the support bath was fully dissolved. Dissolved baths are aspirated, and printed constructs are washed with PBS before culture or analysis.

To achieve sterile prints, the bioprinter was moved inside a laminar flow biosafety cabinet. The bioprinter was exposed to UV light for 5 minutes before being thoroughly wiped with 70% ethanol. All syringe and nozzle components directly in contact with the hydrogel and cells were autoclaved. A HEPA filter was installed upstream of the syringe barrel and all pneumatic circuitry downstream of the HEPA filter was autoclaved.

5.2.4 Cell and Tissue Culture

GFP-expressing human umbilical vein endothelial cells (HUVECs, Angio-Proteomie) were expanded in EGM-2 with Bulletkit (Lonza), normal human lung fibroblasts (NHLFs, Lonza) were expanded in FGM2 (Lonza), human aortic smooth muscle cells (HAoSMCs, Lonza) were expanded in SmGM2 (Lonza), and RFP-expressing pericytes (PC, Angio-Proteomie) were expanded in Pericyte Growth Medium (Angio-Proteomie), according to manufacturer protocols. Cells were printed either directly after passage or from cryopreservation.

Following printing, tissue constructs are maintained in equal parts media of each respective cell type and media is refreshed every 3 days. Media was supplemented with 1% Antibiotic-Antimycotic (Gibco) for the first 3 days.

Cocultures were printed with a 2:1 ratio of HUVECs and NHLFs at a 3 million cells / mL seeding density. Tricultures were printed with a 10:10:1 ratio of HUVECs, NHLFs, and HAoSMCs at 8 million cells/mL. Tetracultures were printed at a 10:5:5:1 ratio of HUVECs, NHLFs, HAoSMCs, and PCs at 8 million cells/mL.

5.2.5 Cell Imaging

Fluorescent images were taken with an epifluorescence microscope (Nikon TEU-2000) and NIS Elements AR 3.2. Images were processed with ImageJ.

5.2.6 FITC-Dextran Standard Curve and Gradient

All FITC-Dextran studies used 2% alginate. Images were taken with 1 second exposure times. Fluorescence intensity thresholds were set to exclude artifacts and background. Gradient images

were stitched using ImageJ's stitching plugin [252]. Colormaps and fluorescence intensity plots were generated with custom Matlab code. Two images were excluded because of improper stitching.

FITC-Dextran alginate fluorescence intensities were measured in the presence of mTeSR1 with 1% AAS. Printed sheets were incubated at 37°C and 5% CO2 before intensity values were measured at later time points. Standard curve linear regression equations were generated using a known y-intercept calibrated to fluorescent images (N = 4) of a printed hydrogel sheet containing 0 mg/mL FITC-Dextran.

5.3 Results & Discussion

5.3.1 Vasculogenesis in Bioprinted Constructs

Our hydrogel composition incorporated alginate, which adds viscosity for printability, fast crosslinking capabilities, and mechanical strength as well as fibrinogen, which provides HSPG binding sites and bioactivity for our vascular cell types. The alginate concentration required optimization and was trialed at 0.5%, 1%, and 2% (w/v) mixed with the 5 mg/mL fibrinogen. These initial experiments were done with 5 mg/mL fibrinogen, and a 2:1 ratio of GFP-HUVECs and NHLFs at 3 x 10^6 cells/mL to mimic optimized conditions used in our microfluidics studies. 0.5% alginate was not viscous enough to impart printability and created hydrogels that were too mechanically unstable for our long-term study. Meanwhile, network formation was not seen with 2% alginate for 32 days in culture (N = 3). Alginate lacks ligands for cellular interaction [253], and we suspect this is the reason why higher alginate concentrations impeded network formation. Therefore, we hypothesized that alginate, functionalized with RGD, may be more conducive towards vasculogenesis. However, 2% (w/v) RGD-alginate, without fibrinogen, did not produce networks for 33 days. This would indicate that fibrinogen is a critical component in the network formation process. Only 1% normal alginate with fibrinogen was conducive to network formation where networks began forming as early as day 5 (**Figure 5.1**). Therefore, 1% (w/v) alginate with 5 mg/mL fibrinogen was determined to be the optimal concentrations for our hybrid hydrogel.

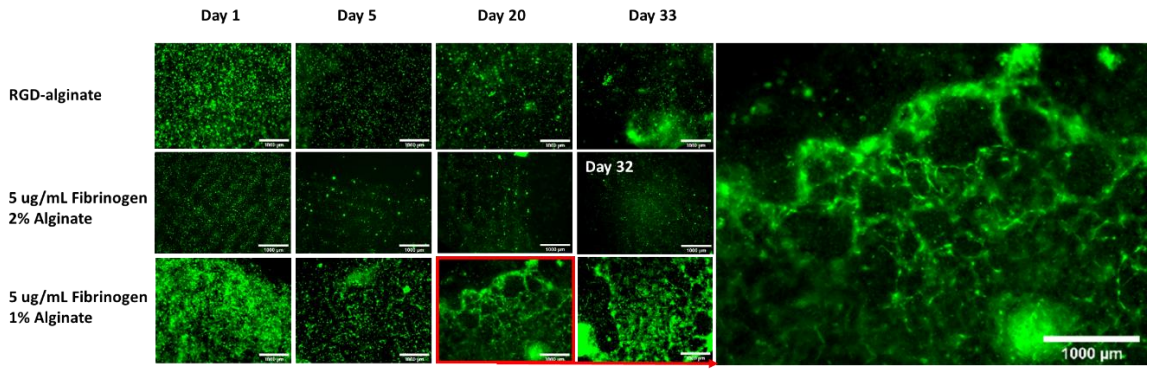

Figure 5.1 *Vascular network formation of GFP-HUVECs seeded with NHLFs and different hydrogel compositions (N = 3). In 5 ug/mL fibrinogen 1% alginate hydrogel, network formation began as early as day 5 and was prominent by day 20. Network formation was not a behavior observed in the RGD-alginate hydrogel.*

Other bioprinting studies have managed to induce network formation in materials such as collagen [254,255], gelatin methacrylate [256,257], and fibrinogen [258]. However, to my knowledge, no other paper has used a material that is as inexpensive and easy to handle as our alginate/fibrinogen hydrogel to induce network formation.

5.3.2 Quantification of VEGF Gradient

We sought to guide our bioprinted networks with the presence of a VEGF gradient. In native tissue, growth factors would be immobilized by HSPG binding sites on ECM. Therefore, we sought to determine how long a printed VEGF gradient could be retained within a 5 mg/mL fibrin + 1% alginate hybrid hydrogel. Our gradient concentration increased across the diagonal of a square, single filament sheet of hydrogel.

While it was easy to visualize a gradient of food coloring, it was difficult to detect a fluorescent gradient of VEGF as physiological concentrations of growth factors are too low to support a sufficient fluorescent reporter concentration. Even as we iterated towards very high concentrations of VEGF (2 ug/mL) with a high, exponential gradient strength of 95% and a long, 10 second exposure time on our epifluorescence microscope, the signal-to-noise ratio remained low (data not shown).

Considering the limitations of VEGF, we pivoted to using 40kDa FITC-Dextran as a substitute for fluorescently conjugated VEGF. FITC-Dextran is much more cost effective than VEGF which allowed us to use high concentrations of the substance in the single digit mg/mL range, greatly increasing the signal-to-noise ratio. Furthermore, 40kDa approximates the molecular weight of VEGF, allowing us to recapitulate some diffusion characteristics. However, FITC-Dextran does not possess the binding sites found on VEGF which would allow for interaction with the ECM through heparan sulfates.

We first created a standard curve by quantifying the mean fluorescence intensities of hydrogels mixed with known concentrations of FITC-Dextran (**Figure 5.2**). While we produced standard curves for 4 different time points, only the standard curve at 0 hours would be used to calibrate the other experiments.

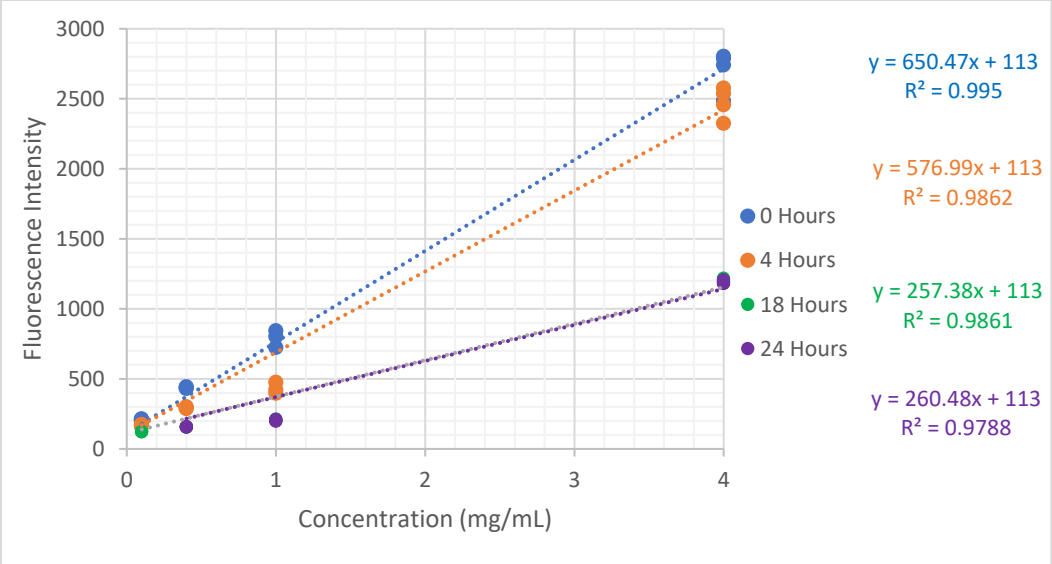

Figure 5.2 *Standard curve for 2% alginate mixed with known concentrations of FITC-Dextran. Measurements were taken at 4 different time points for 0.1, 0.4, 1, and 4 mg/mL FITC-Dextran. Each condition is (N ≥ 3).*

We tracked 5 gradient sheets created with 2 mg/mL FITC-Dextran for over 4 days (**Figure 5.3**). We quantified the fluorescence intensities of FITC-Dextran gradients along the direction of the gradient using custom Matlab code. The gradients began with a noisy, uneven gradient and smooths and decreases in intensity over the course of the study. After 4 days under culture conditions without cells, a less concentrated gradient remains intact (**Figure 5.3B**). Fluorescence intensity measurements are susceptible to the distortions of artifacts, air bubbles, and scattering from neighboring pixels. Due to the noise, we averaged 5 samples for each timepoint.

Unexpectedly, the high ends of the gradient were producing fluorescence intensities that were exceeding the standard curve's intensity corresponding to 2 mg/mL, the printed concentration. We observed that the printed sheet is noticeably thicker at the high concentration end (data not shown) We hypothesize that excess deposition of solution into the support bath disrupts the bath's integrity, causing increased hydrogel dispersion and abnormally high fluorescence intensities. The theoretically maximum embedded concentration should be equivalent to the printed concentration. Therefore, we estimate that a fluorescence intensity corresponding to 2 mg/mL marks the valve open time (6,000 µs with a 100 µm ID nozzle at 5 psi) that saturates the gelatin support bath. In line with our hypothesis, fluorescence intensity quantifications deviate from a linear fit after the point of saturation (**Figure 5.3C**).

We related the ratio of embedded to printed concentration of solute to the microdispensing valve's open time (**Figure 5.3C**). This figure was generated with 0 Days data from **Figure 5.3B** where the embedded concentration was determined from converting fluorescence intensity data with the standard curve from **Figure 5.2**. Valve open time was determined by converting distance with **Equation 2.8**. Only values below saturation are used to generate the linear regression equation.

The standard curve and quantifications in **Figure 5.3** are system-specific and we encourage users of ModiPrint to determine the fraction of entrapped solutes for each experiment.

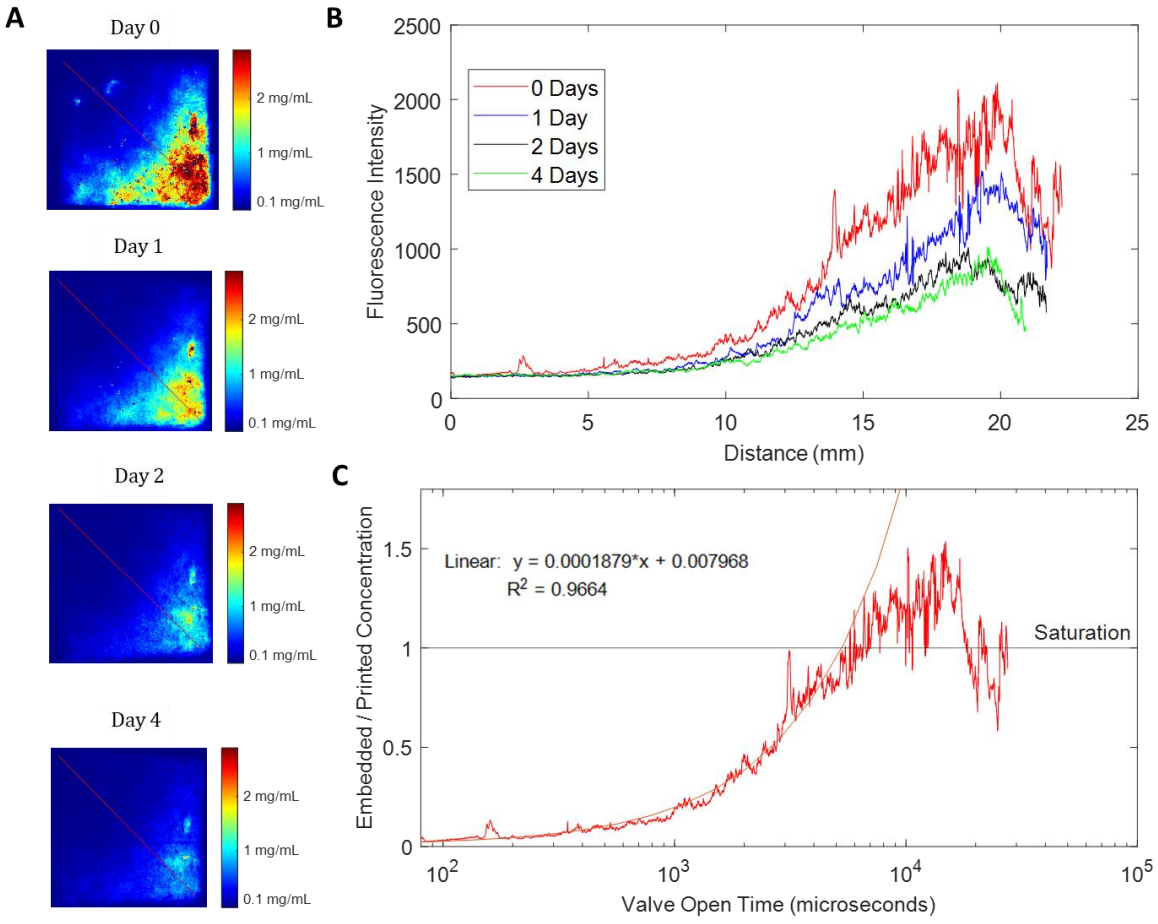

Figure 5.3 *Quantification of FITC-Dextran gradients.* ***A)*** *Fluorescence density colormaps of a 15x15 mm sheet containing a FITC-Dextran gradient over time. The colorbar values are determined from 0 Hour standard curve regression equation from Figure 5.2. The red line represents the 1-dimensional area that is quantified for Figure 5.3B.* ***B)*** *Average fluorescence intensities of gradients over time and distance. (N = 5)* ***C)*** *Ratio of final over initial concentration of small molecules embedded vs. valve open time. The linear regression equation is calculated with values below saturation.*

A noteworthy issue that we encountered was bubble formation. ModiPrint moves the printhead along the toolpath designated by g-code, stopping every interpolate distance (ID, a user-defined parameter) to dispense a droplet. However, this action disrupts the integrity of the support bath, and at short ID values (≤ 1 mm) creates gaps in the bath that manifests as bubbles embedded within the hydrogel. To mitigate this issue, we used a wider ID of 2 mm, and a slower printhead movement speed of 2 mm/s for this study. Chapter 2 results with food coloring gradients demonstrate that, qualitatively, such a large ID value does not create uneven gradients (**Figure 2.17**). And while a 2

mm ID necessitates that the gradient must be fabricated on millimeter-scale constructs, further optimization can improve the resolution of the gradient. A high exponential gradient strength (95%) also created more bubbles than a lower strength (45%). We believe this is also the result of long dispense times that is oversaturating the support bath with aqueous solution and disrupting its integrity. An improved version of the support bath with better self-healing capabilities (such as FRESH 2.0 [244]) or a microdispensing inkjet nozzle with a thinner outer diameter may be able to print bubble-free gradients with smaller ID values and higher gradient strengths.

5.3.3 Guided Vascularization with Bioprinted Concentration Gradients

Tricultures and tetracultures, embedded with VEGF gradients, are currently ongoing in what is planned to be a 40-day experiment. Data from previous experiments (N = 1) indicate that tricultures are not conducive to forming networks within 10 days (**Figure 5.4**, N = 1). On the other hand, tetracultures form networks at day 10. It is worth noting that structural stability of these prints was not sound because the printed sheets were too wide for their thickness. This caused the tetraculture sheet to fold (day 10) which warranted the cancellation and repeat of the experiment.

Images of the bioprinted sheets indicate that cell clumps form at certain corners of the sheet, a behavior not seen in any previous print. This would indicate that the presence of the gradient is guiding cell migration or proliferation towards a certain section of the sheet. However, these experiments were before the implementation of the protrusion that tracks the high and low ends of the gradient, therefore, we do not know if these clumps are forming at the high end. Replicate experiments will be necessary to confirm that this behavior is not a coincidence.

Bioprinted networks here are intended to complement other microfluidics studies in the McCloskey lab where other members are studying the effects of accessory cells on microfluidic vascular network formation. Our bioprinted experiments replicated the same cell type ratios and densities used in the microfluidic studies. Alike the microfluidic cultures, using only NHLFs as accessory cells and the tetraculture condition yielded the fastest time to network formation (5 – 10 days). Tricultures in the microfluidics were the slowest to form but were also the most stable. We were not able to see bioprinted triculture network formation as our experiment is not yet complete. Compared to the microfluidic devices, bioprinted networks generally form more slowly, from what we hypothesize, due to the presence of alginate which is not conducive to bioactivity.

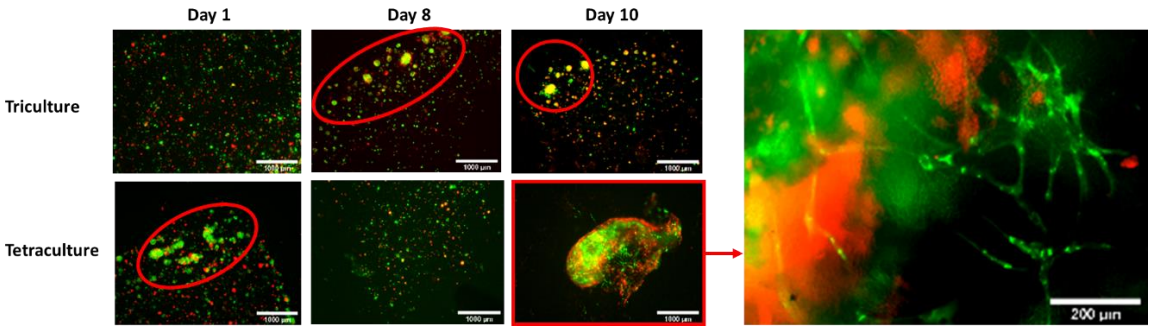

Figure 5.4 *Vascular network formation of triculture and tetracultures seeded with different hydrogel compositions. Tetracultures formed networks by 10 days whereas tricultures did not.*

5.3.4 Future Work

Proliferation, Migration, and Gradient Response

While preliminary results are promising, more work needs to be done to characterize the effects of the artificial VEGF gradient on ECs. We do not know if the clumping effect seen in **Figure 5.4** is a result of migration, proliferation, or coincidence. While replicate experiments can make the results more robust, other experiments can determine the mechanisms of gradient response.

The McCloskey lab has previous experience and the equipment to conduct time lapse experiments. Time-lapse microscopy can be used to track the migration of ECs in response to the gradient. To my knowledge, it is difficult to reliably trace the movements of individual cells at the high densities that we are printing. If individual cells cannot be traced by software or hand, a fluorescence coverage metric used with GFP-ECs, can estimate population changes over time.

VEGF is known to modulate both the proliferation and migration of ECs [259], but a timelapse on a dense population may not be able to decouple proliferation from migration. A printed population treated with mitomycin C (MMC) can would not proliferate thus a timelapse measuring only migration can be performed. However, MMC is known to modulate mechanisms related to vascularization and would be excluded from studies vascularization studies [260]. Proliferation can be tracked separately from migration through nuclear markers of proliferation. Ki67 , or cell cycle indicators, such as cyclin A, can be stained at multiple time points and locations in the gradient. However, this method would require destroying samples via fixation and single samples cannot be tracked over time.

Our hypothesis from these studies is that ECs at the higher end of the VEGF gradient will be more proliferative, and ECs at all areas would migrate towards the high end of the gradient.

Quantification of Vascular Networks

Vascular network formation can be quantitatively characterized with AngioTool [261], a computational tool that the McCloskey lab is familiar with. AngioTool quantifies metrics such as vessel length, density, and branching, where an increase of such parameters indicates improved vascularization. Meanwhile, ImageJ's Directionality plugin can analyze the sprouting direction of new vessels. Using these metrics, we can quantify the differences in vascularization between the high and low ends of the gradient. We hypothesize that the high end of the gradient would experience increased vessel length, density, and branching, and that network directionality would be more oriented parallel to the direction of the gradient.

Material Effect on Vascularization

We have noticed an increase in network formation time in our alginate/fibrinogen hydrogel compared to the pure fibrinogen conditions in microfluidic devices. Furthermore, we did not observe network formation in hydrogel compositions containing more than 1% alginate. This leads us to hypothesize that the presence of alginate is inhibiting the vascular cells' ability to remodel the surrounding matrix, which would be in-line with literature [262].

We used alginate in this study for its low cost, printability, and structural characteristics. But substitution of alginate with ECMs that contain cell binding motifs can potentially improve network formation speed and density. These substitutes can include other hydrogels which have been bioprinted and successfully induced network formation such as collagen [254,255] and gelatin methacrylate [256,257] as well as RGD-alginate which was demonstrated to be successful with

induced pluripotent stem cells in Chapter 2. Collagen is an especially attractive material as its processing and printing has been drastically improved with the recent introduction of FRESH 2.0 [244]. This improved version of the gelatin support bath also allows high resolution printing of unmodified collagen and can potentially mitigate bubbling issues with our gradient-patterning protocol.

5.4 Conclusion

A hybrid bioink of alginate and fibrinogen was optimized for vascular network formation of HUVECs with NHLFs while retaining the mechanical stability and viscosity necessary for bioprinting. Under these conditions, printed HUVECs formed vascular networks as early as 5 days and retained the networks for over a month. Inclusion of HAoSMCs (triculture) impeded network formation while further inclusion of PC (tetraculture) caused network formation to occur at 10 days. Furthermore, we were able to embed a gradient of FITC-Dextran into alginate hydrogel, demonstrate that a gradient is maintained for 4 days, and quantify the gradient's concentration. Printed vascular cells aggregated at certain corners of the construct in response to a VEGF gradient, indicating that cells may have proliferated or migrated in response to the gradient. Further experiments are still being conducted to elucidate the effects of accessory cells and VEGF gradients on bioprinted network formation. Future studies are being planned for quantification of vascular networks and mechanisms of gradient response. Few studies have produced vascular network formation in bioprinted constructs, and none have done so with our novel protocol that recapitulates the success of microfluidic networks.

Chapter 6: Conclusion

Objectives

The regenerative medicine field is pursuing lofty goals of creating artificial tissue. Larger artificial tissue from scalable techniques like bioprinting are valued for their future potential as substitutes for organ transplants, which are in constant short supply [3]. Meanwhile, highly functionalized tissue from organoids and microfluidics are well suited as an alternative drug testing platform to improve an inefficient pre-clinical screening process [7]. Following the discovery of iPSC [5], regenerative medicine progressed towards autologous tissues to resolve transplant rejection issues and personalized drug testing platforms. This establishes the workflow of regenerative medicine where stem cells are derived into target cell types, these cell types are patterned into 3D structures, the cells are left to self-assemble and functionalize, then the resulting tissue is characterized, implanted, or used for drug testing.

Currently, tissue engineering techniques cannot completely recapitulate the complexities of native tissue. Doing so would require the difficult feat of incorporating multiple cell types, ECM, and spatially patterning these components via engineering and self-assembly. Engineering techniques typically recapitulate the processes of native tissue, such as concentration gradients [71], embryoid bodies [28], and cocultures [212], to coax cells into forming their natural configurations. In the same vein, producing tissues that are dimensionally thicker than the limits of diffusion require perfusable vasculature. Large diameter vessels are artificially patterned while small diameter microvasculature require cells to be induced into sprouting or vasculogenesis [38].

Bioprinting is a popular patterning with exceptional geometric flexibility and scalability, positioning it to be the most suitable technique for creating artificial organs. However, bioprinting is also ill suited manipulate cellular microenvironments and recapitulate complexities which other techniques excel at. A major limitation is bioprinting's requirement for material printability, where bioinks must have suitable viscosity for controlled deposition and fast crosslinking to retain its printed structure. This greatly reduces the resolution of bioprinting in comparison to other techniques and relegates most studies to printing simple microenvironments of homogenously distributed ECM and proteins [21]. Furthermore, few bioprinting studies have viably dispensed pluripotent stem cells which are potent in self-assembling complex structures such as organoids [28].

Summary of Findings

I tackle these problems with bioprinting by creating a highly custom, multi-material bioprinter with hardware and software optimizations for improving resolution, viability, construct complexity, and accessibility (Chapter 2). This bioprinter, ModiPrint, uses a gas pressurized material reservoir and small nozzle diameters for controlled extrusion of semi-viscous materials. I was able to optimize this system to produce 100 μm diameter alginate filaments with the aid of FRESH support baths [17]. However, resolution is reduced when extruding complex geometries because the constant dispense rate of the extruder does not match the non-constant velocity of the XYZ stage. But with novel software and a rigid machine frame, I was able to implement fast cornering that reduces the velocity differential and retain high resolutions in complex geometries. Furthermore, I was able to print hiPSC with high viability and sterility maintained for 30 days without antibiotics. This can be

attributed to low travel time between the material reservoir and nozzle that reduces shear stress and compact device design that allows complete operation within a biosafety cabinet. The device also combines low volume drop-on-demand bioprinting with extrusion bioprinting to produce concentration gradients embedded within hydrogels. Unlike other techniques, concentration gradients produced by ModiPrint is scalable and not limited by geometry. ModiPrint integrates all these features with 3D models and an easy to use UI control software. All hardware components in ModiPrint are commercially available and is fully documented for anyone to recreate and operate for less than $4,000. All aspects of ModiPrint are open sourced except for the firmware which has been commercialized (www.modiprint.com) for a nominal fee.

I attempted to assist the McCloskey lab's endeavors in vascularization by adapting their protocol for generating EC from PSC to a protocol for generating VSMC (Chapter 3). This VSMC induction protocol would provide PSC-derived VSMC to complement PSC-derived EC in the lab's ongoing vasculogenesis studies. By using the same progenitor intermediate, this VSMC induction protocol would also allow the lab to study codifferentiation. I also aimed to optimize the protocol to produce the purest population of hiPSC-derived VSMC as VSMC lack surface markers that allow further purification by sorting. Initially, I used an atRA protocol to derive VSMC from mouse ESC and compared its marker expression, via flow cytometry, to primary VSMC isolated from mice aortas. I obtained some preliminary data that indicated that lower seeding densities and certain ECM were more conducive towards VSMC fate. However, I switched to a serum free protocol using hiPSC before completing the data set. I was able to consistently recreate the lab's protocol for producing high purity KDR+ VPC populations. But faulty antibodies invalidated years of data. The valid data remaining indicated that the hiPSC-derived VSMC were positive for a late marker, SMMHC, albeit inconsistently. However, other lab members were still able to use my hiPSC-derived VSMC populations as accessory cells to promote vasculogenesis, indicating that the VSMC behaved as mural cells in the context of vessel formation.

I sought to debug the issues related to the faulty VSMC marker antibodies (Chapter 3). The use of antibodies in combination with flow cytometry is a common way to characterize cell populations as it can perform high throughput, single cell analysis of multiple fluorescent reporters, cell size, and cell granularity. The specific issue I was experiencing was either nonspecific binding or a complete lack of binding of the antibodies to their intended epitope. I trialed the common methods used to debug this issue, including viability dye exclusions, use of blocking reagents, and the use of different staining kits. I then titrated eight different antibodies, with their respective isotype controls, against primary VSMC and a variety of negative control cells. Out of all eight antibodies, only one, SMMHC from eBioscience, was able to distinguish between positive and negative controls but only at a specific concentration. As we could not find more markers to characterize our hiPSC-derived VSMC, we could not continue our differentiation studies any further.

Finally, we were able to create bioprinted vascular networks in vitro which few other studies have been able to produce. These networks are the first step towards creating perfusable microvasculature in a scalable, geometrically flexible manner. We studied the effects of alginate and fibrinogen on network formation and found that fibrinogen was necessary to induce network formation and higher concentrations (2 wt/v%) of alginate impeded network formation. In our fibrinogen/alginate hydrogel, HUVECs with NHLFs were able to form networks as early as 5 days. Adding HAoSMCs (triculture) delayed or inhibited network formation. Additional PC (tetraculture) caused networks to form faster at 10 days. Furthermore, we demonstrated that

concentration gradients of VEGF could be retained within our bioprinted construct for at least 2 days. Preliminary data indicate that bioprinted vascular cells embedded with concentration gradients form aggregates at specific sections of the printed construct.

Contributions & Recommendations

The most impactful contributions of my graduate work are to the field of bioprinting. It is the most promising technique for creating artificial organs and large tissue but suffers shortfalls of resolution which leads to introduce biological complexity at the cellular level. Many studies optimize parameters for high resolution bioprinting, and some have achieved 100 µm diameters as I have [34]. However, most techniques require optimizations to the print parameters or materials which necessarily compromise other aspects of the printed results. I introduce a novel concept of acceleration control which can theoretically be applied to any pressure-driven extrusion printing system to improve resolutions without compromising structural integrity or material composition.

Currently, many bioprinting studies are limited to simple geometries for ease of production and characterization. However, native tissues are often more complex and consist of distinct layers/compartments of tissues interacting closely together. With continual improvements to resolution, printed constructs can better mimic the geometries of native tissue and recapitulate the microenvironment. While I, and many others, have introduced optimizations and techniques to improve the resolution of bioprinting, extrusion techniques are still typically limited to 100 µm resolutions at best. Higher resolutions typically require smaller diameter nozzles which comes with the compromise of higher susceptibility to clogging and longer print times. The issue of printing higher densities of cells (which are more prone to clogging) while maintaining higher resolutions is seldom explored. And to my knowledge, there are no practical methods to ensure that cells remain evenly distributed in the bioink throughout long prints. Furthermore, positioning multiple materials precisely and consistently is challenging [263]. To create truly complex, high resolution, multi-material constructs would require calibration protocols currently unknown to bioprinting. Advances in 3D printing technology may need to occur before these issues in bioprinting can be resolved.

I introduce a new technique for the fabrication of concentration gradients embedded in hydrogels. Concentration gradients are a well-known driving force for cell migration and tissue assembly in vivo, and many microfluidics studies have recapitulated this phenomena to manipulate cellular behavior in vitro [32]. However, bioprinting has not had the same successes in engineering such a complex microenvironment. Only one study has patterned gradients with bioprinting and it does so via a multi-nozzle approach [19]. I contribute another novel approach to printing gradients. My technique has its shortcomings, such as the requirement of a support bath, specialized control software, and large discretization of the gradient (2 mm) to avoid bubble formation. However, my technique has many strengths, including the simplification of the process to only 2 materials and full software integration which allows for the practical generation of complex gradient geometries. Unlike other bioprinting and microfluidics approaches, my gradient approach fully retains the flexibility, geometric advantages, and scalability of bioprinting.

Bioprinting hydrogels embedded with small molecule gradients is still a new concept, and the two techniques that exist require specialized equipment to execute. Furthermore, my technique and the multi-nozzle approach, discretizes the concentration gradient in steps at least hundreds of microns large. Gradients generated in such a way would necessarily be large compared to that generated

with microfluidic devices and diffusion. To my knowledge, gradients in vivo are typically generated by diffusion and gradients in the millimeter length scales may not physiologically accurate. Moreover, while microfluidic studies have recapitulated gradients and demonstrated their efficacy in controlling cell behavior, few studies have demonstrated the efficacy of gradients as an engineering tool to guide the formation of tissue. Much more work in surrounding fields would need to eb accomplished before concentration gradients in bioprinting can be more than just a novelty.

Many research groups are designing their own bioprinters, modifying thermoplastic printers with limited functionality, or purchasing expensive commercial devices. I introduce an alternative, low cost machine for research groups that cannot commercial devices or want novel features. My design of a novel, multi-material bioprinter combines high bioprinting (100 μm diameter alginate filaments) with the novel methods of improving resolution and embedding gradients. The device can also viably dispense hiPSC, which can be useful for future studies that rely on self-assembly for tissue functionalization. With the accessibility, feature set, and commercializing of ModiPrint, I expect other research groups to use the bioprinter's features to advance the bioprinting field.

The only open source bioprinters that are thoroughly documented for others to recreate are adaptations of thermoplastic printer which are limited in functionality. High performance, custom bioprinters are often not documented beyond the materials and methods sections. Even leading research groups in the bioprinting field introduce their systems with incomplete documentation or strange standards. This highly cited Nature paper publishes their C++ control software as a PDF file instead of on a dedicated code repository [59]. The field places little emphasis on the documentation and recreation of custom bioprinters, a flaw that caused me a great deal of unnecessary work to produce my own system. Understandably, few would put in the tedious effort to thoroughly document their devices as it does not create more publications. I have spent the extra effort to ease other research groups into recreating my technology and I hope I can set an example for others to do the same.

Although my studies with differentiating VSMC from hiPSC were not successful, I did produce data on the inconsistencies of several VSMC antibodies. It is considered a necessary practice to validate commercially available antibodies before use [221] and many manufacturers offer full refunds as researchers become increasingly wary of faulty products. Yet there is only one large-scale study of commercially available antibodies [228] and relatively few reports from individual research groups about faulty reagents. My failed study disseminates little more than which antibodies are faulty in the context of VSMC differentiation. Regardless, I believe more of such studies need to be reported, because for such a prevalent issue in biology, it is underrepresented in the literature.

My final contribution is that of vascularization in bioprinting, though it is still an incomplete study. Artificial thick tissue needs to recapitulate small and large diameter vascular to function as its in vivo counterpart. The current paradigm of vascularization in vitro is to sprout small diameter vessels from artificially patterned large diameter vessels. Bioprinting has the necessary traits of scalability and geometric complexity to produce large diameter vessels, but few bioprinting studies have managed to induce network formation. Here, we have induced vascular network formation with an alginate/fibrinogen hydrogel. We are continuing studies to understand the effects of a VEGF gradient on this system. If successful, we can potentially introduce a new method to guide

the directionality of vascular network formation in vitro and functionalize large diameter vessels to sprout in response to artificial gradients.

Bibliography

1. Kaushik G, J Leijten and A Khademhosseini (2017). Concise Review: Organ Engineering: Design, Technology, and Integration. Stem Cells 35: 51–60.
2. Dzobo K, NE Thomford, DA Senthebane, H Shipanga, A Rowe, C Dandara, M Pillay and KSCM Motaung (2018). Advances in regenerative medicine and tissue engineering: Innovation and transformation of medicine. Stem Cells Int 2018:.
3. Health Resources & Services Administration Organ Donation Statistics.
4. Wood KJ and R Goto (2012). Mechanisms of rejection: Current perspectives. Transplantation 93: 1–10.
5. Takahashi K and S Yamanaka (2006). Induction of Pluripotent Stem Cells from Mouse Embryonic and Adult Fibroblast Cultures by Defined Factors. Cell 126: 663–676.
6. Heidary Rouchi A and M Mahdavi-Mazdeh (2015). Regenerative Medicine in Organ and Tissue Transplantation: Shortly and Practically Achievable? Int J Organ Transplant Med 6: 93–98.
7. Karathanasis SK (2014). Regenerative Medicine: Transforming the Drug Discovery and Development Paradigm. Cold Spring Harb Perspect Med 4: a014084–a014084.
8. Pammolli F, L Magazzini and M Riccaboni (2011). The productivity crisis in pharmaceutical R&D. Nat Rev Drug Discov 10: 428–438.
9. Kola I and J Landis (2004). Can the pharmaceutical industry reduce attrition rates? Nat Rev Drug Discov 3: 711–715.
10. Langhans SA (2018). Three-dimensional in vitro cell culture models in drug discovery and drug repositioning. Front Pharmacol 9: 1–14.
11. Blancas AA, J Shih, SI Simon and E Mccloskey (2011). Functional Characterization of Embryonic Stem Cell-Derived Endothelial Cells. 415–428.
12. Cheung C, AS Bernardo, MWB Trotter, R a Pedersen and S Sinha (2012). Generation of human vascular smooth muscle subtypes provides insight into embryological origin–dependent disease susceptibility. Nat Biotechnol 30: 165–173.
13. Orlova V V., Y Drabsch, C Freund, S Petrus-Reurer, FE van den Hil, S Muenthaisong, P t. Dijke and CL Mummery (2014). Functionality of Endothelial Cells and Pericytes From Human Pluripotent Stem Cells Demonstrated in Cultured Vascular Plexus and Zebrafish Xenografts. Arterioscler Thromb Vasc Biol 34: 177–186.
14. William S. Turner, Nabjot Sandhu KEM (2014). Tissue Engineering: Construction of a Multicellular 3D Scaffold for the Delivery of Layered Cell Sheets. Jove.
15. Wong L, JD Pegan, B Gabela-Zuniga, M Khine and KE McCloskey (2017). Leaf-inspired microcontact printing vascular patterns. Biofabrication 9: 021001.
16. Kolesky DB, KA Homan, MA Skylar-Scott and JA Lewis (2016). Three-dimensional bioprinting of thick vascularized tissues. Proc Natl Acad Sci 113: 3179–3184.
17. Hinton TJ, Q Jallerat, RN Palchesko, JH Park, MS Grodzicki, H-J Shue, MH Ramadan, AR Hudson and AW Feinberg (2015). Three-dimensional printing of complex biological structures by freeform reversible embedding of suspended hydr(1) Hinton, T. J.; Jallerat, Q.; Palchesko, R. N.; Park, J. H.; Grodzicki, M. S.; Shue, H.-J.; Ramadan, M. H.; Hudson, A. R.; Feinberg, A. W. Thr. Sci Adv 1: e1500758–e1500758.
18. Belair DG, JA Whisler, J Valdez, J Velazquez, JA Molenda, V Vickerman, R Lewis, C Daigh, TD Hansen, DA Mann, JA Thomson, LG Griffith, RD Kamm, MP Schwartz and WL Murphy (2015). Human Vascular Tissue Models Formed from Human Induced Pluripotent Stem Cell Derived Endothelial Cells. Stem Cell Rev Reports 11: 511–525.
19. Liu W, YS Zhang, MA Heinrich, F De Ferrari, HL Jang, SM Bakht, MM Alvarez, J Yang, YC Li, G Trujillo-de Santiago, AK Miri, K Zhu, P Khoshakhlagh, G Prakash, H Cheng, X Guan, Z Zhong, J Ju, GH Zhu, X Jin, SR Shin, MR Dokmeci and A Khademhosseini (2017). Rapid Continuous Multimaterial Extrusion Bioprinting. Adv Mater 29: 1–8.
20. Faulkner-Jones A, C Fyfe, D-J Cornelissen, J Gardner, J King, A Courtney and W Shu (2015). Bioprinting of human pluripotent stem cells and their directed differentiation into hepatocyte-like cells for the generation of mini-livers in 3D. Biofabrication 7: 044102.
21. Dasgupta Q and LD Black (2019). A FRESH SLATE for 3D bioprinting. Science (80-) 365: 446–447.

22. Huang L, A Holtzinger, I Jagan, M Begora, I Lohse, N Ngai, C Nostro, R Wang, LB Muthuswamy, HC Crawford, C Arrowsmith, SE Kalloger, DJ Renouf, AA Connor, S Cleary, DF Schaeffer, M Roehrl, MS Tsao, S Gallinger, G Keller and SK Muthuswamy (2015). Ductal pancreatic cancer modeling and drug screening using human pluripotent stem cell- and patient-derived tumor organoids. Nat Med 21: 1364–1371.
23. Glaser DE, WS Turner, N Madfis, L Wong, J Zamora, N White, S Reyes, AB Burns, A Gopinathan and KE McCloskey (2016). Multifactorial Optimizations for Directing Endothelial Fate from Stem Cells. PLoS One 11: e0166663.
24. Tu C, BS Chao and JC Wu (2018). Strategies for improving the maturity of human induced pluripotent stem cell-derived cardiomyocytes. Circ Res 123: 512–514.
25. Engel M, D Do-Ha, SS Muñoz and L Ooi (2016). Common pitfalls of stem cell differentiation: a guide to improving protocols for neurodegenerative disease models and research. Cell Mol Life Sci 73: 3693–3709.
26. Armulik A, G Genové and C Betsholtz (2011). Pericytes: Developmental, Physiological, and Pathological Perspectives, Problems, and Promises. Dev Cell 21: 193–215.
27. Dominici M, K Le Blanc, I Mueller, I Slaper-Cortenbach, F Marini, D Krause, R Deans, A Keating, D Prockop and E Horwitz (2006). Minimal criteria for defining multipotent mesenchymal stromal cells. The International Society for Cellular Therapy position statement. Cytotherapy 8: 315–317.
28. Takahashi T (2019). Organoids for Drug Discovery and Personalized Medicine. Annu Rev Pharmacol Toxicol 59: 447–462.
29. Rossi G, A Manfrin and MP Lutolf (2018). Progress and potential in organoid research. Nat Rev Genet 19: 671–687.
30. Zhang B, A Korolj, BFL Lai and M Radisic (2018). Advances in organ-on-a-chip engineering. Nat Rev Mater 3: 257–278.
31. Guo F, JB French, P Li, H Zhao, CY Chan, JR Fick, SJ Benkovic and TJ Huang (2013). Probing cell–cell communication with microfluidic devices. Lab Chip 13: 3152.
32. Wang X, Z Liu and Y Pang (2017). Concentration gradient generation methods based on microfluidic systems. RSC Adv 7: 29966–29984.
33. Murphy S V and A Atala (2014). 3D bioprinting of tissues and organs. Nat Biotechnol 32: 773–785.
34. Lee JM and JM Lee (2019). Resolution and shape in bioprinting : Strategizing towards complex tissue and organ printing Resolution and shape in bioprinting : Strategizing towards complex tissue and organ printing. 011307:.
35. Armistead FJ, J Gala De Pablo, H Gadêlha, SA Peyman and SD Evans (2019). Cells Under Stress: An Inertial-Shear Microfluidic Determination of Cell Behavior. Biophys J 116: 1127–1135.
36. Aguado BA, W Mulyasasmita, J Su, KJ Lampe and SC Heilshorn (2012). Improving viability of stem cells during syringe needle flow through the design of hydrogel cell carriers. Tissue Eng - Part A 18: 806–815.
37. Cidonio G, M Glinka, JI Dawson and ROC Oreffo (2019). The cell in the ink: Improving biofabrication by printing stem cells for skeletal regenerative medicine. Biomaterials 209: 10–24.
38. Gianni-Barrera R, N Di Maggio, L Melly, MG Burger, E Mujagic, L Gürke, DJ Schaefer and A Banfi (2020). Therapeutic vascularization in regenerative medicine. Stem Cells Transl Med 9: 433–444.
39. Groebe K and P Vaupel (1988). Evaluation of oxygen diffusion distances in human breast cancer xenografts using tumor-specific in vivo data: Role of various mechanisms in the development of tumor hypoxia. Int J Radiat Oncol 15: 691–697.
40. Olive PL, C Vikse and MJ Trotter (1992). Measurement of oxygen diffusion distance in tumor cubes using a fluorescent hypoxia probe. Int J Radiat Oncol 22: 397–402.
41. Grigoryan B, SJ Paulsen, DC Corbett, DW Sazer, CL Fortin, AJ Zaita, PT Greenfield, NJ Calafat, JP Gounley, AH Ta, F Johansson, A Randles, JE Rosenkrantz, JD Louis-Rosenberg, PA Galie, KR Stevens and JS Miller (2019). Multivascular networks and functional intravascular topologies within biocompatible hydrogels. Science (80-) 364: 458–464.
42. Hasan A, A Paul, A Memic and A Khademhosseini (2015). A multilayered microfluidic blood vessel-like structure. Biomed Microdevices 17: 1–13.
43. Lee VK, AM Lanzi, H Ngo, S-S Yoo, PA Vincent and G Dai (2014). Generation of Multi-scale Vascular Network System Within 3D Hydrogel Using 3D Bio-printing Technology. Cell Mol Bioeng 7: 460–472.

44. Bogorad MI, J DeStefano, J Karlsson, AD Wong, S Gerecht and PC Searson (2015). Review: In vitro microvessel models. Lab Chip 15: 4242–4255.
45. Jeon JS, S Bersini, JA Whisler, MB Chen, G Dubini, JL Charest, M Moretti, RD Kamm, RK Jain, E Dejana, F Orsenigo, M Fukuda, N Hiraoka, JC Yeh, S Gout, PL Tremblay, J Huot, AJ LeBlanc, L Krishnan, CJ Sullivan, SK Williams, JB Hoying, GD Yancopoulos, S Davis, NW Gale, JS Rudge, SJ Wiegand, J Holash, P Carmeliet, M Hellstrom, H Gerhardt, M Kalen, X Li, U Eriksson, H Wolburg, C Betsholtz, G Thurston, C Suri, K Smith, J McClain, TN Sato, GD Yancopoulos, DM McDonald, A Armulik, A Abramsson, C Betsholtz, MJ Kluk, T Hla, RC Chambers, P Leoni, et al. (2014). Generation of 3D functional microvascular networks with human mesenchymal stem cells in microfluidic systems. Integr Biol 6: 555–563.
46. Wong LE (2018). Lion's Thesis Huehuehue.
47. Haase K and RD Kamm (2017). Advances in on-chip vascularization. 12: 285–302.
48. Glaser DE, AB Burns, R Hatano, M Medrzycki, Y Fan and KE McCloskey (2014). Specialized mouse embryonic stem cells for studying vascular development. Stem Cells Cloning 7: 79–88.
49. Blancas A a, AJ Shih, NE Lauer and KE McCloskey (2011). Endothelial Cells from Embryonic Stem Cells in a Chemically Defined Medium. Stem Cells Dev 20: 2153–2161.
50. Madfis N, Z Lin, A Kumar, SA Douglas, MO Platt, Y Fan and KE Mccloskey (2018). Co-Emergence of Specialized Endothelial Cells. 27: 326–335.
51. Yamashita J, H Itoh, M Hirashima, M Ogawa, S-I Nishikawa, T Yurugi, M Naito, K Nakao and S-I Nishikawa (2000). Flk1-positive cells derived from embryonic stem cells serve as vascular progenitors. Nature 408: 92–96.
52. Zhang YS, M Duchamp, R Oklu, LW Ellisen, R Langer and A Khademhosseini (2016). Bioprinting the Cancer Microenvironment. ACS Biomater Sci Eng 2: 1710–1721.
53. Li J, M Chen, X Fan and H Zhou (2016). Recent advances in bioprinting techniques: approaches, applications and future prospects. J Transl Med 14: 271.
54. Noh S, N Myung, M Park, S Kim, SU Zhang, HW Kang, C Mandrycky, Z Wang, K Kim and D-H Kim (2016). 3D bioprinting for engineering complex tissues. Biotechnol Adv 34: 422–434.
55. Hölzl K, S Lin, L Tytgat, S Van Vlierberghe, L Gu and A Ovsianikov (2016). Bioink properties before, during and after 3D bioprinting. Biofabrication 8: 32002.
56. Miller E, J Phillippi, G Fisher, P Campbell, L Walker and L Weiss (2009). Inkjet Printing of Growth Factor Concentration Gradients and Combinatorial Arrays Immobilized on Biologically-Relevant Substrates. Comb Chem High Throughput Screen 12: 604–618.
57. Lee VK, DY Kim, H Ngo, Y Lee, L Seo, SS Yoo, PA Vincent and G Dai (2014). Creating perfused functional vascular channels using 3D bio-printing technology. Biomaterials 35: 8092–8102.
58. Shim JH, JS Lee, JY Kim and DW Cho (2012). Bioprinting of a mechanically enhanced three-dimensional dual cell-laden construct for osteochondral tissue engineering using a multi-head tissue/organ building system. J Micromechanics Microengineering 22:.
59. Kang H, SJ Lee, IK Ko, C Kengla, JJ Yoo and A Atala (2016). A 3D bioprinting system to produce human-scale tissue constructs with structural integrity. Nat Biotechnol 34: 312–319.
60. Johnson GD, JA Reid, RC Ogle, PA Mollica, PC Sachs and RD Bruno (2016). Accessible bioprinting: adaptation of a low-cost 3D-printer for precise cell placement and stem cell differentiation. Biofabrication 8: 025017.
61. Lee J, KE Kim, S Bang, I Noh and C Lee (2017). A desktop multi-material 3D bio-printing system with open-source hardware and software. Int J Precis Eng Manuf 18: 605–612.
62. Tracy LE, RA Minasian and EJ Caterson (2016). Extracellular Matrix and Dermal Fibroblast Function in the Healing Wound. 5: 119–136.
63. Majesky MW, XR Dong, JN Regan and VJ Hoglund (2011). Vascular Smooth Muscle Progenitor Cells: Building and Repairing Blood Vessels. Circ Res 108: 365–377.
64. Berg J, T Hiller, MS Kissner, TH Qazi, GN Duda, AC Hocke, S Hippenstiel, L Elomaa, M Weinhart, C Fahrenson and J Kurreck (2018). Optimization of cell-laden bioinks for 3D bioprinting and efficient infection with influenza A virus. Sci Rep 1–13.
65. Wu Z, X Su, Y Xu, B Kong, W Sun and S Mi (2016). Bioprinting three-dimensional cell-laden tissue

constructs with controllable degradation. Nat Publ Gr 1–10.
66. Bioinks M, R Seyedmahmoud, B Çelebi-saltik, N Barros and R Nasiri (2019). Three-Dimensional Bioprinting of Functional Skeletal Muscle Tissue Using Gelatin. 1–12.
67. Suntornnond R, EYS Tan, J An and CK Chua (2016). A Mathematical Model on the Resolution of Extrusion Bioprinting for the Development of New Bioinks. Materials (Basel) 9:.
68. Wang G, L Yao, W Wang, J Ou, C Cheng and H Ishii (2016). xPrint: A Modularized Liquid Printer for Smart Materials Deposition. Proc 2016 CHI Conf Hum Factors Comput Syst 5743–5752.
69. Eital L What are the requirements for stepper motor acceleration?
70. Shen EM and KE McCloskey (2017). Development of Mural Cells: From In Vivo Understanding to In Vitro Recapitulation. Stem Cells Dev scd.2017.0020.
71. Wu J, Z Mao, S Yu, T Ren and C Gao (2012). Gradient Biomaterials and Their Impact on Cell Migration. In Polymeric Biomaterials for Tissue Regeneration, (Springer Singapore), pp. 337–355.
72. Mac Gabhann F, JW Ji and AS Popel (2007). VEGF gradients, receptor activation, and sprout guidance in resting and exercising skeletal muscle. J Appl Physiol 102: 722–734.
73. Faulkner-Jones A, S Greenhough, J a King, J Gardner, A Courtney and W Shu (2013). Development of a valve-based cell printer for the formation of human embryonic stem cell spheroid aggregates. Biofabrication 5: 015013.
74. Arduino Arduino Library Source Code.
75. McCauley M AccelStepper.
76. Staff E Generate stepper-motor speed profiles in real time.
77. GRBL Source Code.
78. Jeon S Improving Grbl: Cornering Algorithm.
79. Axis stalling on high speed arcs.
80. RepRap G-code.
81. Gao T, GJ Gillispie, JS Copus, AK PR, Y-J Seol, A Atala, JJ Yoo and SJ Lee (2018). Optimization of gelatin–alginate composite bioink printability using rheological parameters: a systematic approach. Biofabrication 10: 034106.
82. Leberfinger AN, DJ Ravnic, A Dhawan and IT Ozbolat (2017). Concise Review: Bioprinting of Stem Cells for Transplantable Tissue Fabrication. Stem Cells Transl Med 6: 1940–1948.
83. Gombotz W (1998). Protein release from alginate matrices. Adv Drug Deliv Rev 31: 267–285.
84. Jain D and D Bar-Shalom (2014). Alginate drug delivery systems: Application in context of pharmaceutical and biomedical research. Drug Dev Ind Pharm 40: 1576–1584.
85. Yue B (2014). Biology of the Extracellular Matrix: An Overview. J Glaucoma 0000000000: 1–8.
86. Townsley MI (2012). Structure and composition of pulmonary arteries, capillaries, and veins. Compr Physiol 2: 675–709.
87. Lindblom P (2003). Endothelial PDGF-B retention is required for proper investment of pericytes in the microvessel wall. Genes Dev 17: 1835–1840.
88. Bergers G and S Song (2005). The role of pericytes in blood-vessel formation and maintenance. Neuro Oncol 7: 452–464.
89. Volz KS, AH Jacobs, HI Chen, A Poduri, AS McKay, DP Riordan, N Kofler, J Kitajewski, I Weissman and K Red-Horse (2015). Pericytes are progenitors for coronary artery smooth muscle. Elife 4:.
90. Owens GK (2004). Molecular Regulation of Vascular Smooth Muscle Cell Differentiation in Development and Disease. Physiol Rev 84: 767–801.
91. Cheung C and S Sinha (2011). Human embryonic stem cell-derived vascular smooth muscle cells in therapeutic neovascularisation. J Mol Cell Cardiol 51: 651–664.
92. Neff LP, BW Tillman, SK Yazdani, MA Machingal, JJ Yoo, S Soker, BW Bernish, RL Geary and GJ Christ (2011). Vascular smooth muscle enhances functionality of tissue-engineered blood vessels in vivo. J Vasc Surg 53: 426–434.
93. Meng M, NG Zaorsky, L Deng, H Wang, J Chao, L-J Zhao, Z-Y Yuan and W Ping (2015). Pericytes: a double-edged sword in cancer therapy. Futur Oncol 11: 169–179.
94. Lian Q, Y Zhang, J Zhang, HK Zhang, X Wu, Y Zhang, FF-Y Lam, S Kang, JC Xia, W-H Lai, K-W Au, YY

Chow, C-W Siu, C-N Lee and H-F Tse (2010). Functional Mesenchymal Stem Cells Derived From Human Induced Pluripotent Stem Cells Attenuate Limb Ischemia in Mice. Circulation 121: 1113–1123.
95. Murry CE and G Keller (2008). Differentiation of Embryonic Stem Cells to Clinically Relevant Populations: Lessons from Embryonic Development. Cell 132: 661–680.
96. Tam PP. and RR Behringer (1997). Mouse gastrulation: the formation of a mammalian body plan. Mech Dev 68: 3–25.
97. Majesky MW (2007). Developmental Basis of Vascular Smooth Muscle Diversity. Arterioscler Thromb Vasc Biol 27: 1248–1258.
98. Dosch R, V Gawantka, H Delius, C Blumenstock and C Niehrs (1997). Bmp-4 acts as a morphogen in dorsoventral mesoderm patterning in Xenopus. Development 124: 2325–2334.
99. Schlueter J, J Männer and T Brand (2006). BMP is an important regulator of proepicardial identity in the chick embryo. Dev Biol 295: 546–558.
100. Duband J-L (2006). Neural crest delamination and migration: integrating regulations of cell interactions, locomotion, survival and fate. Adv Exp Med Biol 589: 45–77.
101. Marchant L, C Linker, P Ruiz, N Guerrero and R Mayor (1998). The inductive properties of mesoderm suggest that the neural crest cells are specified by a BMP gradient. Dev Biol 198: 319–329.
102. Vallier L, T Touboul, Z Chng, M Brimpari, N Hannan, E Millan, LE Smithers, M Trotter, P Rugg-Gunn, A Weber and R a. Pedersen (2009). Early cell fate decisions of human embryonic stem cells and mouse epiblast stem cells are controlled by the same signalling pathways. PLoS One 4:.
103. Kouskoff V, G Lacaud, S Schwantz, HJ Fehling and G Keller (2005). Sequential development of hematopoietic and cardiac mesoderm during embryonic stem cell differentiation. Proc Natl Acad Sci 102: 13170–13175.
104. Lee G, SM Chambers, MJ Tomishima and L Studer (2010). Derivation of neural crest cells from human pluripotent stem cells. Nat Protoc 5: 688–701.
105. Jiang X, DH Rowitch, P Soriano, a P McMahon and HM Sucov (2000). Fate of the mammalian cardiac neural crest. Development 127: 1607–1616.
106. Verzi MP, DJ McCulley, S De Val, E Dodou and BL Black (2005). The right ventricle, outflow tract, and ventricular septum comprise a restricted expression domain within the secondary/anterior heart field. Dev Biol 287: 134–145.
107. Waldo KL, MR Hutson, CC Ward, M Zdanowicz, H a. Stadt, D Kumiski, R Abu-Issa and ML Kirby (2005). Secondary heart field contributes myocardium and smooth muscle to the arterial pole of the developing heart. Dev Biol 281: 78–90.
108. Etchevers HC, C Vincent, NM Le Douarin and GF Couly (2001). The cephalic neural crest provides pericytes and smooth muscle cells to all blood vessels of the face and forebrain. Development 128: 1059–1068.
109. Mikawa T and RG Gourdie (1996). Pericardial Mesoderm Generates a Population of Coronary Smooth Muscle Cells Migrating into the Heart along with Ingrowth of the Epicardial Organ. Dev Biol 174: 221–232.
110. Dettman RW, W Denetclaw, CP Ordahl and J Bristow (1998). Common Epicardial Origin of Coronary Vascular Smooth Muscle, Perivascular Fibroblasts, and Intermyocardial Fibroblasts in the Avian Heart. Dev Biol 193: 169–181.
111. Pérez-Pomares J-M, R Carmona, M González-Iriarte, G Atencia, A Wessels and R Muñoz-Chápuli (2002). Origin of coronary endothelial cells from epicardial mesothelium in avian embryos. Int J Dev Biol 46: 1005–1013.
112. Wasteson P, BR Johansson, T Jukkola, S Breuer, LM Akyürek, J Partanen and P Lindahl (2008). Developmental origin of smooth muscle cells in the descending aorta in mice. Development 135: 1823–1832.
113. Topouzis S and MW Majesky (1996). Smooth Muscle Lineage Diversity in the Chick Embryo. Dev Biol 178: 430–445.
114. Wiegreffe C, B Christ, R Huang and M Scaal (2009). Remodeling of aortic smooth muscle during avian embryonic development. Dev Dyn 238: 624–631.
115. Pouget C, K Pottin and T Jaffredo (2008). Sclerotomal origin of vascular smooth muscle cells and

pericytes in the embryo. Dev Biol 315: 437–447.
116. Campagnolo P, D Cesselli, A Al Haj Zen, AP Beltrami, N Krankel, R Katare, G Angelini, C Emanueli and P Madeddu (2010). Human Adult Vena Saphena Contains Perivascular Progenitor Cells Endowed With Clonogenic and Proangiogenic Potential. Circulation 121: 1735–1745.
117. Hu Y, Z Zhang, E Torsney, AR Afzal, F Davison, B Metzler and Q Xu (2004). Abundant progenitor cells in the adventitia contribute to atherosclerosis of vein grafts in ApoE-deficient mice. J Clin Invest 113: 1258–1265.
118. Greif DM, M Kumar, JK Lighthouse, J Hum, A An, L Ding, K Red-Horse, FH Espinoza, L Olson, S Offermanns and MA Krasnow (2012). Radial Construction of an Arterial Wall. Dev Cell 23: 482–493.
119. Hellström M, M Kalén, P Lindahl, A Abramsson and C Betsholtz (1999). Role of PDGF-B and PDGFR-beta in recruitment of vascular smooth muscle cells and pericytes during embryonic blood vessel formation in the mouse. Development 126: 3047–3055.
120. Gaengel K, G Genove, A Armulik and C Betsholtz (2009). Endothelial-Mural Cell Signaling in Vascular Development and Angiogenesis. Arterioscler Thromb Vasc Biol 29: 630–638.
121. Benjamin LE, I Hemo and E Keshet (1998). A plasticity window for blood vessel remodelling is defined by pericyte coverage of the preformed endothelial network and is regulated by PDGF-B and VEGF. Development 125: 1591–1598.
122. Fredriksson L, H Li and U Eriksson (2004). The PDGF family: four gene products form five dimeric isoforms. Cytokine Growth Factor Rev 15: 197–204.
123. Sweeney MD, S Ayyadurai and B V Zlokovic (2016). Pericytes of the neurovascular unit: key functions and signaling pathways. Nat Neurosci 19: 771–783.
124. Tallquist MD, WJ French and P Soriano (2003). Additive Effects of PDGF Receptor β Signaling Pathways in Vascular Smooth Muscle Cell Development. PLoS Biol 1: 288–299.
125. Mack CP (2011). Signaling Mechanisms That Regulate Smooth Muscle Cell Differentiation. Arterioscler Thromb Vasc Biol 31: 1495–1505.
126. Olson LE and P Soriano (2011). PDGFRβ Signaling Regulates Mural Cell Plasticity and Inhibits Fat Development. Dev Cell 20: 815–826.
127. Wang A, Z Tang, X Li, Y Jiang, DA Tsou and S Li (2012). Derivation of Smooth Muscle Cells with Neural Crest Origin from Human Induced Pluripotent Stem Cells. Cells Tissues Organs 195: 5–14.
128. Wanjare M, S Kusuma and S Gerecht (2014). Defining Differences among Perivascular Cells Derived from Human Pluripotent Stem Cells. Stem Cell Reports 2: 561–575.
129. Kumar AHS, P Metharom, J Schmeckpeper, S Weiss, K Martin and NM Caplice (2010). Bone marrow-derived CX3CR1 progenitors contribute to neointimal smooth muscle cells via fractalkine CX3CR1 interaction. FASEB J 24: 81–92.
130. Tang Z, A Wang, F Yuan, Z Yan, B Liu, JS Chu, JA Helms and S Li (2012). Differentiation of multipotent vascular stem cells contributes to vascular diseases. Nat Commun 3: 875.
131. Howson KM (2005). The postnatal rat aorta contains pericyte progenitor cells that form spheroidal colonies in suspension culture. AJP Cell Physiol 289: 1396–1407.
132. Xiao Q, L Zeng, Z Zhang, Y Hu and Q Xu (2006). Stem cell-derived Sca-1+ progenitors differentiate into smooth muscle cells, which is mediated by collagen IV-integrin 1/beta1/ v and PDGF receptor pathways. AJP Cell Physiol 292: 342–352.
133. Sainz J (2005). Isolation of “Side Population” Progenitor Cells From Healthy Arteries of Adult Mice. Arterioscler Thromb Vasc Biol 26: 281–286.
134. Shi Y and J Massagué (2003). Mechanisms of TGF-β Signaling from Cell Membrane to the Nucleus. Cell 113: 685–700.
135. Nassiri F, MD Cusimano, BW Scheithauer, F Rotondo, A Fazio, GM Yousef, L V. Syro, K Kovacs and R V. Lloyd (2011). Endoglin (CD105): a review of its role in angiogenesis and tumor diagnosis, progression and therapy. Anticancer Res 31: 2283–2290.
136. Langlois D, M Hneino, L Bouazza, A Parlakian, T Sasaki, G Bricca and JY Li (2010). Conditional inactivation of TGF-β type II receptor in smooth muscle cells and epicardium causes lethal aortic and cardiac defects. Transgenic Res 19: 1069–1082.

137. Mancini ML, A Terzic, BA Conley, LH Oxburgh, T Nicola and CPH Vary (2009). Endoglin plays distinct roles in vascular smooth muscle cell recruitment and regulation of arteriovenous identity during angiogenesis. Dev Dyn 238: 2479–2493.
138. Sridurongrit S, J Larsson, R Schwartz, P Ruiz-Lozano and V Kaartinen (2008). Signaling via the Tgf-β type I receptor Alk5 in heart development. Dev Biol 322: 208–218.
139. Jeon ES, HJ Moon, MJ Lee, HY Song, YM Kim, YC Bae, JS Jung and JH Kim (2006). Sphingosylphosphorylcholine induces differentiation of human mesenchymal stem cells into smooth-muscle-like cells through a TGF-beta-dependent mechanism. J Cell Sci 119: 4994–5005.
140. Chen S and RJ Lechleider (2004). Transforming growth factor-beta-induced differentiation of smooth muscle from a neural crest stem cell line. Circ Res 94: 1195–1202.
141. Maurer J, S Fuchs, R Jäger, B Kurz, L Sommer and H Schorle (2007). Establishment and controlled differentiation of neural crest stem cell lines using conditional transgenesis. Differentiation 75: 580–591.
142. Wang N, G-D Ren, Z Zhou, Y Xu, T Qin, R-F Yu and T-C Zhang (2012). Cooperation of myocardin and smad2 in inducing differentiation of mesenchymal stem cells into smooth muscle cells. IUBMB Life 64: 331–339.
143. González-Núñez M, JM Muñoz-Félix and JM López-Novoa (2013). The ALK-1/Smad1 pathway in cardiovascular physiopathology. A new target for therapy? Biochim Biophys Acta - Mol Basis Dis 1832: 1492–1510.
144. Xie W-B, Z Li, N Shi, X Guo, J Tang, W Ju, J Han, T Liu, EP Bottinger, Y Chai, P a Jose and S-Y Chen (2013). Smad2 and MRTFB Cooperatively Regulate Vascular Smooth Muscle Differentiation from Neural Crest Cells. Circ Res 113: e76–e86.
145. Sinha S, MH Hoofnagle, PA Kingston, ME McCanna and GK Owens (2004). Transforming growth factor-beta1 signaling contributes to development of smooth muscle cells from embryonic stem cells. Am J Physiol Cell Physiol 287: 1560–1568.
146. Xie C, RP Ritchie, H Huang, J Zhang and YE Chen (2011). Smooth muscle cell differentiation in vitro: models and underlying molecular mechanisms. Arterioscler Thromb Vasc Biol 31: 1485–1494.
147. Colbert MC (2002). Retinoids and cardiovascular developmental defects. Cardiovasc Toxicol 2: 25–39.
148. Urvalek A, KB Laursen and LJ Gudas (2014). The roles of retinoic acid and retinoic acid receptors in inducing epigenetic changes. Subcell Biochem 70: 129–149.
149. Drab M, H Haller, R Bychkov, B Erdmann, C Lindschau, H Haase, I Morano, FC Luft and a M Wobus (1997). From totipotent embryonic stem cells to spontaneously contracting smooth muscle cells: a retinoic acid and db-cAMP in vitro differentiation model. FASEB J 11: 905–915.
150. Su Z, Y Li, X Zhao and M Zhang (2010). All-trans retinoic acid promotes smooth muscle cell differentiation of rabbit bone marrow-derived mesenchymal stem cells. J Zhejiang Univ Sci B 11: 489–496.
151. Huang H, X Zhao, L Chen, C Xu, X Yao, Y Lu, L Dai and M Zhang (2006). Differentiation of human embryonic stem cells into smooth muscle cells in adherent monolayer culture. Biochem Biophys Res Commun 351: 321–327.
152. Xie C-Q, H Huang, S Wei, L-S Song, J Zhang, RP Ritchie, L Chen, M Zhang and YE Chen (2009). A Comparison of Murine Smooth Muscle Cells Generated from Embryonic versus Induced Pluripotent Stem Cells. Stem Cells Dev 18: 741–748.
153. Lai L, BL Bohnsack, K Niederreither and KK Hirschi (2003). Retinoic acid regulates endothelial cell proliferation during vasculogenesis. Development 130: 6465–6474.
154. Rhinn M and P Dolle (2012). Retinoic acid signalling during development. Development 139: 843–858.
155. Wobus AM, J Rohwedel, V Maltsev and J Hescheler (1994). In vitro differentiation of embryonic stem cells into cardiomyocytes or skeletal muscle cells is specifically modulated by retinoic acid. Roux's Arch Dev Biol 204: 36–45.
156. Bain G, D Kitchens, M Yao, JE Huettner and DI Gottlieb (1995). Embryonic Stem Cells Express Neuronal Properties in Vitro. Dev Biol 168: 342–357.
157. Xiao Q, G Wang, Z Luo and Q Xu (2010). The mechanism of stem cell differentiation into smooth muscle cells. Thromb Haemost 104: 440–448.

158. Niland S and JA Eble (2012). Integrin-Mediated Cell-Matrix Interaction in Physiological and Pathological Blood Vessel Formation. J Oncol 2012: 1–25.
159. Abraham S, N Kogata, R Fassler and RH Adams (2008). Integrin 1 Subunit Controls Mural Cell Adhesion, Spreading, and Blood Vessel Wall Stability. Circ Res 102: 562–570.
160. Grazioli A, CS Alves, K Konstantopoulos and JT Yang (2006). Defective blood vessel development and pericyte/pvSMC distribution in α4 integrin-deficient mouse embryos. Dev Biol 293: 165–177.
161. Flintoff-Dye NL, J Welser, J Rooney, P Scowen, S Tamowski, W Hatton and DJ Burkin (2005). Role for the α7β1 integrin in vascular development and integrity. Dev Dyn 234: 11–21.
162. Turner CJ, K Badu-Nkansah, D Crowley, A van der Flier and RO Hynes (2015). α5 and αv integrins cooperate to regulate vascular smooth muscle and neural crest functions in vivo. Development 142: 797–808.
163. Turner CJ, K Badu-Nkansah, D Crowley, A van der Flier and RO Hynes (2014). Integrin-α5β1 is not required for mural cell functions during development of blood vessels but is required for lymphatic-blood vessel separation and lymphovenous valve formation. Dev Biol 392: 381–392.
164. Montanez E, S a Wickström, J Altstätter, H Chu and R Fässler (2009). α-parvin controls vascular mural cell recruitment to vessel wall by regulating RhoA/ROCK signalling. EMBO J 28: 3132–3144.
165. Chen Z-L, Y Yao, EH Norris, A Kruyer, O Jno-Charles, A Akhmerov and S Strickland (2013). Ablation of astrocytic laminin impairs vascular smooth muscle cell function and leads to hemorrhagic stroke. J Cell Biol 202: 381–395.
166. Rhodes JM and M Simons (2007). The extracellular matrix and blood vessel formation: not just a scaffold. J Cell Mol Med 11: 176–205.
167. Kelleher CM, SE McLean and RP Mecham (2004). Vascular extracellular matrix and aortic development. Curr Top Dev Biol 62: 153–188.
168. Kalluri R (2003). Basement membranes: structure, assembly and role in tumour angiogenesis. Nat Rev Cancer 3: 422–433.
169. Shimizu N, K Yamamoto, S Obi, S Kumagaya, T Masumura, Y Shimano, K Naruse, JK Yamashita, T Igarashi and J Ando (2008). Cyclic strain induces mouse embryonic stem cell differentiation into vascular smooth muscle cells by activating PDGF receptor beta. J Appl Physiol 104: 766–772.
170. Gluck JM, C Delman, J Chyu, WR MacLellan, RJ Shemin and S Heydarkhan-Hagvall (2014). Microenvironment influences vascular differentiation of murine cardiovascular progenitor cells. J Biomed Mater Res Part B Appl Biomater 102: 1730–1739.
171. Suzuki S, Y Narita, A Yamawaki, Y Murase, M Satake, M Mutsuga, H Okamoto, H Kagami, M Ueda and Y Ueda (2010). Effects of Extracellular Matrix on Differentiation of Human Bone Marrow-Derived Mesenchymal Stem Cells into Smooth Muscle Cell Lineage: Utility for Cardiovascular Tissue Engineering. Cells Tissues Organs 191: 269–280.
172. Gong Z and LE Niklason (2008). Small-diameter human vessel wall engineered from bone marrow-derived mesenchymal stem cells (hMSCs). FASEB J 22: 1635–1648.
173. Kim S-H, J Turnbull and S Guimond (2011). Extracellular matrix and cell signalling: the dynamic cooperation of integrin, proteoglycan and growth factor receptor. J Endocrinol 209: 139–151.
174. Taipale J and J Keski-Oja (1997). Growth factors in the extracellular matrix. FASEB J 11: 51–59.
175. Abramsson A, S Kurup, M Busse, S Yamada, P Lindblom, E Schallmeiner, D Stenzel, D Sauvaget, J Ledin, M Ringvall, U Landegren, L Kjellén, G Bondjers, J Li, U Lindahl, D Spillmann, C Betsholtz and H Gerhardt (2007). Defective N-sulfation of heparan sulfate proteoglycans limits PDGF-BB binding and pericyte recruitment in vascular development. Genes Dev 21: 316–331.
176. Abramsson A, P Lindblom and C Betsholtz (2003). Endothelial and nonendothelial sources of PDGF-B regulate pericyte recruitment and influence vascular pattern formation in tumors. J Clin Invest 112: 1142–1151.
177. Ji RP, CKL Phoon, O Aristizábal, KE McGrath, J Palis and DH Turnbull (2003). Onset of cardiac function during early mouse embryogenesis coincides with entry of primitive erythroblasts into the embryo proper. Circ Res 92: 133–135.
178. Landerholm TE, XR Dong, J Lu, NS Belaguli, RJ Schwartz and MW Majesky (1999). A role for serum

response factor in coronary smooth muscle differentiation from proepicardial cells. Development 126: 2053–2062.
179. Duband J-L, M Gimona, M Scatena, S Sartore and JV Small (1993). Calponin and SM22 as differentiation markers of smooth muscle: spatiotemporal distribution during avian embryonic development. Differentiation 55: 1–11.
180. Hughes S and T Chan-Ling (2004). Characterization of Smooth Muscle Cell and Pericyte Differentiation in the Rat Retina In Vivo. Investig Opthalmology Vis Sci 45: 2795–2806.
181. Ozerdem U, KA Grako, K Dahlin-Huppe, E Monosov and WB Stallcup (2001). NG2 proteoglycan is expressed exclusively by mural cells during vascular morphogenesis. Dev Dyn 222: 218–227.
182. Miano JM, P Cserjesi, KL Ligon, M Periasamy and EN Olson (1994). Smooth muscle myosin heavy chain exclusively marks the smooth muscle lineage during mouse embryogenesis. Circ Res 75: 803–812.
183. Chou R-GR, MH Stromer, RM Robson and TW Huiatt (1992). Assembly of contractile and cytoskeletal elements in developing smooth muscle cells. Dev Biol 149: 339–348.
184. Deruiter MC, SSM Rensen, GPGM Coolen, BP Hierck, M Bergwerff, WMH Debie, AC Gittenberger-De Groot and GJJM Van Eys (2001). Smoothelin expression during chicken embryogenesis: Detection of an embryonic isoform. Dev Dyn 221: 460–463.
185. Aikawa M, PN Sivam, M Kuro-o, K Kimura, K Nakahara, S Takewaki, M Ueda, H Yamaguchi, Y Yazaki and M Periasamy (1993). Human smooth muscle myosin heavy chain isoforms as molecular markers for vascular development and atherosclerosis. Circ Res 73: 1000–1012.
186. Borrione a C, a M Zanellato, G Scannapieco, P Pauletto and S Sartore (1989). Myosin heavy-chain isoforms in adult and developing rabbit vascular smooth muscle. Eur J Biochem 183: 413–417.
187. Kuro-o M, R Nagai, H Tsuchimochi, H Katoh, Y Yazaki, A Ohkubo and F Takaku (1989). Developmentally regulated expression of vascular smooth muscle myosin heavy chain isoforms. J Biol Chem 264: 18272–18275.
188. Beitz JG, IS Kim, P Calabresi and a R Frackelton (1991). Human microvascular endothelial cells express receptors for platelet-derived growth factor. Proc Natl Acad Sci U S A 88: 2021–2025.
189. Hewitt KJ, Y Shamis, E Knight, A Smith, A Maione, A Alt-Holland, SD Sheridan, SJ Haggarty and JA Garlick (2012). PDGFR expression and function in fibroblasts derived from pluripotent cells is linked to DNA demethylation. J Cell Sci 125: 2276–2287.
190. Guimarães-Camboa N, P Cattaneo, Y Sun, T Moore-Morris, Y Gu, ND Dalton, E Rockenstein, E Masliah, KL Peterson, WB Stallcup, J Chen and SM Evans (2017). Pericytes of Multiple Organs Do Not Behave as Mesenchymal Stem Cells In Vivo. Cell Stem Cell 20: 1–15.
191. Sugiyama S, K Kugiyama, S Nakamura, K Kataoka, M Aikawa, K Shimizu, S Koide, RN Mitchell, H Ogawa and P Libby (2006). Characterization of smooth muscle-like cells in circulating human peripheral blood. Atherosclerosis 187: 351–362.
192. Gan Q, T Yoshida, J Li and GK Owens (2007). Smooth Muscle Cells and Myofibroblasts Use Distinct Transcriptional Mechanisms for Smooth Muscle -Actin Expression. Circ Res 101: 883–892.
193. Li L, JM Miano, P Cserjesi and EN Olson (1996). SM22a Marker of Adult Smooth Muscle, Is Expressed in Multiple Myogenic Lineages During Embryogenesis. Circ Res 78: 188–195.
194. Miano JM and EN Olson (1996). Expression of the smooth muscle cell calponin gene marks the early cardiac and smooth muscle cell lineages during mouse embryogenesis. J Biol Chem 271: 7095–7103.
195. Samaha FF, HS Ip, EE Morrisey, J Seltzer, Z Tang, J Solway and MS Parmacek (1996). Developmental pattern of expression and genomic organization of the calponin-h1 gene. A contractile smooth muscle cell marker. J Biol Chem 271: 395–403.
196. Owens GK (1995). Regulation of differentiation of vascular smooth muscle cells. Physiol Rev 75: 487–517.
197. Tian X-X, J Kang, C-H Yan, K Xu, J Tao, G-T Yang and Y-L Han (2013). Purification and functional assessment of smooth muscle cells derived from mouse embryonic stem cells. J Geriatr Cardiol 10: 272–280.
198. Sinha S, BR Wamhoff, MH Hoofnagle, J Thomas, RL Neppl, T Deering, BP Helmke, DK Bowles, A V Somlyo and GK Owens (2006). Assessment of Contractility of Purified Smooth Muscle Cells Derived from

Embryonic Stem Cells. Stem Cells 24: 1678–1688.
199. Thornbury KD (1999). Tonic and phasic activity in smooth muscle. Ir J Med Sci 168: 201–207.
200. Krämer J, C Quensel, J Meding, MC Cardoso and H Leonhardt (2001). Identification and characterization of novel smoothelin isoforms in vascular smooth muscle. J Vasc Res 38: 120–132.
201. Gabbiani G, E Schmid, S Winter, C Chaponnier, C de Ckhastonay, J Vandekerckhove, K Weber and WW Franke (1981). Vascular smooth muscle cells differ from other smooth muscle cells: predominance of vimentin filaments and a specific alpha-type actin. Proc Natl Acad Sci 78: 298–302.
202. Kelley CA, M Takahashi, JH Yu and RS Adelstein (1993). An insert of seven amino acids confers functional differences between smooth muscle myosins from the intestines and vasculature. J Biol Chem 268: 12848–12854.
203. Chi J-T, EH Rodriguez, Z Wang, DSA Nuyten, S Mukherjee, M van de Rijn, MJ van de Vijver, T Hastie and PO Brown (2007). Gene Expression Programs of Human Smooth Muscle Cells: Tissue-Specific Differentiation and Prognostic Significance in Breast Cancers. PLoS Genet 3: 1770–1784.
204. Bichsel CA, SRR Hall, RA Schmid, OT Guenat and T Geiser (2015). Primary Human Lung Pericytes Support and Stabilize In Vitro Perfusable Microvessels. Tissue Eng Part A 21: 2166–2176.
205. Vo E, D Hanjaya-Putra, Y Zha, S Kusuma and S Gerecht (2010). Smooth-Muscle-Like Cells Derived from Human Embryonic Stem Cells Support and Augment Cord-Like Structures In Vitro. Stem Cell Rev Reports 6: 237–247.
206. Au P, J Tam, D Fukumura and RK Jain (2008). Bone marrow-derived mesenchymal stem cells facilitate engineering of long-lasting functional vasculature. Blood 111: 4551–4558.
207. Ross JJ and RT Tranquillo (2003). ECM gene expression correlates with in vitro tissue growth and development in fibrin gel remodeled by neonatal smooth muscle cells. Matrix Biol 22: 1–7.
208. Arihiro S, H Ohtani, N Hiwatashi, A Torii, T Sorsa and H Nagura (2001). Vascular smooth muscle cells and pericytes express MMP-1, MMP-9, TIMP-1 and type I procollagen in inflammatory bowel disease. Histopathology 39: 50–59.
209. Madsen CS, CP Regan, JE Hungerford, SL White, I Manabe and GK Owens (1998). Smooth muscle-specific expression of the smooth muscle myosin heavy chain gene in transgenic mice requires 5'-flanking and first intronic DNA sequence. Circ Res 82: 908–917.
210. Xin H-B, K-Y Deng, M Rishniw, G Ji and MI Kotlikoff (2002). Smooth muscle expression of Cre recombinase and eGFP in transgenic mice. Physiol Genomics 10: 211–215.
211. Jeon ES, WS Park, MJ Lee, YM Kim, J Han and JH Kim (2008). A Rho Kinase/Myocardin-Related Transcription Factor-A-Dependent Mechanism Underlies the Sphingosylphosphorylcholine-Induced Differentiation of Mesenchymal Stem Cells Into Contractile Smooth Muscle Cells. Circ Res 103: 635–642.
212. Whisler JA, MB Chen and RD Kamm (2014). Control of Perfusable Microvascular Network Morphology Using a Multiculture Microfluidic System. Tissue Eng Part C Methods 20: 543–552.
213. Adan A, G Alizada, Y Kiraz, Y Baran and A Nalbant (2017). Flow cytometry: basic principles and applications. Crit Rev Biotechnol 37: 163–176.
214. McKinnon KM (2018). Flow Cytometry: An Overview. Curr Protoc Immunol 120: 5.1.1-5.1.11.
215. Martins AA, A Paiva, JM Morgado, A Gomes and ML Pais (2009). Quantification and Immunophenotypic Characterization of Bone Marrow and Umbilical Cord Blood Mesenchymal Stem Cells by Multicolor Flow Cytometry. Transplant Proc 41: 943–946.
216. Khan SS, MA Solomon and JP McCoy (2005). Detection of circulating endothelial cells and endothelial progenitor cells by flow cytometry. Cytom Part B - Clin Cytom 64: 1–8.
217. Crouch EE and F Doetsch (2018). FACS isolation of endothelial cells and pericytes from mouse brain microregions. Nat Protoc 13: 738–751.
218. Cheung C, AS Bernardo, R a Pedersen and S Sinha (2014). Directed differentiation of embryonic origin-specific vascular smooth muscle subtypes from human pluripotent stem cells. Nat Protoc 9: 929–938.
219. Orlova V V., FE Van Den Hil, S Petrus-Reurer, Y Drabsch, P Ten Dijke and CL Mummery (2014). Generation, expansion and functional analysis of endothelial cells and pericytes derived from human pluripotent stem cells. Nat Protoc 9: 1514–1531.

220. Hulspas R (2010). Titration of Fluorochrome-Conjugated Antibodies for Labeling Cell Surface Markers on Live Cells. Curr Protoc Cytom 54: 1–9.
221. Kalina T, K Lundsten and P Engel (2020). Relevance of Antibody Validation for Flow Cytometry. Cytom Part A 97: 126–136.
222. Reinsberg J (1996). Different efficacy of various blocking reagents to eliminate interferences by human antimouse antibodies with a two-site immunoassay. Clin Biochem 29: 145–148.
223. Andersen MN, SNH Al-Karradi, TW Kragstrup and M Hokland (2016). Elimination of erroneous results in flow cytometry caused by antibody binding to Fc receptors on human monocytes and macrophages. Cytom Part A 89: 1001–1009.
224. Weller MG (2016). Quality Issues of Research Antibodies. Anal Chem Insights 2016: 21–27.
225. Baker M (2015). Reproducibility crisis: Blame it on the antibodies. Nature 521: 274–276.
226. Bradbury A and A Plückthun (2015). Reproducibility: Standardize antibodies used in research. Nature 518: 27–29.
227. Voskuil JLA (2017). The challenges with the validation of research antibodies. F1000Research 6: 161.
228. Berglund L, E Björling, P Oksvold, L Fagerberg, A Asplund, C Al-Khalili Szigyarto, A Persson, J Ottosson, H Wernérus, P Nilsson, E Lundberg, Å Sivertsson, S Navani, K Wester, C Kampf, S Hober, F Pontén and M Uhlén (2008). A Genecentric Human Protein Atlas for Expression Profiles Based on Antibodies. Mol Cell Proteomics 7: 2019–2027.
229. Gutiérrez OM, CC Sun, W Chen, JL Babitt and HY Lin (2012). Statement of Concern about a Commercial Assay Used to Measure sHJV. Am J Nephrol 36: 332–333.
230. Prassas I, D Brinc, S Farkona, F Leung, A Dimitromanolakis, CC Chrystoja, R Brand, V Kulasingam, IM Blasutig and EP Diamandis (2014). False Biomarker Discovery due to Reactivity of a Commercial ELISA for CUZD1 with Cancer Antigen CA125. Clin Chem 60: 381–388.
231. Bordeaux J, AW Welsh, S Agarwal, E Killiam, MT Baquero, JA Hanna, VK Anagnostou and DL Rimm (2010). Antibody validation. Biotechniques 48: 197–209.
232. Roncador G, P Engel, L Maestre, AP Anderson, JL Cordell, MS Cragg, V Šerbec, M Jones, VJ Lisnic, L Kremer, D Li, F Koch-Nolte, N Pascual, JI Rodríguez-Barbosa, R Torensma, H Turley, K Pulford and AH Banham (2016). The European antibody network's practical guide to finding and validating suitable antibodies for research. MAbs 8: 27–36.
233. Moonen JRAJ, G Krenning, MGL Brinker, JA Koerts, MJA van Luyn and MC Harmsen (2010). Endothelial progenitor cells give rise to pro-angiogenic smooth muscle-like progeny. Cardiovasc Res 86: 506–515.
234. Paranya G, S Vineberg, E Dvorin, S Kaushal, SJ Roth, E Rabkin, FJ Schoen and J Bischoff (2001). Aortic Valve Endothelial Cells Undergo Transforming Growth Factor-β-Mediated and Non-Transforming Growth Factor-β-Mediated Transdifferentiation in Vitro. Am J Pathol 159: 1335–1343.
235. Piera-Velazquez S, Z Li and SA Jimenez (2011). Role of Endothelial-Mesenchymal Transition (EndoMT) in the Pathogenesis of Fibrotic Disorders. Am J Pathol 179: 1074–1080.
236. Gardiner DM (2017). Regulation of Regeneration by Heparan Sulfate Proteoglycans in the Extracellular Matrix. Regen Eng Transl Med 3: 192–198.
237. Yan D and X Lin (2009). Shaping Morphogen Gradients by Proteoglycans. Cold Spring Harb Perspect Biol 1: a002493–a002493.
238. Sahni A and CW Francis (2000). Vascular endothelial growth factor binds to fibrinogen and fibrin and stimulates endothelial cell proliferation. Blood 96: 3772–3778.
239. Jafarkhani M, Z Salehi, A Aidun and MA Shokrgozar (2019). Bioprinting in Vascularization Strategies. 23: 9–20.
240. Gao Q, Y He, J Fu, A Liu and L Ma (2015). Coaxial nozzle-assisted 3D bioprinting with built-in microchannels for nutrients delivery. Biomaterials 61: 203–215.
241. Dai X, L Liu, J Ouyang, X Li, X Zhang, Q Lan and T Xu (2017). Coaxial 3D bioprinting of self-assembled multicellular heterogeneous tumor fibers. Sci Rep 7: 1457.
242. Liu W, Z Zhong, N Hu, Y Zhou, L Maggio, AK Miri, A Fragasso, X Jin, A Khademhosseini and YS Zhang (2018). Coaxial extrusion bioprinting of 3D microfibrous constructs with cell-favorable gelatin

methacryloyl microenvironments. Biofabrication 10: 024102.
243. Miller JS, KR Stevens, MT Yang, BM Baker, D-HT Nguyen, DM Cohen, E Toro, AA Chen, PA Galie, X Yu, R Chaturvedi, SN Bhatia and CS Chen (2012). Rapid casting of patterned vascular networks for perfusable engineered three-dimensional tissues. Nat Mater 11: 768–774.
244. Lee A, AR Hudson, DJ Shiwarski, JW Tashman, TJ Hinton, S Yerneni, JM Bliley, PG Campbell and AW Feinberg (2019). 3D bioprinting of collagen to rebuild components of the human heart. Science (80-) 365: 482–487.
245. Sasmal P, P Datta, Y Wu and IT Ozbolat (2018). 3D bioprinting for modelling vasculature. Microphysiological Syst 1: 1–1.
246. Kim S, W Kim, S Lim and JS Jeon (2017). Vasculature-on-a-chip for in vitro disease models. Bioengineering 4:.
247. Moya ML, Y-H Hsu, AP Lee, CCW Hughes and SC George (2013). In Vitro Perfused Human Capillary Networks. Tissue Eng Part C Methods 19: 730–737.
248. TAKAKURA N (2011). Role of intimate interactions between endothelial cells and the surrounding accessory cells in the maturation of blood vessels. J Thromb Haemost 9: 144–150.
249. Chen S, L Zhang, Y Zhao, M Ke, B Li, L Chen and S Cai (2017). A perforated microhole-based microfluidic device for improving sprouting angiogenesis in vitro. Biomicrofluidics 11: 054111.
250. Shirure VS, A Lezia, A Tao, LF Alonzo and SC George (2017). Low levels of physiological interstitial flow eliminate morphogen gradients and guide angiogenesis. Angiogenesis 20: 493–504.
251. Ko J, Y Lee, S Lee, S Lee and NL Jeon (2019). Human Ocular Angiogenesis-Inspired Vascular Models on an Injection-Molded Microfluidic Chip. Adv Healthc Mater 8: 1900328.
252. Preibisch S, S Saalfeld and P Tomancak (2009). Globally optimal stitching of tiled 3D microscopic image acquisitions. Bioinformatics 25: 1463–1465.
253. Sun J and H Tan (2013). Alginate-Based Biomaterials for Regenerative Medicine Applications. Materials (Basel) 6: 1285–1309.
254. Kérourédan O, J-M Bourget, M Rémy, S Crauste-Manciet, J Kalisky, S Catros, NB Thébaud and R Devillard (2019). Micropatterning of endothelial cells to create a capillary-like network with defined architecture by laser-assisted bioprinting. J Mater Sci Mater Med 30: 28.
255. Lee JW, Y-J Choi, W-J Yong, F Pati, J-H Shim, KS Kang, I-H Kang, J Park and D-W Cho (2016). Development of a 3D cell printed construct considering angiogenesis for liver tissue engineering. Biofabrication 8: 015007.
256. Byambaa B, N Annabi, K Yue, G Trujillo-de Santiago, MM Alvarez, W Jia, M Kazemzadeh-Narbat, SR Shin, A Tamayol and A Khademhosseini (2017). Bioprinted Osteogenic and Vasculogenic Patterns for Engineering 3D Bone Tissue. Adv Healthc Mater 6: 1700015.
257. Jia W, PS Gungor-Ozkerim, YS Zhang, K Yue, K Zhu, W Liu, Q Pi, B Byambaa, MR Dokmeci, SR Shin and A Khademhosseini (2016). Direct 3D bioprinting of perfusable vascular constructs using a blend bioink. Biomaterials 106: 58–68.
258. Zhang G, M Varkey, Z Wang, B Xie, R Hou and A Atala (2020). ECM concentration and cell-mediated traction forces play a role in vascular network assembly in 3D bioprinted tissue. Biotechnol Bioeng 117: 1148–1158.
259. Coultas L, K Chawengsaksophak and J Rossant (2005). Endothelial cells and VEGF in vascular development. Nature 438: 937–945.
260. Verma A, J DeGrado, AB Hittelman, MA Wheeler, HZ Kaimakliotis and RM Weiss (2011). Effect of mitomycin C on concentrations of vascular endothelial growth factor and its receptors in bladder cancer cells and in bladders of rats intravesically instilled with mitomycin C. BJU Int 107: 1154–1161.
261. Zudaire E, L Gambardella, C Kurcz and S Vermeren (2011). A Computational Tool for Quantitative Analysis of Vascular Networks. PLoS One 6: e27385.
262. Neves MI, L Moroni and CC Barrias (2020). Modulating Alginate Hydrogels for Improved Biological Performance as Cellular 3D Microenvironments. Front Bioeng Biotechnol 8:.
263. Sodupe-Ortega E, A Sanz-Garcia, A Pernia-Espinoza and C Escobedo-Lucea (2018). Accurate Calibration in Multi-Material 3D Bioprinting for Tissue Engineering. Materials (Basel) 11: 1402.